University of Strathclyde
Faculty of Engineering

Submitted to the Faculty of Engineering in fulfillment of the requirements for the degree of Doctor of Philosophy

On the Dynamics, Stability and Control of Displaced Lunar Orbits

by
Jules Simo

Glasgow

Declaration of author's rights

Acknowledgements

My first and greatest thanks go to my advisor Professor Colin McInnes, for his excellent guidance, support, and for giving me the opportunity to pursue a number of different and exciting projects during this time period. He introduced me to Solar Sailing and provided help and encouragement. I benefitted very much from his critical view of past and current developments in the field. He was constantly present when I needed his advice, and always willing to spend time on discussing new ideas.

It is hard to imagine a better academic environment for doing research. My thanks go to everyone at the university as well the AstroNet network (EU Marie Curie Network MRTN-CT-2006-035151), who has been contributing to this stimulating atmosphere. Thanks are also due to my friends for their moral support.

Most of all I wish to thank my family for their incredible support, understanding and patience.

Abstract

Now more than a speculative technology, solar sailing offers new capabilities for the design of space missions. This new concept promises to be useful in overcoming the challenges of transportation throughout the solar system. By exploiting the momentum transported by solar photons, solar sails can perform new high-energy mission concepts, which are essentially impossible for conventional propulsion, without the need for reaction mass.

In this thesis, novel families of highly non-Keplerian orbits (NKO) for spacecraft utilising either solar sail or solar electric propulsion (SEP) at linear order are investigated in the Earth-Moon circular restricted three-body problem (CRTBP). In particular, periodic orbits near the libration points in the Earth-Moon system will be explored along with their applications. A hybrid concept for displaced lunar orbits has been developed to overcome the limitations of both solar sailing and SEP. Feedback linearisation is used to perform stabilisation and trajectory tracking for the nonlinear system. In addition to a detailed investigation of the dynamics and control of highly NKO, effort will be devoted to develop a strategy that uses maneuvers executed impulsively at discrete time intervals. Thus, impulse control is investigated as a means of generating displaced orbits and is compared to continuous thrust control.

Furthermore, a methodology is developed for computing approximate large displaced orbits in the Earth-Moon CRTBP by the Moon-Sail two-body problem, and their local stability characteristics are investigated. It was found that orbits with a large displacement are unstable, as expected.

As will be shown, displaced periodic orbits exist at all libration points at linear order. A particular use of such orbits includes continous communications between the equatorial regions of the Earth and the lunar poles to support future robotic and human exploration.

Contents

List of Figures

List of Tables

Chapter 1

Introduction

The design of spacecraft trajectories is a crucial task in space mission design. However, propellant usage is a critical parameter for any spacecraft mission, thus the choice of an efficient control strategy is important. Farquhar [1] investigated station-keeping methods involving continuous thrusting and the use of solar sails to provide control forces. The continuing work on station-keeping by Colombo [2, 3] examined two possible methods of precisely maintaining a spacecraft at the interior libration point. The first approach involves the use of a solar sail, and the other technique uses a cable or tether that connect spaceceaft to each other. By varying the length of the cable, the spacecraft can be controlled such that it remains at the libration point. Propellantless spacecraft propulsion systems such as solar sailing rely on solar radiation pressure, the flux of momentum transported by sunlight, to provide propulsive force. A solar sail is then a large, flat, lightweight reflective surface deployed in space that can propel spacecraft without the use of propellant. Although the force on a solar sail spacecraft is less than a conventional chemical rocket, the solar sail spacecraft constantly accelerates over time and achieves a significant energy change. Therefore, this form of propulsion can in principle provide energy changes greater than are possible with either ion or chemical propellants.

Solar sails are being developed as a mission-enabling technology in support of future science missions. A wide range of missions have been studied and shown to be effective. These include the NOAA/NASA (National Oceanic and Atmospheric Administration/National Aeronautics and Space Administration) Geostorm mission and the Polar Observer missions. The Geostorm mission requires a solar sail to be placed at a point sunward of the classical Earth-Sun L_1 equilibrium point to provide early warning of solar storms. The primary goal of this mission is to provide enhanced warning of such storms to allow corrective action to be taken to protect vulnerable systems. This significant enhancement of warning time only requires a modest solar sail (see McInnes [4, 5]). The Polar Observer mission concept uses a solar sail displaced high above the L_1 point to provide real-time views of the polar regions of the Earth [4]. The use of large solar reflectors at the L_1 artificial libration point appears to be an efficient tool for climate engineering [6, 7, 8]. There are however many high energy missions which are either achieved by solar sailing or can be enabled at lower cost with electric or chemical propulsion [9, 10, 11]. Thus, a range of issues will

be adressed including the combination of solar sail and solar electric propulsion (SEP) to overcome the limitations of both solar sailing and SEP. For spacecraft applications, solar sailing is limited by the fact that the direction of the solar radiation pressure (SRP) force can never be pointed toward the Sun, while SEP can provide thrust in any direction. The solar sail is capable of providing cost effective, propellantless propulsion that enables a constant thrust over an extended mission lifetime, whereas SEP consumes propellant and decreases the mass of the spacecraft. SEP is now a realistic option for performing trajectories for interplanetary missions after its successful demonstration by the Deep Space 1 mission [12, 13].

The purpose of this investigation is to determine the feasibility of attaining and maintaining unique highly non-Keplerian orbits in the Earth-Moon system in order to obtain continuous communications between the equatorial regions of the Earth and the lunar poles. Thus, this thesis investigates the dynamics, stability and control of displaced periodic orbits in the circular restricted Earth-Moon system.

1.1 Why search for periodic orbits?

Periodic orbits have been studied extensively in dynamical systems. They are very important in the study of the structure of phase space, and in most cases the only solution which is known for all time. Besides, the stability behaviour of a dynamical system and its evolution depends on the topology of its phase space. Thus, the study of the stability along a family of periodic orbits of the planetary type can provide a first prediction on the regions of phase space where stable motion can exist.

It also has been recognized, first by H. Poincaré, that periodic orbits are fundamental to understanding the dynamics of planets and satellites. At the end of paragraph 36 of the first volume of the Méthodes nouvelles [14] one reads Poincaré's famous sentence about periodic (or relatively periodic) solutions:

"D'ailleurs, ce qui nous rend ces solutions périodiques si précieuses, c'est qu'elles sont, pour ainsi dire, la seule brèche par où nous puissions essayer de pénétrer dans une place jusqu'ici réputée inabordable".

That is roughly translated into English as *"What makes these periodic solutions so precious is that they are, so to say, the only breach through which we can try to penetrate into a region reputed, up to now, to be unapproachable".*

In fact, Poincaré considered periodic orbits the only way to access understanding of the behaviour in the difficult three-body problem. Prior work related to solar sail orbits is summarised below, followed by an outline and the contributions of this dissertation.

1.2 Previous Work

Over several years, solar sailing has been studied as a novel propulsion system for space missions. Solar sail technology appears as a promising form of advanced spacecraft propul-

sion which can enable exciting new space-science mission concepts such as solar system exploration and deep space observation. Although solar sailing has been considered as a practical means of spacecraft propulsion only relatively recently, the fundamental ideas are by no means new (see McInnes [4] for a detailed description). A solar sail is propelled by reflecting solar photons and therefore can transform the momentum of photons into a propulsive force. Solar sails can also be utilised for highly non-Keplerian orbits, such as orbits displaced high above the ecliptic plane (see Waters and McInnes [15, 16]). In Baoyin and McInnes [17, 18, 19], McInnes et al. [20, 21], the authors describe new orbits which are associated with artificial equilibrium points in the Earth-Sun system. These artificial equilibria have potential applications for future space physics and Earth observation missions. In McInnes and Simmons [22], Molostov and Shvartsburg [23, 24, 25], the authors investigate large new families of solar sail orbits, such as Sun-centered halo-type trajectories, with the sail executing a circular orbit of a chosen period above the ecliptic plane. In addition to displaced Sun-centered orbits [26, 27], displaced planet-centered orbits are also investigated [28, 29, 30, 31]. These circular orbits (displaced behind the planet in the anti-Sun direction) are generated by orienting the sail such that a component of the solar radiation pressure force is directed out of the orbit plane. Solar sails are especially suited for such highly non-Keplerian orbits, since they can apply a propulsive force continuously [32, 33, 34]. In such trajectories, a sail can be used as a communication satellite for high latitudes. For example, the orbital plane of the sail can be displaced above the orbital plane of the Earth, so that the sail can stay fixed above the Earth at some distance, if the orbital periods are equal (see Forward [35]).

The design of space missions to remain in the vicinity of an equilibrium point in a three-body system is both useful and more difficult than for a two-body system. However, many applications have been formulated in the two-body problem [36, 37, 38, 39, 40]. In the solar sail three-body problem, there has been less attention. This thesis contributes to new solar sail three-body orbits.

1.3 Problem Statement

The Earth-Moon libration points have been a topic of great interest in recent years [41, 42, 43]. Particularly attractive are the orbits around the collinear points because their unique positions are advantageous for several important applications in space mission design (see e.g. Szebehely [44], Roy [45], Vonbun [46], Gómez et al. [47, 48, 49]). In particular, Vonbun proposes an artificial L_2 point using low-thrust propulsion in the Earth-Moon system for lunar communications. This has the advantage of a short path length from the Moon to L_2, which is important for telecommunications applications. However, a linear analysis shows that the collinear libration points L_1, L_2, and L_3 are of the type $saddle \times center \times center$, leading to instability in their vicinity, whereas the equilateral equilibrium points L_4, and L_5 are stable ($center \times center \times center$). Although the libration points L_4, and L_5 are naturally stable, the disadvantage is the longer communication path length from the libration point to the Moon for communications applications. In analogy, the Trojan

asteroids were discovered near the triangular libration points of the Sun-Jupiter system. In recent years several authors have tried to determine more accurate approximations to orbits (quasi-Halo orbits) at such equilibrium points [50]. These orbits were first studied by Farquhar [51, 52], Farquhar and Kamel [50], Broucke [53, 54], Farquhar and Dunham [55, 56], Breakwell and Brown [57, 58], Richardson [59, 60], Howell [61, 62, 63, 64], Folta [65, 66], Wie [67]. If an orbit maintains visibility from Earth, a spacecraft on it (near the L_2 point) can be used to provide communications between the equatorial regions of the Earth and the lunar far-side. As can be seen in Figure 1.1, H is the out-of-plane distance for a spacecraft to be visible from Earth and the lunar far-side. The establishment of a bridge for radio communications is crucial for forthcoming space missions, which plan to use the lunar poles.

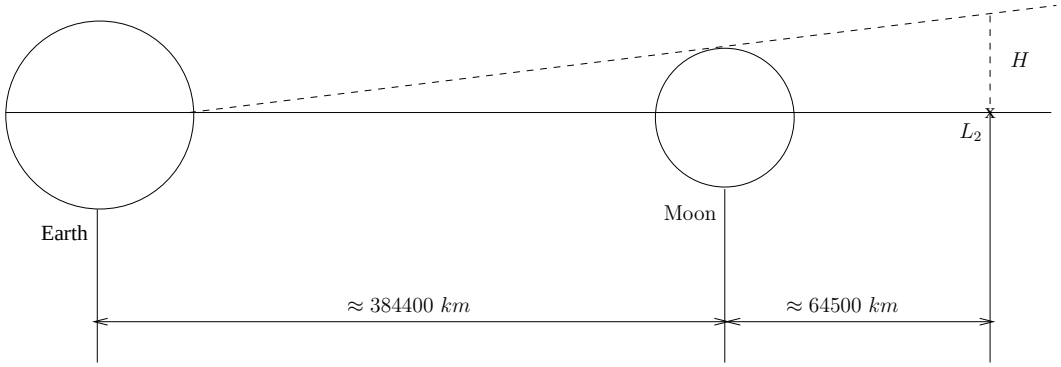

Figure 1.1: Geometry for Earth visibility.

The solar sail Earth-Moon problem differs greatly from the Earth-Sun system as the Sun-line direction varies continuously in the rotating frame and the equations of motion of the sail are given by a set of nonlinear, non-autonomous ordinary differential quations.

In this work, it will be largely assumed that the solar sail is a perfect reflector. A schematic diagram of a displaced Moon-centred orbit of radius ρ and displacement z using an idealised, perfectly reflecting solar sail can be seen in Figure 1.2. The position of the sail is given by $\boldsymbol{r}$ in a frame of reference rotating with angular velocity $\boldsymbol{\omega}_\star$ relative to an inertial frame I, where $\boldsymbol{\omega}_\star$ is the angular velocity of the Sun-line. The sail orientation is defined by the unit vector $\boldsymbol{n}$ fixed in the rotating frame of reference R. The sail attitude may be defined by the pitch angle γ between the Sun-line direction $\boldsymbol{S}$ and the sail normal vector $\boldsymbol{n}$. The requirement $\boldsymbol{S} \cdot \boldsymbol{n} \geq 0$ is imposed to ensure that the sail normal is always directed away from the Sun. Applications to such large displaced orbits are considered in Chapter 7.

The aim of this thesis is to investigate new families of highly non-Keplerian orbits, within the frame of the Earth-Moon circular restricted three-body problem (CRTBP). In particular, periodic orbits near the libration points of the CRTBP will be explored along with their applications. By making use of an approximate, first order analytical solution to the nonlinear, non-autonomous ordinary differential equations, periodic orbits can be derived that are displaced above/below the plane of the CRTBP. It is shown from linear

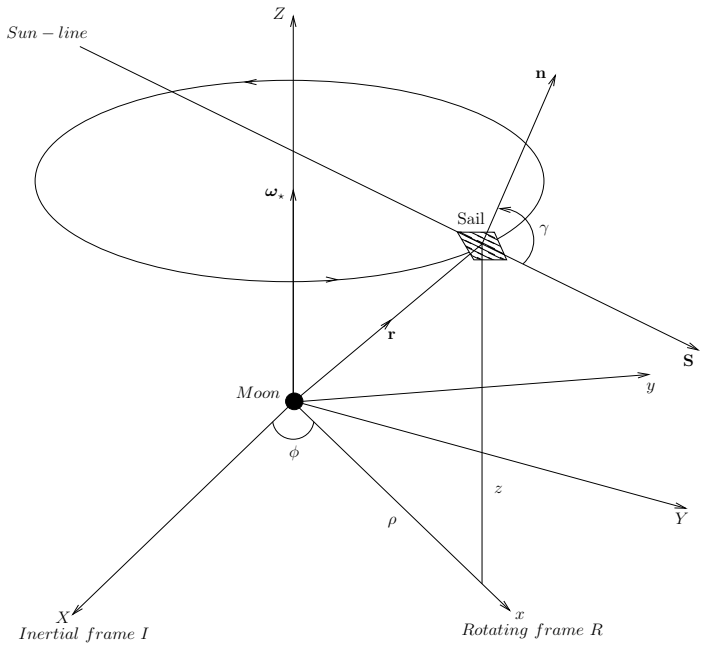

Figure 1.2: Displaced Moon-centered orbit.

analysis the existence of displaced lunar orbits by McInnes [68]. In this work, the nonlinear analysis is then adopted, which uses the linear solution as a reference orbit where the nonlinearities are compensated for using feedback linearisation, as will be discussed in Chapter 6. Thus, the thesis investigates displaced periodic orbits at linear order in the Earth-Moon restricted three-body system, where the third massless body utilises either a solar sail and/or solar electric propulsion [69, 70, 71, 72, 73, 74, 75, 76, 77, 78, 79, 80, 81, 82, 83]. These highly non-Keplerian orbits are achieved using an extremely small sail acceleration.

Displaced orbits have more recently been developed by Ozimek et al. [84, 85, 86] using collocation methods, and Wawrzyniak and Howell [87, 88, 89]. These numerically generated orbits are qualitatively similar to that shown schematically in Figure 1.2, while satisfying constraints on visibility from the lunar surface. A collocation method discretises both the trajectory and control, and generates a solution for the discretised states simultaneously.

1.4 Contributions of this Work

This thesis advances the state of the art by providing new insights into the dynamics of displaced solar sail orbits in the circular restricted Earth-Moon system. The dynamics are completely different from the Earth-Sun system in that the Sun-line direction constantly changes in the rotating frame, rotating once per synodic lunar month. In the following, it is shown that displaced periodic orbits exist at all Lagrange points at linear order. Furthermore, the dynamics of displaced orbits in relation to an approximate two-body Earth-Moon problem with a constant radiation pressure is considered. It was proved

that large displaced orbits in the Earth-Moon circular restricted three-body problem can be approximated by the Moon-Sail two-body problem. The importance of finding such displaced orbits is to obtain continuous communications between the equatorial regions of the Earth and the polar regions of the Moon. The solar sail can be used as a communication satellite for high latitude regions of the Moon, as shown Figure 1.3 using displaced orbits in the vicinity of the L_1 or L_2 libration points, as will be discussed in Chapter 5.

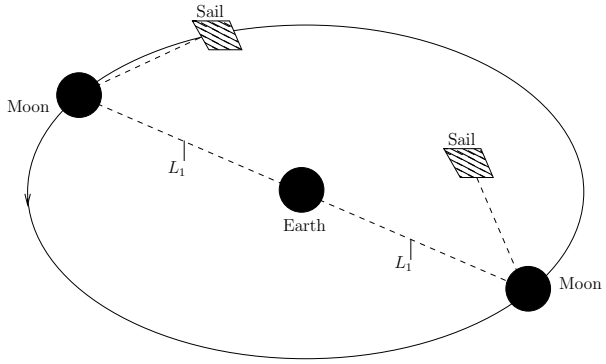

Figure 1.3: Displaced Moon-centered libration point orbit, viewed from an inertial frame.

The contribution of this thesis is summarised as follows:

- The development and analysis of a spacecraft model in the Earth-Moon system together with a generic low-thrust propulsion system using either a solar sail and/or solar electric propulsion.

- The use of hybrid solar electric propulsion in the Earth-Moon system to overcome some of the limitations of the pure sail (the solar radiation pressure force can never be directed sunward), since the solar electric propulsion can provide thrust in any direction through a gimbal-mounted thruster or attitude maneuvers.

- Use of feedback linearisation to perform stabilisation and trajectory tracking for the nonlinear system.

- Impulse control is investigated as a means of generating displaced lunar orbits and is compared to continuous thrust control.

- Approximation of large displaced orbits in the Earth-Moon circular restricted three-body problem by the Moon-Sail two-body problem.

Given the above points, this thesis will therefore address the following research questions:

- What novel insights can be obtained by exploring the dynamics of displaced lunar orbits related to the two- and three-body problem?

- Can hybrid low-thrust propulsion (solar sail and solar electric propulsion) be used to generate displaced periodic orbits in the Earth-Moon circular restricted three-body problem?
- Can impulse control be used as a means of enabling displaced lunar orbits?

These questions can be readily answered using the results of this thesis, as structured below.

1.5 Structure of the Work

This thesis is organised as follows:

In Chapter 2, a brief overview of propulsion systems (solar sails, electric and chemical) is presented.

Chapter 3 provides a summary of the models that are used throughout this work. The problem is mathematically developed, including the derivation of the equations of motion for the circular restricted three-body problem.

In Chapter 4, the linearised motion relative to the equilibrium solutions is discussed. This motion consists of two simultaneous harmonic oscillations with two corresponding frequencies, which are in general different. One motion is in the plane of the Moon's orbit, while the other is out-of-plane. The more general case of unequal frequencies in this Chapter results in a special type of Lissajous orbit with a period that is commensurate with the period of the primary orbit.

Chapter 5 is devoted to the study of a novel family of displaced periodic orbits at linear order in the Earth-Moon system using solar sail propulsion. A sufficient condition for displaced periodic orbits based on the sail pitch angle and the magnitude of the solar radiation pressure for a fixed initial out-of-plane distance has been derived. By introducing a first-order approximation, periodic orbits are derived analytically at linear order. Then, solar sail propulsion is used to provide station-keeping at periodic orbits around the libration points using small variations in the sail's orientation. Thus, the z-position is maintained at the triangular libration points by adjusting the control angle γ in such a way that it will cancel disturbances that drive the sail away from those points. The linear feedback controller is developed by linearising the z-dynamics around the triangular libration points and some sail attitude γ_0.

Chapter 6 investigates displaced periodic orbits at linear order in the circular restricted Earth-Moon system, where the third massless body utilises a hybrid of solar sail and a solar electric propulsion system. In particular, periodic orbits in the vicinity of the Lagrange points in the Earth-Moon system will be explored along with their applications. Firstly the dynamic model of the hybrid sail is described. The first-order approximation is derived for the linearised equations of motion. Then, a feedback linearisation control scheme (see Slotine and Li [90]) is proposed and implemented. The main idea of this approach is to cancel the non-linearities and to impose desired linear dynamics satisfied by the solar sail. The SEP control is selected, which takes into consideration the non-linearity cancellation

and the stabilising linear control. When the control is applied to the nonlinear system, asymtotic stability is achieved. This provides the key advantage that the displacement distance of the hybrid sail is then constant. A constant displacement distance of 1750 km has been considered for the simulations to ensure visibility from the Earth and lunar pole. In practice, a constant displacement distance may lead to easier tracking from the lunar surface for communications applications. Impulse control is also investigated to find displaced lunar orbits and is compared to continuous thrust control.

In Chapter 7, the dynamics of displaced orbits in relation to the two and three-body Earth-Moon problem are compared. Trajectories near the Earth-Moon L_1 and L_2 points are not easily identified, such that the solar sail can enable continuous communications with the equatorial regions of the Earth from any point on the lunar far-side. An asymptotic analysis for large and small accelerations is developed. This analysis is obtained within an approximation of large displaced orbits by the Moon-Sail two-body problem. The displaced periodic orbits found approach the asymptotic solutions as the characteristic acceleration becomes large. It is shown for example that, with a suitable sail attitude control program, a large out-of-plane trajectory far from the L_2 can be approximated using the two-body analysis. This simple, two-body approximate analysis matches with the large displaced orbits found by Ozimek et al. [84] using numerical collocation methods in a previous study. For small accelerations the linear approximation of the Earth-Moon three-body problem again matches well with Ozimek et al. [84]. In addition, the linear stability characteristics of the families of approximate periodic orbits are investigated.

Chapter 8 summarises the methods and results presented in this thesis, and indicates some avenues for related future work.

Publications

The following describes the author's contribution to the individual publications which are related to, or have influenced the work in this thesis.

Books:

1. Simo, J., McInnes, C.R. "Solar Sail Orbits at the Earth-Moon Libration Points," *In Nonlinear Science & Complexity*, Vol II, Springer, 2009, pp. 147-155.

2. Simo, J., McInnes, C.R. "Displaced Periodic Orbits with Low-Thrust Propulsion in the Earth-Moon System," *Advances in the Astronautical Sciences*, Vol. 134, 2009, pp. 815-828.

3. Simo, J., McInnes, C.R. "Displaced Solar Sail Orbits: Dynamics and Applications," *Advances in the Astronautical Sciences*, Vol. 136, 2010, pp. 1803-1816.

4. Simo, J., McInnes, C.R. "On the Stability of Approximate Displaced Lunar Orbits," *Advances in the Astronautical Sciences*, Vol. 136, 2010, pp. 1229-1238.

Journals:

1. Simo, J., McInnes, C.R. "Asymptotic Analysis of Displaced Lunar Orbits," *Journal of Guidance, Control and Dynamics*, Vol. 32, No. 5, September-October 2009, pp. 1666-1671.

2. Simo, J., McInnes, C.R. "Solar Sail Orbits at the Earth-Moon Libration Points," *Communications in Nonlinear Science and Numerical Simulation*, Vol. 14, No. 12, December 2009, pp. 4191-4196.

3. Simo, J., McInnes, C.R. "Designing Displaced Lunar Orbits using Low-Thrust Propulsion," *Journal of Guidance, Control and Dynamics*, Vol. 33, No. 1, January-February 2010, pp. 259-265.

Conferences:

1. Simo, J., McInnes, C.R. "Solar Sail Orbits at the Earth-Moon Libration Points," 2^{nd} *Conference on Nonlinear Science and Complexity, NSC 08*, Porto, Portugal, July 28-31, 2008.

2. Simo, J., McInnes, C.R. "Solar Sail Trajectories at the Earth-Moon Lagrange Points," 59^{th} *International Astronautical Congress, IAC 08*, Glasgow, Scotland, September 29-October 3, 2008. Paper IAC-08.C1.3.13.

3. Simo, J., McInnes, C.R. "Displaced Periodic Orbits with Low-Thrust Propulsion in the Earth-Moon System," 19^{th} *AAS/AIAA Space Flight Mechanics Meeting*, Savannah, Georgia, February 8-12, 2009. Paper AAS 09-153.

4. Simo, J., McInnes, C.R. "Stabilization of Displaced Periodic Orbits in the Solar Sail Restricted Three-Body Problem," *SIAM Conference on Applications of Dynamical Systems, DS09*, Snowbird, Utah, May 17-21, 2009.

5. Simo, J., McInnes, C.R. "Analysis and Control of Displaced Periodic Orbits in the Earth-Moon System," 60^{th} *International Astronautical Congress, IAC 09*, Daejeon, Republic of Korea, October 12-16, 2009. Paper IAC-09.C1.2.4.

6. Simo, J., McInnes, C.R. "On the Stability of Approximate Displaced Lunar Orbits," 20^{th} *AAS/AIAA Space Flight Mechanics Meeting*, San Diego, California, February 14-17, 2010. Paper AAS 10-181.

7. Simo, J., McInnes, C.R. "Displaced Solar Sail Orbits: Dynamics and Applications," 20^{th} *AAS/AIAA Space Flight Mechanics Meeting*, San Diego, California, February 14-17, 2010. Paper AAS 10-222.

8. Simo, J., McInnes, C.R. "Displaced Lunar Orbits Using Low-Thrust Propulsion: Application to Binary Asteroid," *Workshop on Applications on Control theory to Astrodynamics problems*, Surrey, England, April 26-27, 2010.

Chapter 2

Spacecraft propulsion

This Chapter discusses the underlying concept of solar sailing, solar electric propulsion (SEP) and chemical propulsion. It is intended as an overview of the theory for space propulsion and an exploration of the physics of solar radiation pressure used in this investigation. The contributions made in this thesis were largely performed using a perfectly reflecting solar sail. More detailed discussion can be found in the references which are noted throughout the sections. Accelerating efforts to advance the technology readiness level (TRL), and so reduce the advancement Degree of Difficulty (AD^2) can be made by combining solar sail and SEP propulsion, as described for a future advancement roadmap in reference [91]. TRL defines the maturity or readiness at discrete points in a schedule, and the AD^2 scale is developed to address issues of programmatic risk and to aid the incorporation of low-TRL components into larger systems. Therefore, the hybrid electric propulsion system is introduced to overcome the limitations of both solar sailing and SEP.

2.1 Solar Sailing

Solar sails have been studied for decades as a novel form of propulsion for planetary missions. Rather than carrying propellant, solar sails gain momentum from photons (the quantum packets of energy which compose Sunlight). However, the momentum transported by an individual photon is small. Thus, in order to intercept large numbers of photons, hence to provide a large momentum transfer, solar sails must have a large surface area (typically a square sail held in tension by four deployable diagonal booms), and be extremely light (see McInnes [4]). Scaled solar sails are depicted in Figure 2.1. IKAROS (Interplanetary Kite-craft Accelerated by Radiation of the Sun) is the Japan Aerospace Exploration Agency's experimental spacecraft, as shown in Figure 2.2.

By combining the impulse due to incident and reflected photons, the total force is directed normal to the surface of the solar sail. The orientation of the sail, and hence the force vector is defined relative to the Sun-line by the sail pitch angle. This is in contrast to the non-ideal sail (non perfect reflector), where the resultant force vector will not be in the direction normal to the sail surface due to the fact that the absorbed photon force is

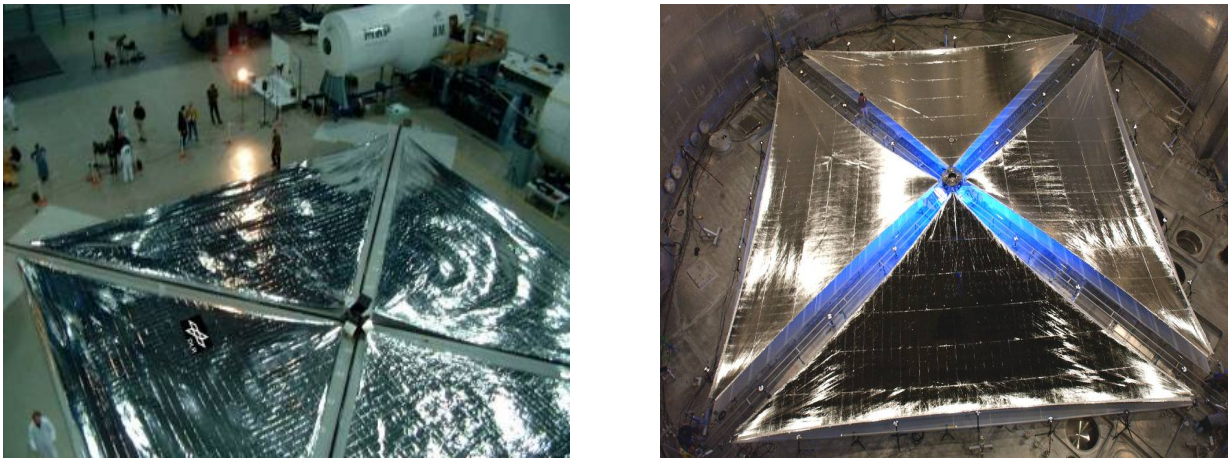

(*a*) (*b*)

Figure 2.1: (a) Ground test of a 20× 20 m solar sail (ESA); (b) Ground test of a 20× 20 m solar sail (NASA).

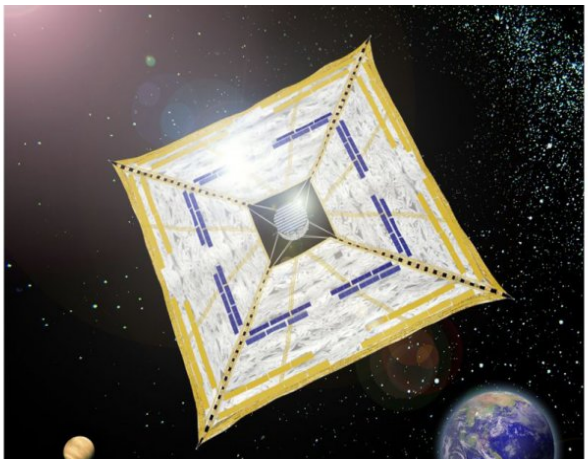

Figure 2.2: The IKAROS (Interplanetary Kite-craft Accelerated by Radiation of the Sun) solar sail (JAXA).

greater than the force due to reflected photons. The concept of the solar sail goes back as far as 1924 to Konstantin Tsiolkovsky [92] and his co-worker Friedrich Tsander [93]. The first proposed that large spacecraft could be propelled through space using photon pressure, and the second proposed a lightweight solar sail design. The concept of solar sailing appears to have remained relatively dormant for over thirty years. However, in 1958 Richard Garwin authored the first solar sail paper in the journal *Jet Propulsion*, and coined the term "solar sailing" (Garwin 1958). In the following, more detailed studies of solar sail orbits were undertaken, considering the mission applications and technology requirements [94, 95]. The design of a comet Halley rendezvous mission using solar sailing was initiated at the NASA Jet Propulsion Laboratory in November 1976. Since the NASA Comet Halley mission studies, a wide range of solar sail mission studies have been carried out. Therefore, a primary objective is to test and validate solar sail models that are currently under development so that they may be used with confidence in future mission development.

2.1.1 Solar Sail Mission Applications: Non-Keplerian Orbits

Solar sails have the capability to provide cost effective, propellantless propulsion that enables long mission lifetimes, deliver larger payload mass fractions, and generate highly non-Keplerian orbits that were previously inaccessible. A specific application for advanced solar sail spacecraft is the identification of highly non-Keplerian orbits, where the propulsive force is applied continuously in order to counteract gravity [96]. It should be noted that the new families of orbits are extensions to the classical two- and three-body problems in astrodynamics. A practical concern for other forms of low-thrust propulsion is the limited mission duration, which is fixed by the propellant mass fraction of the spacecraft. For these reasons, solar sails with a large propellantless ΔV capability can provide a wide range of opportunities for innovative low-cost missions.

A solar sailing mission architecture with a solar sail loading (mass per unit area) of only 1.5 gm^{-2} would enable solar physics missions that could levitate above the solar poles, providing continuous observations or hovering at any particular location in the solar system. Such a solar sail could also displace circular heliocentric orbits high above the ecliptic plane, where the orbit period is chosen to be synchronous with the Earth or some other solar system body (McInnes et al. [97]). Solar radiation pressure also impacts the location of the libration points. Consequently, the libration points of the Earth-Sun system can be artificially displaced using a modest solar sail (See McInnes et al. [20] and McInnes [98]). A case study example is the location of the L_1 point, that can be displaced closer to the Sun or even above the plane of the Earth's orbit. The proposed new sunward equilibrium location formed the basis for the NASA/NOAA Geostorm mission concept [99, 100, 101].

Displaced non-Keplerian orbits for solar sails have been considered by various authors for applications in two- and three-body problems. Thus, this thesis will investigate new families of orbits in the Earth-Moon circular restricted three-body problem (CRTBP). Applications include continuous line-of-sight communications with the lunar poles [102,

103, 104, 105, 106, 107].

Displaced orbits can also be used to increase the capacity of the geostationary ring. In fact, the pressure from sunlight reflecting off the solar sail pushes the satellite above or below geostationary orbit, and also displaces the centre of the orbit behind the Earth, away from the Sun. The idea of using the pressure of sunlight on a large solar sail to push the orbit of a geostationary satellite above or below the usual geostationary ring around the Earth was first proposed by Forward [108, 109]. By tilting the solar sail, Forward uses a component of sail acceleration normal to the Earth's equatorial plane to "levitate" the sail above or below the Earth's equatorial plane. In the following, Fischer and Haerting [110], and later [111] claim such light-levitation is not possible, as the component of sail acceleration neglected by Forward in [108, 109] parallel to the Earth's equatorial plane does not allow for equilibria. More recently, Baig and McInnes [112] use the neglected parallel component to generate a new family of NKO for solar sail spacecraft displaced above or below the Earth's equatorial plane. Although the existence of levitated geostationary orbits is demonstrated as proposed by Forward [108, 109], only modest displacements are found due to the large in-plane component of sail acceleration. These new, displaced orbits would allow more communication satellites to be stacked north or south of the Earth's equator, allowing additional satellites to be deployed to meet the growing demand for communications.

In the last decade, various solar sail rendezvous missions with a comet or asteroid have been studied. Thus, a number of mechanisms have been proposed for deflecting potentially hazardous Near Earth Objects (NEOs) [113, 114, 115, 116, 117, 118, 119]. The study of solar sailing mission applications to such a complex problem of changing the trajectory of NEOs to mitigate their impact threat to the Earth is not straightforward. The largest uncertainty in risk analysis arises from our incomplete knowledge of asteroids whose orbits bring them near to the Earth. The kinetic impact approach for mitigating the threat of asteroids has the risk that the impact could result in the fragmentation of the asteroid. Thus, Lu and Love [120] have recently proposed the use of gravitational coupling to modify the asteroid's orbit using a spacecraft with continuous low thrust propulsion. This concept implies that the spacecraft hovers in static equilibrium near the NEO surface. The control of a spacecraft hovering over a rotating small body, such as an asteroid or comet, has been analysed by Broschart and Scheeres [121]. In the following, McInnes [122] proposed the use of a displaced non-Keplerian orbit rather than a static hovering, which requires that the spacecraft exhaust plume be canted to avoid plume impingement on the NEO surface.

2.1.2 Solar Radiation Pressure Model

A spacecraft orbiting a planet, or the Sun, at a certain distance of r from the Sun will be affected by the solar radiation pressure unless it happens to be in the shadow of the planet. In addition to carrying energy, light particles (photons) transport momentum and are capable of exerting mechanical forces on a solar sail. According to Maxwell's electromagnetic theory, electromagnetic waves carry energy and linear momentum, that is transported to the solar sail. Thus, the radiation pressure P exerted on the surface of the

sail of area A by the impact of reflected photons is defined as the momentum transported per unit of area and time. The radiation pressure P (exerted on a perfectly absorbing surface) at a distance r from the Sun due to the momentum transport by solar photons is

$$P = \frac{W}{c}, \tag{2.1}$$

where W is the energy flux (or the energy crossing unit area in unit time) and c is the speed of light. The radiation pressure exerted on a perfectly reflecting surface due to the momentum transferred to the surface by the incident photons and the reflected photons is twice the value provided by equation (2.1).

The energy flux taken at a distance r from the Sun can be written in terms of the luminosity of Sun and the Sun-Earth distance $R_E = 1AU$,

$$W = W_E \left(\frac{R_E}{r}\right)^2, \tag{2.2}$$

$$W_E = \frac{L_S}{4\pi R_E^2}, \tag{2.3}$$

where W_E is the energy flux measured at the Earth'distance from the Sun and L_S is the solar luminosity.

Substituting equation (2.2) into equation (2.1), the radiation pressure is expressed as

$$P = \frac{W_E}{c}\left(\frac{R_E}{r}\right)^2. \tag{2.4}$$

The energy flux and so radiation pressure varies in proportion to the inverse square of the distance from the Sun. An accepted mean value for the energy flux at Sun-Earth distance $R_E = 1AU$ is the solar constant $W_E = 1368 Js^{-1}m^{-2}$. For a perfectly reflecting solar sail, the solar radiation pressure force per unit area (at a distance of one astronomical unit AU) is then $P_E = 4.56 \times 10^{-6} Nm^{-2}$.

2.1.3 Force on a Perfectly Reflecting Solar Sail

An ideal, perfectly reflecting, flat solar sail is assumed in this Section. The ideal sail model requires that the solar radiation pressure is perfectly reflected from the surface of the sail.

From Figure 2.3, the forces acting on the sail of area A due to photons incident from the $\boldsymbol{u}_i$ direction can be expressed as

$$\boldsymbol{F}_i = PA\langle \boldsymbol{u}_i, \boldsymbol{n}\rangle \boldsymbol{u}_i, \tag{2.5}$$

where P is the solar radiation pressure, $\boldsymbol{n}$ is a unit vector directed normal to the surface of the sail and $A\langle \boldsymbol{u}_i, \boldsymbol{n}\rangle$ is the projected area of the sail in the $\boldsymbol{u}_i$ direction. The force exerted on the sail due to the reflected photons is given by

$$\boldsymbol{F}_r = -PA\langle \boldsymbol{u}_r, \boldsymbol{n}\rangle \boldsymbol{u}_r. \tag{2.6}$$

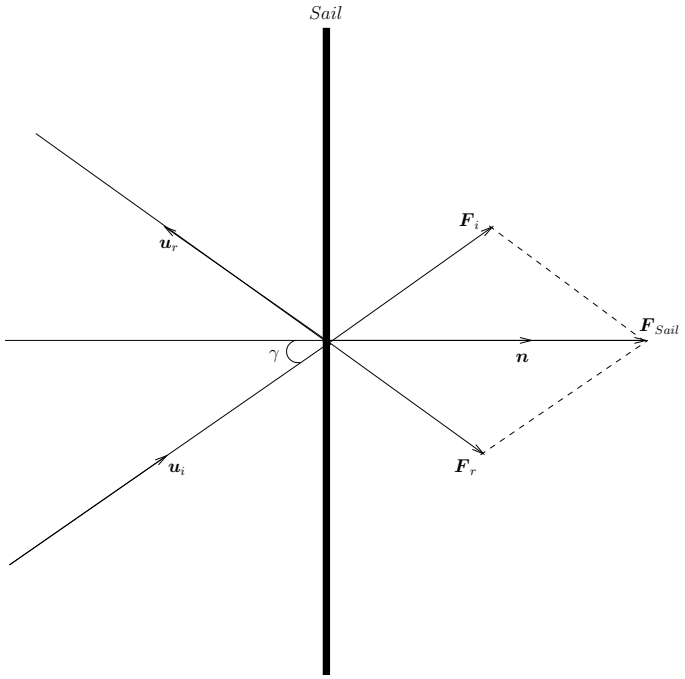

Figure 2.3: Representative forces on a perfectly reflecting solar sail.

It should be noted that $\boldsymbol{u}_i$ and $\boldsymbol{u}_r$ are the unit vectors along the direction of the incident and the reflected photons.

By making use of the vector identity $\boldsymbol{u}_i - \boldsymbol{u}_r = 2\langle \boldsymbol{u}_i, \boldsymbol{n}\rangle \boldsymbol{n}$, the total force acting on a perfectly reflecting solar sail can be expressed as

$$\boldsymbol{F}_{Sail} = \boldsymbol{F}_i + \boldsymbol{F}_r = 2PA\langle \boldsymbol{u}_i, \boldsymbol{n}\rangle^2 \boldsymbol{n}. \tag{2.7}$$

Thus, inserting equation (2.4) into equation (2.7), this total force can be written as

$$\boldsymbol{F}_{Sail} = \frac{2AW_E}{c}\left(\frac{R_E}{r}\right)^2 \langle \boldsymbol{u}_i, \boldsymbol{n}\rangle^2 \boldsymbol{n}. \tag{2.8}$$

Therefore, the total force vector on a perfectly reflecting solar sail of mass M_S, at a distance r from the Sun may now be written as

$$\boldsymbol{F}_{Sail} = \frac{2PM_S}{\sigma}\left(\frac{R_E}{r}\right)^2 \langle \boldsymbol{u}_i, \boldsymbol{n}\rangle^2 \boldsymbol{n}, \tag{2.9}$$

where σ is the sail loading parameter defined as the ratio of the sail mass to sail area. This constant will be used as a key design parameter to define the solar sail lightness number and the characteristic acceleration in Section 2.1.4.

The solar sail acceleration is obtained by dividing the total force by the sail mass M_S.

This results in the following sail acceleration

$$\begin{aligned} \boldsymbol{a}_{Sail} &= \frac{2W_E}{c}\frac{1}{\sigma}\left(\frac{R_E}{r}\right)^2 \langle \boldsymbol{u}_i, \boldsymbol{n}\rangle^2 \boldsymbol{n}, \\ &= \frac{2W_E}{c}\frac{1}{\sigma}\left(\frac{R_E}{r}\right)^2 \cos^2(\gamma)\boldsymbol{n}, \end{aligned} \tag{2.10}$$

where the sail pitch angle γ will be defined as the angle between the sail normal and the incident radiation, as shown in Figure 2.3.

2.1.4 Sail Performance Parameters

The **sail lightness number** β is defined as the ratio of solar radiation pressure acceleration to the solar gravitational acceleration. Then, introducing the sail lightness number, the solar sail acceleration can also be written in terms of the solar gravitational acceleration. The acceleration of the sail due to an ideal solar sail (flat and perfectly reflecting solar sail) can be expressed as

$$\boldsymbol{a}_{Sail} = \beta\frac{GM_S}{r^2}\langle \hat{\boldsymbol{r}}, \boldsymbol{n}\rangle^2 \boldsymbol{n}, \tag{2.11}$$

where M_S is the mass of the Sun and G is the universal gravitational constant. The unit radial vector $\hat{\boldsymbol{r}}$ is used to define the direction of incidence of the radiation $\boldsymbol{u}_i$ for a solar sail in a heliocentric orbit.

Then, using equations (2.10), (2.11) and (2.3), the solar sail lightness number can be written as

$$\beta = \frac{\sigma^\star}{\sigma}, \tag{2.12}$$

where the critical solar sail loading parameter is given by

$$\sigma^\star = \frac{L_s}{2\pi GM_S c} \approx 1.53 g m^{-2}. \tag{2.13}$$

As already mentioned in Section 2.1.3, the sail loading σ is defined as the ratio of the mass and sail area

$$\sigma = \frac{m}{A}. \tag{2.14}$$

The **characteristic acceleration** of the solar sail a_0 is defined as the acceleration experienced by the sail at 1 AU (astronomical unit) aligned normal to the Sun direction such that $\gamma = 0$. Thus, from the equation (2.7), the characteristic acceleration for an ideal sail can be expressed as

$$\begin{aligned} a_0 &= \frac{2PA}{m}, \\ &= \frac{2P}{\sigma}. \end{aligned} \tag{2.15}$$

Therefore, the characteristic acceleration of the solar sail a_0 is an equivalent design parameter to the solar sail loading σ. The non-ideal flat model (see Section 2.1.5) includes a sail efficiency to allow for the finite reflectivity of the sail film and sail billowing ($\eta \approx 0.9$), and so the characteristic acceleration may now be written as

$$a_0 = \frac{9.12\eta}{\sigma} m m^{-2}. \tag{2.16}$$

2.1.5 Force on a Non-Perfectly Reflecting Solar Sail

The assumption of an ideal flat solar sail can render the model inaccurate, since for a realistic solar sail the effects of an imperfect reflector can be considered in the model. A significant feature for the non-perfect flat solar sail is that the so-called cone angle reaches a maximum, limiting the operational range of the solar sail, whereas for the ideal sail the thrust vector is always oriented normal to the sail surface and can in principle be operated up to a 90° Sun angle ($-\pi/2 \leq \gamma \leq \pi/2$). In the previous sections, it was assumed implicitly that the solar sail is a perfect reflector. Thus, by adding the force due to the incident and reflected photons, the resulting force exerted on the solar sail is directed normal to the sail surface. This is in contrast to the non-ideal flat sail model, where one component of the force is along the sail surface, and so the combined force is no longer normal to the sail surface as shown in Figure 2.4. As can be seen in Figure 2.4, the force exerted on the solar sail has a normal component F_n and a transversal component F_t defined in reference [4]. By making use of the reflectance, absorption and emissitivity of the sail film, the total force acting on the solar sail due to the solar radiation pressure is given by

$$\boldsymbol{F}_{Sail} = \boldsymbol{F}_r + \boldsymbol{F}_a + \boldsymbol{F}_e, \tag{2.17}$$

where the force due to reflection $\boldsymbol{F}_r$ is the sum of a fraction s due to specular reflection acting along the normal and the transverse directions denoted by $\boldsymbol{F}_{ru_i}$, and a fraction $B_f(1-s)$ due to diffuse reflection acting along the normal direction denoted by $\boldsymbol{F}_{ru_r}$. It should be noted that B_f is the non-Lambertian coefficient of the front surface of the sail, i.e. a surface which doesn't appear equally bright when viewed from any aspect angle [123]. The force due to absorption is denoted by $\boldsymbol{F}_a$ and the force $\boldsymbol{F}_e$ from re-radiated photons as would be computed from thermodynamics will be defined by a vector $\boldsymbol{n}$ normal to the sail surface. The total force will depend upon the optical characteristics of the sail film, which can be parameterised by the reflection coefficient $\tilde{\rho}$, the absorption coefficient a and the transmission coefficient τ such that

$$\tilde{\rho} + a + \tau = 1. \tag{2.18}$$

Since the transmission coefficient $\tau = 0$ on the reflecting side of the sail, the absorption coefficient is given by

$$a = 1 - \tilde{\rho}. \tag{2.19}$$

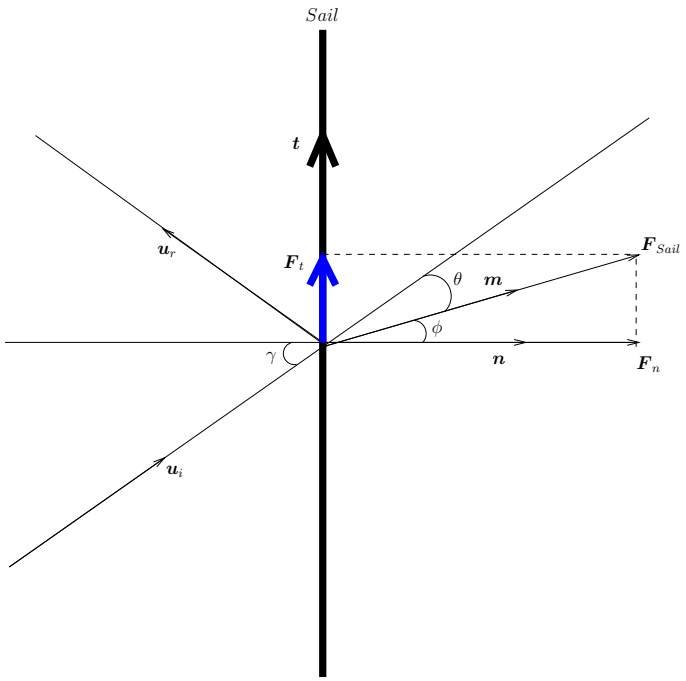

Figure 2.4: Representative forces on a non-perfectly reflecting solar sail.

The direction of incidence of photons will be defined by a unit vector $\boldsymbol{u}_i$ and the direction of specularly reflected photons by a unit vector $\boldsymbol{u}_r$.

The force exerted on the solar sail due to absorbed photons is

$$\begin{aligned} \boldsymbol{F}_a &= PA\cos(\gamma)\boldsymbol{u}_i, \\ &= PA\cos(\gamma)\big[\cos(\gamma)\boldsymbol{n} + \sin(\gamma)\boldsymbol{t}\big], \end{aligned} \tag{2.20}$$

where $A\cos(\gamma)$ is the projected sail area directed along a unit vector $\boldsymbol{u}_i$, and the solar sail orientation is again defined by a vector $\boldsymbol{n}$ normal to the sail surface with a transverse unit vector $\boldsymbol{t}$ perpendicular to $\boldsymbol{n}$, as shown in Figure 2.4.

Of the incident photons, a fraction $\tilde{\rho}$ is reflected. A fraction s of that fraction of photons is specularly reflected, providing a force $\boldsymbol{F}_{ru_i}$ in the $-\boldsymbol{u}_r$ direction given by

$$\begin{aligned} \boldsymbol{F}_{ru_i} &= -(\tilde{\rho}s)PA\cos(\gamma)\boldsymbol{u}_r, \\ &= -(\tilde{\rho}s)PA\cos(\gamma)\big[-\cos(\gamma)\boldsymbol{n} + \sin(\gamma)\boldsymbol{t}\big]. \end{aligned} \tag{2.21}$$

Another fraction of incident photons non-specularly reflected creates a force $\boldsymbol{F}_{ru_r}$ in the $\boldsymbol{n}$ direction given by

$$\boldsymbol{F}_{ru_r} = PA(1-s)B_f\tilde{\rho}\cos(\gamma)\boldsymbol{n}. \tag{2.22}$$

The total force due to reflected photons in terms of the normal and transverse directions is then

$$\begin{aligned} \boldsymbol{F}_r &= \boldsymbol{F}_{ru_i} + \boldsymbol{F}_{ru_r}, \\ &= PA\big[\big(\tilde{\rho}s\cos^2(\gamma) + B_f(1-s)\tilde{\rho}\cos(\gamma)\big)\boldsymbol{n} - \tilde{\rho}s\cos(\gamma)\sin(\gamma)\boldsymbol{t}\big]. \end{aligned} \tag{2.23}$$

The force exerted on the sail surface through emission by re-radiation and the temperature of the solar sail film can then be calculated. The power emitted from a unit area of the sail at temperature T is $\varepsilon\tilde{\sigma}T^4$, where ε is the surface emissivity and $\tilde{\sigma}$ is the Stefan-Boltzmann constant. Assuming that the sail has uniform temperature, and allowing the non-Lambertian nature of the front and back sail surfaces, the force exerted on the solar sail due to emission by re-radiation can be written as

$$\boldsymbol{F}_e = (\varepsilon_f B_f - \varepsilon_b B_b)\frac{\tilde{\sigma}T^4}{c}\boldsymbol{n}, \tag{2.24}$$

where ε_f and ε_b are the front and back emissivities respectively, B_b is the non-Lambertian coefficient of the back surface and T is the absolute temperature of the sail.

The thermal input and output to the sail can be expressed respectively as

$$Ther_{in} = (1-\tilde{\rho})W\cos(\gamma), \tag{2.25}$$

$$Ther_{out} = (\varepsilon_f + \varepsilon_b)\tilde{\sigma}T^4, \tag{2.26}$$

where W is the solar flux incident on the sail.

From the balance between the thermal input and the thermal output as defined in reference [4], it can be seen that

$$(1-\tilde{\rho})W\cos(\gamma) - (\varepsilon_f + \varepsilon_b)\tilde{\sigma}T^4 = 0, \tag{2.27}$$

and considering the radiation pressure $P = W/c$, the sail equilibrium absolute temperature T and the forced exerted on the solar sail due to emission by re-radiation $\boldsymbol{F}_e$ can be calculated. Thus, equation (2.27) becomes

$$T = \left[\frac{1-\tilde{\rho}}{\varepsilon_f + \varepsilon_b}\frac{c}{\tilde{\sigma}}P\cos(\gamma)\right]^{1/4}, \tag{2.28}$$

and equation (2.24) can now be rewritten as

$$\boldsymbol{F}_e = PA(1-\tilde{\rho})\frac{\varepsilon_f B_f - \varepsilon_b B_b}{\epsilon_f + \varepsilon_b}\cos(\gamma)\boldsymbol{n}. \tag{2.29}$$

The total force exerted on the solar sail is obtained after decomposing the forces involved into their normal and transverse components as

$$\begin{aligned} \boldsymbol{F}_n &= PA\Big[(1+\tilde{\rho}s)\cos^2(\gamma) + B_f(1-s)\tilde{\rho}\cos(\gamma) \\ &\quad +(1-\tilde{\rho})\frac{\varepsilon_f B_f - \varepsilon_b B_b}{\varepsilon_f + \varepsilon_b}\cos(\gamma)\Big]\boldsymbol{n}, \end{aligned} \tag{2.30}$$

$$\boldsymbol{F}_t = PA(1-\tilde{\rho}s)\cos(\gamma)\sin(\gamma)\boldsymbol{t}. \tag{2.31}$$

Thus, equations (2.30) and (2.31) can be reduced to

$$\boldsymbol{F}_n = PA\big[a_1\cos^2(\gamma) + a_2\cos(\gamma)\big]\boldsymbol{n}, \tag{2.32}$$

$$\boldsymbol{F}_t = PAa_3\cos(\gamma)\sin(\gamma)\boldsymbol{t}, \tag{2.33}$$

where the optical properties of the sail film are given by the coefficients

$$a_1 = 1+\tilde{\rho}s, \tag{2.34}$$

$$a_2 = B_f(1-s)\tilde{\rho} + (1-\tilde{\rho})\frac{\varepsilon_f B_f - \varepsilon_b B_b}{\varepsilon_f + \varepsilon_b}, \tag{2.35}$$

$$a_3 = 1-\tilde{\rho}s. \tag{2.36}$$

The total force vector may then be written in terms of normal and transversal components as

$$\begin{aligned} \boldsymbol{F}_{Sail} &= \sqrt{F_n^2 + F_t^2}\boldsymbol{m}, \\ &= PA\sqrt{(a_1\cos(\gamma)+a_2)^2 + a_3^2\sin^2(\gamma)}\cos(\gamma)\boldsymbol{m}, \end{aligned} \tag{2.37}$$

where $\boldsymbol{m}$ is the unit vector in the direction of the total force, as shown in Figure 2.4.

For an ideal sail (i.e. a perflect reflector) $\tilde{\rho} = s = 1$, hence $a_1 = 2$, $a_2 = a_3 = 0$, and the total force exerted on the solar sail is given by

$$\boldsymbol{F}_{Sail} = 2PA\cos^2(\gamma)\boldsymbol{n}, \tag{2.38}$$

with $\boldsymbol{n}$=$\boldsymbol{m}$.

As already noted in Section 2.1.3, the direction of incidence of photons is defined by a unit vector $\boldsymbol{u}_i$ and the direction of specularly reflected photons by a unit vector $\boldsymbol{u}_r$. The solar sail orientation is defined by a vector $\boldsymbol{n}$ normal to the sail surface with a transverse unit vector $\boldsymbol{t}$ perpendicular to $\boldsymbol{n}$. The angle between $\boldsymbol{m}$ and $\boldsymbol{u}_i$ is defined by the cone angle θ and the angle between $\boldsymbol{m}$ and $\boldsymbol{n}$ is called center-line angle ϕ, and γ is again the pitch angle of the solar sail relative to the Sun-line, as shown in Figure 2.4.

The center-line angle is given by

$$\begin{aligned} \phi &= \arctan\left(\frac{F_t}{F_n}\right), \\ &= \arctan\left(\frac{a_3 \sin(\gamma)}{a_1 \cos(\gamma) + a_2}\right), \end{aligned} \tag{2.39}$$

while the cone angle θ can be calculated using the relation $\gamma = \theta + \phi$, again shown in Figure 2.4.

The cone angle can then be expressed as

$$\theta = \gamma - \arctan\left(\frac{a_3 \sin(\gamma)}{a_1 \cos(\gamma) + a_2}\right). \tag{2.40}$$

Table 2.1: NSTAR end-of-life engine performance after 8000 h of operation at 2.3 kW. ‡

Engine input power (kW)	*Thrust* (mN)	I_{sp} (s)	$Efficiency$
2.32	92.3	3313	0.646
2.08	83.3	3293	0.645
1.67	66.1	3291	0.640
1.37	52.8	3300	0.622
0.93	34.8	2974	0.544
0.57	21.8	2188	0.409

‡ Data source reference [124].

2.2 Solar Electric Propulsion System

Several propulsion concepts are being developed to significantly enhance near-term capabilities for deep space exploration [125, 126, 127, 128, 129, 130, 131, 132, 133, 134]. The most mature of these is solar electric propulsion. The two objectives for near- and mid-term electric propulsion technology improvements for deep-space missions are to reduce the total mission life cycle costs and flight times. The SEP system is a type of propulsion system which utilises electric (and/or magnetic processes) to accelerate a propellant at a much higher exhaust speed than the classical chemical propulsion. Such electric propulsion devices are capable of producing specific impulses ranging from approximately 1500 to 4000 *sec*, compared to chemical systems which typically operate over the range of 300 to 400 *sec*. Solar electric propulsion has been utilised in numerous communications satellites and a few deep space missions, such as Deep Space 1, SMART-1 and Hayabusa from the Japanese Aerospace Exploration Agency (JAXA) [135]. The ion propulsion system for Deep Space 1 [12, 13] is the NSTAR (NASA solar electric propulpsion technology applications readiness) and is based on the NASA 30-cm-diam engine, as shown in Figure 2.5 (b). Figure 2.6 depicts a schematic of the thruster configuration §, and the end-of-life performance of the NSTAR ion engine after 8000 h of operation at full power is given in Table 2.1. The spacecraft SMART-1 [137], as shown in Figure 2.5 (a), is a lunar orbiter belonging to the European Space Agency (ESA). SMART-1 was designed to demonstrate the use of electric propulsion on a small mission. It should be noted that ion thrusters are currently used for station-keeping on communication satellites and orbit insertion.

§Figure 2.6 can be found in reference [136].

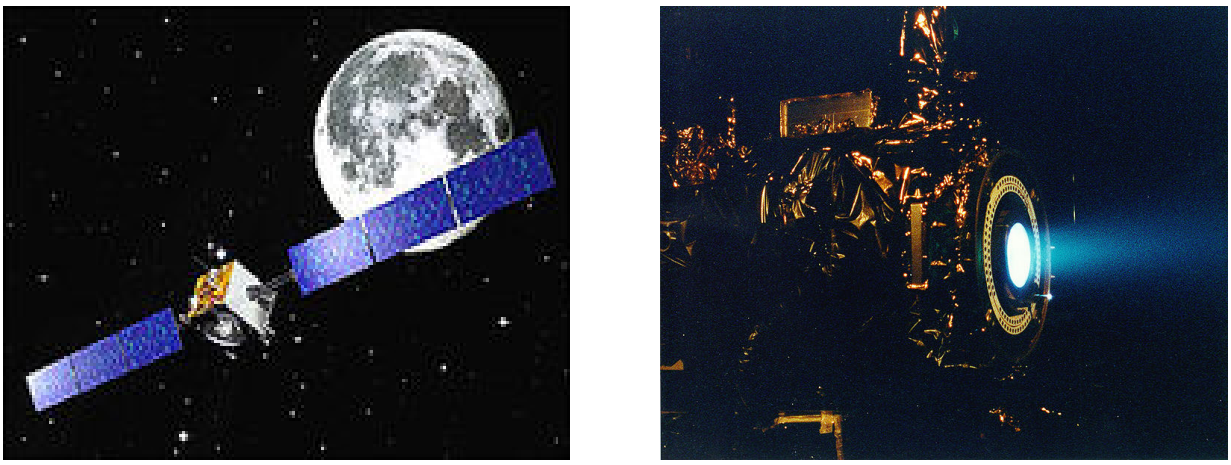

(*a*) (*b*)

Figure 2.5: (a) Artist impression of Smart-1 (ESA); (b) NSTAR Ion Engine used on Deep Space 1 (NASA).

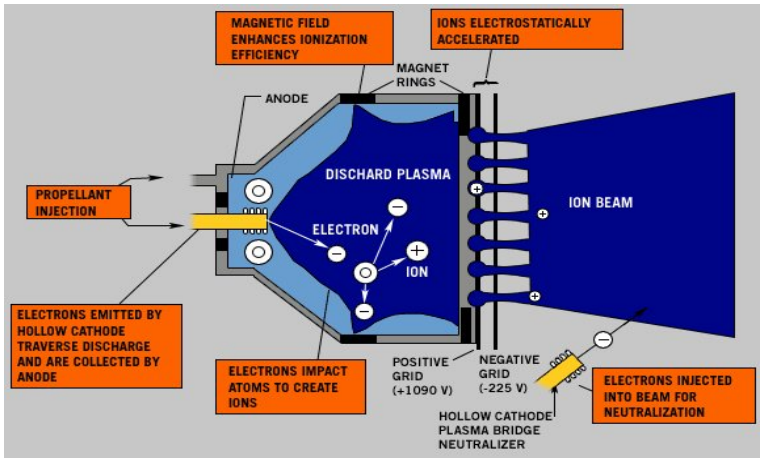

Figure 2.6: Ion thruster component technologies.

2.3 Chemical Propulsion System

Chemical propulsion uses energy produced by a chemical reaction to generate gases at high temperature and pressure in a combustion chamber. The hot gases are then accelerated through a nozzle and ejected from the system at a high exit velocity to produce thrust. Chemical propulsion systems have performed well in traditional near-Earth or deep space missions, but the relatively low energy they deliver for a given propellant mass imposes severe restrictions. With specific impulses in the range of 300 and 400 *sec*, they are capable of exerting a substantial force on the spacecraft, but expend a great deal of propellant. This is in contrast to electric propulsion thrusters, which create significantly less thrust and expend much less propellant in doing so. Thus, electric propulsion thrusters use propellant much more efficiently than chemical propulsion thrusters. For this reason, electric propulsion thrusters are more desirable for station-keeping and maneuvering, since they require minimal thrust to reposition the spacecraft.

2.4 Hybrid Electric Propulsion System

The idea of combining a solar sail with an auxiliary SEP system to obtain a hybrid sail system is important due to the challenges of performing complex missions (see Leipold and Götz [138], Mengali and Quarta [139, 140], Dachwald [141]). Baig and McInnes [142] proposed a new concept of creating artificial equilibria above L_1 point in the Sun-Earth system for Earth observation, in which the third body uses a hybrid of solar sail and SEP. The solar electric propulsion system possesses high specific impulse ($I_{sp} \approx 3000$ *sec*). SEP consumes propellant and decreases the mass of the spacecraft, whereas the solar sail does not consume any propellant. This form of propulsion is useful for some high energy missions, but unlike solar sails, they have a finite ΔV capability, which makes them unsuitable for missions where a non-Keplerian orbit has to be maintained over indefinite periods of time.

When performing analysis in the CRTBP, most of the analytical and numerical solutions generated have resulted from models that include only the gravitational attraction of the two massive bodies. However, the addition of the force from solar sail, solar electric or chemical propulsion leads to interesting new solutions. The CRTBP serves as the basis in the development of the equations of motion used in this thesis and will be introduced in Chapter 3.

Chapter 3

Circular Restricted Three-Body Problem

In this Chapter, the main features of the three-body problem which are important for the discussion in later chapters will be detailed. Thus, the three bodies are assumed to have spherically symmetric gravity fields such that each body can be modeled as a point mass. A special case of interest is the circular restricted three-body problem (CRTBP), in which the primaries are further constrained to rotate about their center of mass in circular orbits and the third mass is assumed to be infinitesimal.

3.1 The Restricted Three-Body Problem

The three-body problem has been the focus of much mathematical and scientific interest. The problem studies the motion of three bodies moving under the gravitational influence of each other. While no general closed-form solution to this problem is found, it is possible to make a number of simplifying assumptions which can help to obtain approximations to the actual motion. Thus, the model of the restricted three-body problem has been used extensively in the study of problems of celestial mechanics (Szebehely, 1967 [44], Roy, 1982 [45]). In the restricted three-body problem, one of the masses is taken to be negligibly small so that the problem simplifies to finding the behavior of the massless body in the combined gravitational field of the other two, i.e, the mass m_3 of the third body denoted as P_3 is negligible compared to the masses of the two primaries. The two primary bodies are denoted as P_1 and P_2 with respective masses m_1 and m_2, where m_2 is assumed to be the smaller mass as defined in Figure 3.1 ($m_1 > m_2 >> m_3$). The spacecraft (massless body) is free to move in all three spatial directions without constraints. If the two primary bodies move on elliptic paths relative to their barycenter, then the problem is reduced to the elliptic restricted three-body problem.

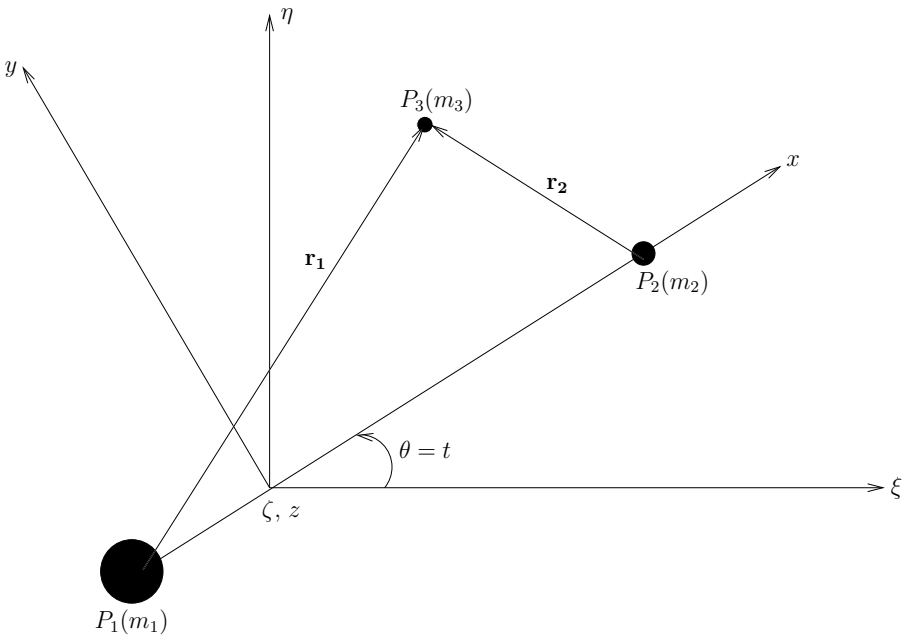

Figure 3.1: Geometry of the circular restricted three-body problem.

3.2 The Circular Restricted Three-Body Problem

The circular restricted three-body problem (CRTBP) describes the dynamics of a massless body attracted by two point masses revolving around each other in a circular orbit. In the CRTBP, the motion of a particle (spacecraft) of negligible mass is considered moving under the gravitational influence of two massive bodies, defined as the primaries. It is assumed that the two primaries rotate in circular orbits about their common center of mass. The center of mass is located at the barycenter on the line joining the primaries [143, 144, 145]. The system of interest in this thesis is the Earth-Moon system such that m_1 represents the Earth and m_2 represents the Moon, and the motion of a spacecraft of much smaller mass is considered.

3.2.1 Dimensionless Quantities

In order to develop any mathematical model without loss of the generality, it is useful to introduce some parameters that are characteristics of each particular three-body system. This set of parameters is used to normalise the equations of motion. The unit of mass is taken to be the total mass of the system $(m_1 + m_2)$ and the unit of length is chosen to be the constant separation between m_1 and m_2. The unit of time is chosen such that the orbital period of m_1 and m_2 about their center of mass is 2π. Thus, the universal constant of gravitation becomes $G = 1$. Under these considerations the masses of the primaries in the normalised system of units are $m_1 = 1 - \mu$ and $m_2 = \mu$, where μ is the dimensionless

mass of the smaller primary defined by

$$\mu = \frac{m_2}{m_1 + m_2}. \tag{3.1}$$

Hence, the dimensionless mass of the larger primary is given by

$$1 - \mu = \frac{m_1}{m_1 + m_2}. \tag{3.2}$$

3.2.2 Equations of Motion

Consider three point masses moving in an inertial Newtonian reference system, with the only force acting on them being their mutual gravitational attractions. From Newton's second law of motion, the equation of motion of each body can be described by the following differential equation

$$m_i \ddot{\boldsymbol{r}}_i = \sum_{j=1,\ j\neq i}^{3} \frac{G m_i m_j}{r_{ji}^3} \boldsymbol{r}_{ji} \quad for \quad i = 1, 2, 3, \tag{3.3}$$

where G is the gravitational constant, and the position vector of P_i relative to P_j is given by $\boldsymbol{r}_{ji} = \boldsymbol{r}_i - \boldsymbol{r}_j$.

In order to examine the motion of the bodies in greater detail, it is useful to look at the equations in terms of the variables shown in Figure 3.1. The inertial coordinate system (ξ, η, ζ) and the rotating coordinate system (x, y, z) will be used in subsequent chapters to derive the equations of motion. Let (ξ_1, η_1, ζ_1) and (ξ_2, η_2, ζ_2) be the nondimensional coordinates of P_1 and P_2 respectively, the equations of motion of an infinitesimal particle are given by

$$\frac{d^2\xi}{dt^2} = \frac{1-\mu}{r_1^3}(\xi_1 - \xi) + \frac{\mu}{r_2^3}(\xi_2 - \xi), \tag{3.4}$$

$$\frac{d^2\eta}{dt^2} = \frac{1-\mu}{r_1^3}(\eta_1 - \eta) + \frac{\mu}{r_2^3}(\eta_2 - \eta), \tag{3.5}$$

$$\frac{d^2\zeta}{dt^2} = \frac{1-\mu}{r_1^3}(\zeta_1 - \zeta) + \frac{\mu}{r_2^3}(\zeta_2 - \zeta), \tag{3.6}$$

where r_1 and r_2 are equal to the distance from the third body to the primary and secondary, respectively

$$r_1 = \sqrt{(\xi - \xi_1)^2 + (\eta - \eta_1)^2 + (\zeta - \zeta_1)^2}, \tag{3.7}$$

$$r_2 = \sqrt{(\xi - \xi_2)^2 + (\eta - \eta_2)^2 + (\zeta - \zeta_2)^2}. \tag{3.8}$$

3.2.3 Transformation between the Inertial and Rotating Frames

In Figure 3.1, the rotating coordinate system with coordinates x, y and z moves counterclockwise with unit angular velocity relative to the inertial frame with coordinates ξ, η and ζ. Let (ξ, η, ζ) and (x, y, z) be the position of the infinitesimal mass in the inertial and rotating frames, respectively. In normalised units, the transformation of the particle's position between the two frames is given by

$$\begin{bmatrix} \xi \\ \eta \\ \zeta \end{bmatrix} = R_t \begin{bmatrix} x \\ y \\ z \end{bmatrix}, \tag{3.9}$$

where

$$R_t = \begin{bmatrix} \cos(t) & -\sin(t) & 0 \\ \sin(t) & \cos(t) & 0 \\ 0 & 0 & 1 \end{bmatrix} \tag{3.10}$$

denotes the matrix of rotation (counterclockwise) by angle $\theta = t$ about the z-axis, as shown in Figure 3.1.

Differentiating gives

$$\begin{aligned} \dot{\xi} &= \dot{x}\cos(t) - x\sin(t) - \dot{y}\sin(t) - y\cos(t), && (3.11)\\ \dot{\eta} &= \dot{x}\sin(t) + x\cos(t) + \dot{y}\cos(t) - y\sin(t), && (3.12)\\ \dot{\zeta} &= \dot{z}. && (3.13) \end{aligned}$$

$$\begin{aligned} \ddot{\xi} &= (\ddot{x} - 2\dot{y} - x)\cos(t) - (\ddot{y} + 2\dot{x} - y)\sin(t), && (3.14)\\ \ddot{\eta} &= (\ddot{x} - 2\dot{y} - x)\sin(t) - (\ddot{y} + 2\dot{x} - y)\cos(t), && (3.15)\\ \ddot{\zeta} &= \ddot{z}, && (3.16) \end{aligned}$$

and substituting the resulting expressions into equation ((3.4)-(3.6)), it can be seen that

$$(\ddot{x} - 2\dot{y} - x)\cos(t) - (\ddot{y} + 2\dot{x} - y)\sin(t) = -\left(\frac{1-\mu}{r_1^3}(x - x_1) + \frac{\mu}{r_2^3}(x - x_2)\right)\cos(t) + \left(\frac{1-\mu}{r_1^3}(y - y_1) + \frac{\mu}{r_2^3}(y - y_2)\right)\sin(t), \tag{3.17}$$

$$(\ddot{x} - 2\dot{y} - x)\sin(t) - (\ddot{y} + 2\dot{x} - y)\cos(t) = -\left(\frac{1-\mu}{r_1^3}(x - x_1) + \frac{\mu}{r_2^3}(x - x_2)\right)\sin(t) - \left(\frac{1-\mu}{r_1^3}(y - y_1) + \frac{\mu}{r_2^3}(y - y_2)\right)\cos(t), \tag{3.18}$$

$$\ddot{z} = -\left(\frac{1-\mu}{r_1^3} + \frac{\mu}{r_2^3}\right)z. \tag{3.19}$$

The resulting nondimensional equations that govern the motion of the infinitesimal mass in the CRTBP are then found to be

$$\ddot{x} - 2\dot{y} = x - \frac{1-\mu}{r_1^3}(x - x_1) - \frac{\mu}{r_2^3}(x - x_2), \tag{3.20}$$

$$\ddot{y} + 2\dot{x} = \left(1 - \frac{1-\mu}{r_1^3} + \frac{\mu}{r_2^3}\right)y, \tag{3.21}$$

$$\ddot{z} = -\left(\frac{1-\mu}{r_1^3} + \frac{\mu}{r_2^3}\right)z, \tag{3.22}$$

where r_1 and r_2 are given in rotating coordinates by

$$r_1 = \sqrt{(x - x_1)^2 + y^2 + z^2}, = \sqrt{(x + \mu)^2 + y^2 + z^2}, \tag{3.23}$$

$$r_2 = \sqrt{(x - x_2)^2 + y^2 + z^2}, = \sqrt{(x - 1 + \mu)^2 + y^2 + z^2}. \tag{3.24}$$

A pseudo-potential function is now obtained from the equations ((3.20)-(3.22)) as

$$U(x, y, z) = -\frac{1}{2}(x^2 + y^2) - \frac{1-\mu}{r_1} - \frac{\mu}{r_2}. \tag{3.25}$$

Thus, equations ((3.20)-(3.22)) can be rewritten in terms of the pseudo-potential as

$$\ddot{x} - 2\dot{y} = -\frac{\partial U}{\partial x}, \tag{3.26}$$

$$\ddot{y} + 2\dot{x} = -\frac{\partial U}{\partial y}, \tag{3.27}$$

$$\ddot{z} = -\frac{\partial U}{\partial z}. \tag{3.28}$$

3.2.4 Equilibrium Solutions

The libration points are the equilibrium solutions of the restricted three-body problem. There are five equilibrium points in the circular restricted three-body problem, known as libration or Lagrange points. The locations in the Earth-Moon system are indicated schematically in Figure 3.2, and summarised in Table 3.1.

The three collinear libration points have been found to exist on the x-axis. By setting the accelerations and the velocities equal to zero in the equation (3.20), it can be seen that

$$\begin{aligned} \frac{\partial U}{\partial x} &= x - \frac{1-\mu}{r_1^3}(x - x_1) - \frac{\mu}{r_2^3}(x - x_2) = 0, \\ &= x - \frac{1-\mu}{r_1^3}(x + \mu) - \frac{\mu}{r_2^3}(x - 1 + \mu) = 0. \end{aligned} \tag{3.29}$$

Solving equation (3.29) for x, yields the three collinear libration points, that is $x_{L_1} = 1 - \mu - \alpha_{L_1}$, $x_{L_2} = 1 - \mu + \alpha_{L_2}$ and $x_{L_3} = -\mu - \alpha_{L_3}$. The distances α_{L_1}, α_{L_2}, and α_{L_3} are the equilibrium points relative to the primaries. The values for α_{L_1}, α_{L_2}, and α_{L_3} are given from the following fifth-order polynomials [44]

$$\begin{aligned} \alpha_{L_1}^5 - (3-\mu)\alpha_{L_1}^4 + (3-2\mu)\alpha_{L_1}^3 - \mu\alpha_{L_1}^2 + 2\mu\alpha_{L_1} - \mu &= 0, \\ \alpha_{L_2}^5 - (3-\mu)\alpha_{L_2}^4 + (3-2\mu)\alpha_{L_2}^3 - \mu\alpha_{L_2}^2 + 2\mu\alpha_{L_2} - \mu &= 0, \\ \alpha_{L_3}^5 - (2+\mu)\alpha_{L_3}^4 + (1+2\mu)\alpha_{L_3}^3 - (1-\mu)\alpha_{L_3}^2 - 2(1-\mu)\mu\alpha_{L_3} - (1-\mu) &= 0. \end{aligned} \tag{3.30}$$

By convention, L_1 lies between the two primaries, L_2 on the far side of the secondary in the positive x-direction and L_3 on the far side of the primary in the negative x-direction. Similarly, the triangular libration points L_4 and L_5 can be computed using the following relationship

$$\frac{\partial U}{\partial x} = \frac{\partial U}{\partial y} = 0. \tag{3.31}$$

These points form an equilateral triangle with the two primaries, which are found to be located at $r_1 = r_2 = 1$ so that $x = \frac{1}{2} - \mu$, $y = \pm\frac{\sqrt{3}}{2}$ and $z = 0$.

3.2.5 Jacobi's Constant and the Surfaces of Zero Relative Velocity

The Jacobi integral is the only integral of the motion that is known to exist for the CRTBP. Multiplying equations (3.26), (3.27) and (3.28) by $\dot{x}$, $\dot{y}$ and $\dot{z}$ respectively, and then adding, it is found that

$$\begin{aligned}
\ddot{x}\dot{x} + \ddot{y}\dot{y} + \ddot{z}\dot{z} &= -\frac{\partial U}{\partial x}\dot{x} - \frac{\partial U}{\partial y}\dot{y} - \frac{\partial U}{\partial z}\dot{z} = -\frac{dU}{dt}, && (3.32)\\
\frac{1}{2}\frac{d}{dt}(\dot{x}^2 + \dot{y}^2 + \dot{z}^2) &= -\frac{\partial U}{\partial x}\frac{dx}{dt} - \frac{\partial U}{\partial y}\frac{dy}{dt} - \frac{\partial U}{\partial z}\frac{dz}{dt} = -\frac{dU}{dt}, && (3.33)\\
\frac{1}{2}(\dot{x}^2 + \dot{y}^2 + \dot{z}^2 + C) &= -U(x, y, z), && (3.34)\\
\dot{x}^2 + \dot{y}^2 + \dot{z}^2 &= -2U(x, y, z) - C. && (3.35)
\end{aligned}$$

For a given position and velocity V in the rotating frame, the Jacobi constant can then be expressed as

$$\begin{aligned}
C &= -2U(x, y, z) - V^2,\\
&= x^2 + y^2 + \frac{2(1-\mu)}{r_1} + \frac{2\mu}{r_2} - (\dot{x}^2 + \dot{y}^2 + \dot{z}^2). && (3.36)
\end{aligned}$$

The Hamiltonian H, for the system described by equations (3.26)-(3.28) is given by

$$\begin{aligned}
H &= \frac{1}{2}(\dot{x}^2 + \dot{y}^2 + \dot{z}^2) - \frac{1}{2}(x^2 + y^2) - \frac{1-\mu}{r_1} - \frac{\mu}{r_2},\\
&= \frac{1}{2}V^2 + U(x, y, z). && (3.37)
\end{aligned}$$

This represents an energy-like quantity associated with the particle P_3 relative to the rotating frame. Thus, the Jacobi constant is related to the Hamiltonian through the equation $C = -2H$.

Let C_{L_i} be the value of the Jacobi constant at the libration points L_i $(i = 1 \cdots 5)$. The range of energy levels decreases such that $C_{L_1} > C_{L_2} > C_{L_3} > C_{L_4} = C_{L_5}$. The corresponding values are indicated in Table 3.2.

For a given Jacobi constant, the particle is not free to wander over the entire configuration space due to the constraint that the velocity must be positive, $V^2 \geq 0$, that

$$x^2 + y^2 + \frac{2(1-\mu)}{r_1} + \frac{2\mu}{r_2} \geq C. \tag{3.38}$$

Thus, the regions where the motion is forbidden are given by $-2U(x, y, z) - C < 0$, and the boundary of these volumes $(C = -2U(x, y, z))$ is typically referred to as zero-velocity surfaces. The zero-velocity curves are then obtained by setting the velocity in equation (3.36) equal to zero, and then mapping the resultant curves for positions near the primaries [45, 44, 146, 147, 148, 149].

Table 3.1: Earth-Moon equilibrium point locations [$].

Libration point	x_{Li}	y_{L_i}	z_{Li}
L_1	0.8369180073	0	0
L_2	1.1556799131	0	0
L_3	-1.0050624018	0	0
L_4	0.4876777420	$\frac{\sqrt{3}}{2}$	0
L_5	0.4876777420	$-\frac{\sqrt{3}}{2}$	0

[$] $\mu = 0.012150582$.

Table 3.2: Values of the Jacobi Constant in the Earth-Moon System.

Jacobi Constant	
C_{L_1}	3.188340
C_{L_2}	3.172160
C_{L_3}	3.012147
C_{L_4}	2.987997
C_{L_5}	2.987997

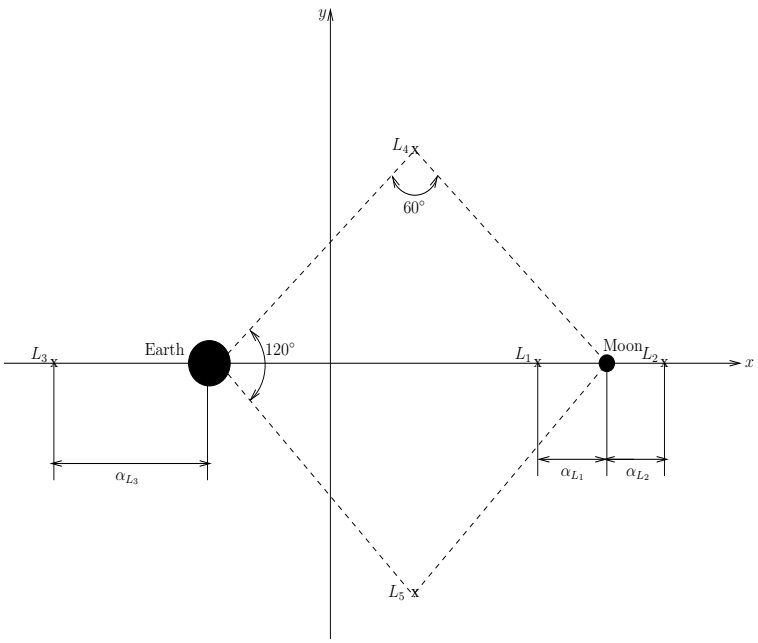

Figure 3.2: Schematic location of the five Lagrange points in the Earth-Moon System.

3.2.6 Periodic Orbits

As already noted, libration points are stationary equilibrium points. It is then possible to find bounded motion in the region of the libration points. The most general motion of this type to be produced in the vicinity of the libration points is a quasi-periodic trajectory. As will be shown in Chapter 4, one example of a bounded oscillatory, three-dimensional solution near the libration points is a Lissajous trajectory. The Halo orbit is then a special case of Lissajous orbit where the in-plane and out-of-plane frequencies are equal [150, 151]. Farquhar [152] first proposed a halo orbit near the translunar libration point for a single communications satellite to link the Earth with the far side of the Moon. If the orbit is in the plane of motion of the primaries, it is referred to as a Lyapunov orbit.

Chapter 4

Linearised Motion Relative to the Libration Points

The families of periodic orbits described in this Chapter exhibit different types of configurations. General analytical solutions at linear order to the three-body problem are derived. The shapes of the periodic orbits associated to the Earth-Moon libration points will then be considered. The orbit size is represented by the input amplitudes. While not intended to be a complete investigation, a sample Lissajous orbit in the vicinity of the L_1 libration point is computed in the Earth-Moon system. Then, the result is applicable to orbits around the remaining libration points.

4.1 Linear Approximation Relative to the Libration Points

The goal of this section is to determine the relationships that exist between the analytical solutions driven only by the gravitational forces and those evaluated when the control accelerations are later incorporated.

The linearised equations of motion are obtained by pertubing the state from the equilibrium solution. Let $\boldsymbol{r} \rightarrow \boldsymbol{r}_L + \delta\boldsymbol{r}$, where $\boldsymbol{r}_L = (x_{L_i}, y_{L_i}, z_{L_i})^T$ are the coordinates of the equilibrium point L_i $(i = 1, \cdots, 5)$, $\delta\boldsymbol{r} = (\delta x, \delta y, \delta y)^T = (\xi, \eta, \zeta)^T$ are the components of the position vector relative to the equilibrium point, as shown in Figure 4.1. The pertubed state relative to the equilibrium point is given by

$$x = x_{L_i} + \xi, \tag{4.1}$$

$$y = y_{L_i} + \eta, \tag{4.2}$$

$$z = z_{L_i} + \zeta. \tag{4.3}$$

From a Taylor series expansion about the equilibrium point, and retaining only the first-order terms, a linear system is obtained from the equation (3.20) to equation (3.22) as

$$\dot{\mathbf{X}} = A\mathbf{X}, \tag{4.4}$$

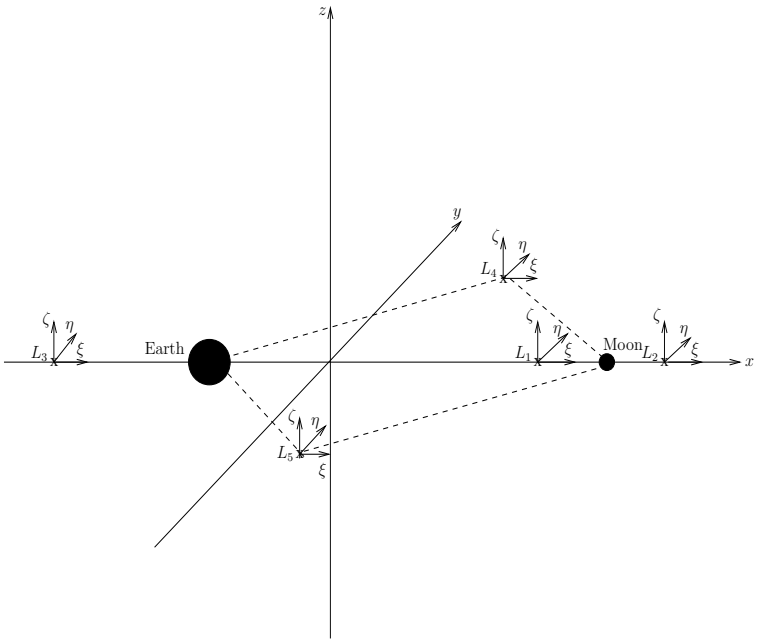

Figure 4.1: Attachment of the components of the position vector $\delta\boldsymbol{r} = (\xi, \eta, \zeta)^T$ to the Lagrange points in the Earth-Moon System.

where $\mathbf{X} = (\delta\boldsymbol{r}, \delta\dot{\boldsymbol{r}})^T$.

Then, for the linear system (4.4), the matrix A is given by

$$A = \begin{pmatrix} 0_3 & I_3 \\ K & \Omega \end{pmatrix}, \tag{4.5}$$

where 0_3 is a null matrix, I_3 is a identity matrix,

$$K = \left[\frac{\partial \nabla U(\boldsymbol{r})}{\partial \boldsymbol{r}} \bigg|_{\boldsymbol{r}=\boldsymbol{r}_L} \right], \tag{4.6}$$

and

$$\Omega = \begin{pmatrix} 0 & 2 & 0 \\ -2 & 0 & 0 \\ 0 & 0 & 0 \end{pmatrix}. \tag{4.7}$$

4.1.1 Collinear Libration Points

In component form equation (4.4) shows that the nondimensional linearised equations of motion near the collinear libration points are given by

$$\ddot{\xi} - 2\dot{\eta} - U^o_{xx}\xi = 0, \tag{4.8}$$
$$\ddot{\eta} + 2\dot{\xi} - U^o_{yy}\eta = 0, \tag{4.9}$$
$$\ddot{\zeta} - U^o_{zz}\zeta = 0, \tag{4.10}$$

where

$$\begin{aligned} U^o_{xx} &= 1 + 2c_2, \\ U^o_{yy} &= 1 - c_2, \\ U^o_{zz} &= -c_2, \end{aligned}$$

and

$$c_2 = \frac{1-\mu}{|x_{L_i} + \mu|^3} + \frac{\mu}{|x_{L_i} - (1-\mu)|^3}, \qquad i = 1, 2, 3.$$

The general form of the solution describing the in-plane motion is given by

$$\xi(t) = \sum_{k=1}^{4} A_k e^{\lambda_k t}, \tag{4.11}$$
$$\eta(t) = \sum_{k=1}^{4} B_k e^{\lambda_k t}, \tag{4.12}$$

where λ_k are the in-plane eigenvalues, A_k and B_k are constants to be determined from the initial conditions. The in-plane eigenvalues λ_k are the roots of the characteristic polynomial

$$\lambda^4 + \lambda^2(4 - U^o_{xx} - U^o_{yy}) + U^o_{xx}U^o_{yy} = 0. \tag{4.13}$$

Thus, the solutions are written in the following form

$$\lambda_{1,2} = \pm\sqrt{-\iota_1 + \sqrt{\iota_1^2 + \iota_2^2}}, \tag{4.14}$$
$$\lambda_{3,4} = \pm i\sqrt{\iota_1 + \sqrt{\iota_1^2 + \iota_2^2}} = \pm i\omega_{\xi\eta}, \tag{4.15}$$

where

$$\iota_1 = 2 - \frac{U^o_{xx} + U^o_{yy}}{2}, \tag{4.16}$$
$$\iota_2^2 = -U^o_{xx}U^o_{yy} > 0. \tag{4.17}$$

It can be seen that two of the four roots of the characteristic equation are always real and two roots are purely immaginary.

Substituting equations (4.11) and (4.12) into equation (6.61)-(6.62), it is found that

$$B_k = \frac{\lambda_k^2 - U_{xx}^o}{2\lambda_k} A_k. \tag{4.18}$$

By making use of the equation (4.18), the initial state variations are related to the coefficient A_k as follows

$$\xi(t_0) = \sum_{k=1}^{4} A_k e^{\lambda_k t_0}, \tag{4.19}$$

$$\dot{\xi}(t_0) = \sum_{k=1}^{4} \lambda_k A_k e^{\lambda_k t_0}, \tag{4.20}$$

$$\eta(t_0) = \sum_{k=1}^{4} \frac{\lambda_k^2 - U_{xx}^o}{2\lambda_k} A_k e^{\lambda_k t_0}, \tag{4.21}$$

$$\dot{\eta}(t_0) = \sum_{k=1}^{4} \lambda_k \frac{\lambda_k^2 - U_{xx}^o}{2\lambda_k} A_k e^{\lambda_k t_0}. \tag{4.22}$$

The ζ equation is uncoupled from the ξ and η equations and can be solved separately. The out-of-plane eigenvalues can be obtained from the characteristic polynomial

$$\lambda^2 - U_{zz}^o = 0, \tag{4.23}$$

that is

$$\lambda_{5,6} = \pm i\sqrt{|U_{zz}^o|} = \pm i\omega_\zeta. \tag{4.24}$$

The characteristic equation for the out-of-plane motion possesses purely imaginary roots. The solution of the out-of-plane motion may be written as

$$\zeta(t) = C_1 \cos(\omega_\zeta t) + C_2 \sin(\omega_\zeta t), \tag{4.25}$$

where $\omega_\zeta = \sqrt{|U_{zz}^o|}$ is the out-of-plane frequency and C_1 and C_2 are constants to be determined from the initial conditions. When $t = 0$, $\zeta(0) = \zeta_0$ and $\dot{\zeta}(0) = \dot{\zeta}_0$, and so $\zeta_0 = C_2$ and $\dot{\zeta}_0 = C_1\omega_\zeta$.

Consequently, the general solution can be obtained as

$$\zeta(t) = \zeta_0 \cos(\omega_\zeta t) + \frac{\dot{\zeta}_0}{\omega_\zeta} \sin(\omega_\zeta t). \tag{4.26}$$

Thus, the linearisation relative to the collinear libration points yields two pairs of eigenvalues corresponding to the centre manifold, and one pair of eigenvalues that represents

the saddle component leading to instability. However, the solution of the in-plane motion can be made to contain only oscillatory modes with the proper choice of intial conditions ($A_1 = A_2 = 0$). The constants A_1 and A_2 are associated with the real exponents defined in equation (4.14), which corresponds to the saddle component of the phase space. The resulting linear solution for the in-plane motion can then be written as

$$\xi(t) = A_3 e^{\lambda_3 t} + A_4 e^{\lambda_4 t}, \tag{4.27}$$
$$\eta(t) = B_3 e^{\lambda_3 t} + B_4 e^{\lambda_4 t}. \tag{4.28}$$

Specifically for an initial position ξ_0 and η_0, the coefficients A_3, A_4, B_3 and B_4 can be evaluated. Thus, the resulting linear solution becomes

$$\xi(t) = \xi_0 \cos(\omega_{\xi\eta} t) + \frac{\eta_0}{j} \sin(\omega_{\xi\eta} t), \tag{4.29}$$
$$\eta(t) = \eta_0 \cos(\omega_{\xi\eta} t) - j\xi_0 \sin(\omega_{\xi\eta} t). \tag{4.30}$$

where j and $\omega_{\xi\eta}$ are defined as

$$j = \frac{\omega_{\xi\eta}^2 + U_{xx}^o}{2\omega_{\xi\eta}}, \tag{4.31}$$
$$\omega_{\xi\eta} = \sqrt{\iota_1 + \sqrt{\iota_1^2 + \iota_2^2}}. \tag{4.32}$$

It can be further noted that the general solution of the linearised equations of motion ((4.8)-(4.10)) around the collinear points, as given in reference [153], can also be expressed as

$$\xi(t) = A_1 e^{\nu_{\xi\eta} t} + A_2 e^{-\nu_{\xi\eta} t} + A_3 \cos(\omega_{\xi\eta} t) + A_4 \sin(\omega_{\xi\eta} t), \tag{4.33}$$
$$\eta(t) = k_1 A_1 e^{\nu_{\xi\eta} t} - k_1 A_2 e^{-\nu_{\xi\eta} t} - k_2 A_4 \cos(\omega_{\xi\eta} t) + k_2 A_3 \sin(\omega_{\xi\eta} t), \tag{4.34}$$
$$\zeta(t) = C_1 \cos(\omega_\zeta t) + C_2 \sin(\omega_\zeta t), \tag{4.35}$$

for arbitrary constants of integration A_i and some constants k_1, k_2, $\omega_{\xi\eta}$, ω_ζ and $\nu_{\xi\eta}$ depending on the value of the mass parameter and the libration point where

$$\begin{aligned}
\omega_{\xi\eta} &= \sqrt{\frac{1}{2}\Big((2-c_2)+\sqrt{(2-c_2)^2-4(1-c_2)(1+2c_2)}\Big)}, \\
&= \sqrt{\frac{2-c_2+\sqrt{9c_2^2-8c_2}}{2}}, \qquad (4.36)\\
\nu_{\xi\eta} &= \sqrt{\frac{1}{2}\Big(-(2-c_2)+\sqrt{(2-c_2)^2-4(1-c_2)(1+2c_2)}\Big)}, \\
&= \sqrt{\frac{-2+c_2+\sqrt{9c_2^2-8c_2}}{2}}, \qquad (4.37)\\
\omega_\zeta &= \sqrt{c_2}, \qquad (4.38)\\
k_1 &= \frac{-1-2c_2+\nu_{\xi\eta}^2}{2\nu_{\xi\eta}}, \qquad (4.39)\\
k_2 &= -\frac{1+2c_2+\omega_{\xi\eta}^2}{2\omega_{\xi\eta}}. \qquad (4.40)
\end{aligned}$$

The out-of-plane motion consists of an harmonic oscillator

$$\begin{bmatrix} \zeta \\ \dot{\zeta} \end{bmatrix} = \begin{bmatrix} \cos\nu_{\xi\eta}t & \sin\nu_{\xi\eta}t \\ -\nu_{\xi\eta}\sin\nu_{\xi\eta}t & \nu_{\xi\eta}\cos\nu_{\xi\eta}t \end{bmatrix} \begin{bmatrix} C_1 \\ C_2 \end{bmatrix}, \qquad (4.41)$$

and the inverse can be expressed as follows

$$\begin{bmatrix} C_1 \\ C_2 \end{bmatrix} = \begin{bmatrix} \cos\nu_{\xi\eta}t & \frac{-1}{\nu_{\xi\eta}}\sin\nu_{\xi\eta}t \\ -\sin\nu_{\xi\eta}t & \frac{1}{\nu_{\xi\eta}}\cos\nu_{\xi\eta}t \end{bmatrix} \begin{bmatrix} \zeta \\ \dot{\zeta} \end{bmatrix}. \qquad (4.42)$$

The in-plane motion is given by the following linear transformation

$$\begin{bmatrix} \xi \\ \eta \\ \dot{\xi} \\ \dot{\eta} \end{bmatrix} = \begin{bmatrix} e^{\nu_{\xi\eta}t} & e^{-\nu_{\xi\eta}t} & \cos\omega_{\xi\eta}t & \sin\omega_{\xi\eta} \\ k_1e^{\nu_{\xi\eta}t} & -k_1e^{-\nu_{\xi\eta}t} & k_2\sin\omega_{\xi\eta}t & -k_2\cos\omega_{\xi\eta} \\ \nu_{\xi\eta}e^{\nu_{\xi\eta}t} & -\nu_{\xi\eta}e^{-\nu_{\xi\eta}t} & -\omega_{\xi\eta}\sin\omega_{\xi\eta}t & \omega_{\xi\eta}\cos\omega_{\xi\eta} \\ k_1\nu_{\xi\eta}e^{\nu_{\xi\eta}t} & k_1\nu_{\xi\eta}e^{-\nu_{\xi\eta}t} & k_2\omega_{\xi\eta}\cos\omega_{\xi\eta}t & k_2\omega_{\xi\eta}\sin\omega_{\xi\eta} \end{bmatrix} \begin{bmatrix} A_1 \\ A_2 \\ A_3 \\ A_4 \end{bmatrix}, \qquad (4.43)$$

and

$$\begin{bmatrix} A_1 \\ A_2 \\ A_3 \\ A_4 \end{bmatrix} = \begin{bmatrix} -\frac{k_2\omega_{\xi\eta}}{2\kappa_1}e^{-\nu_{\xi\eta}t} & \frac{\omega_{\xi\eta}}{2\kappa_2}e^{-\nu_{\xi\eta}t} & \frac{k_2}{2\kappa_2}e^{-\nu_{\xi\eta}t} & \frac{1}{2\kappa_1}e^{-\nu_{\xi\eta}t} \\ -\frac{k_2\omega_{\xi\eta}}{2\kappa_1}e^{\nu_{\xi\eta}t} & -\frac{\omega_{\xi\eta}}{2\kappa_2}e^{\nu_{\xi\eta}t} & -\frac{k_2}{2\kappa_2}e^{\nu_{\xi\eta}t} & \frac{1}{2\kappa_1}e^{\nu_{\xi\eta}t} \\ \frac{k_1\nu_{\xi\eta}}{\kappa_1}\cos(\omega_{\xi\eta}t) & \frac{\nu_{\xi\eta}}{\kappa_2}\sin(\omega_{\xi\eta}t) & -\frac{k_1}{\kappa_2}\sin(\omega_{\xi\eta}t) & -\frac{1}{\kappa_1}\cos(\omega_{\xi\eta}t) \\ \frac{k_1\nu_{\xi\eta}}{\kappa_1}\sin(\omega_{\xi\eta}t) & -\frac{\nu_{\xi\eta}}{\kappa_2}\cos(\omega_{\xi\eta}t) & \frac{k_1}{\kappa_2}\cos(\omega_{\xi\eta}t) & -\frac{1}{\kappa_1}\sin(\omega_{\xi\eta}t) \end{bmatrix} \begin{bmatrix} \xi \\ \eta \\ \dot{\xi} \\ \dot{\eta} \end{bmatrix} \qquad (4.44)$$

with $\kappa_1 = k_1\nu_{\xi\eta} - k_2\omega_{\xi\eta}$, $\kappa_2 = k_1\omega_{\xi\eta} + k_2\nu_{\xi\eta}$.

If, however, initial conditions are specified such that $A_1 = A_2 = 0$, then the general form of the solution for motion near the collinear libration points is a Lissajous path. The subsequent motion can then be approximated from equations ((4.33)-(4.35)) and the linearised results are given by

$$\begin{aligned} \xi(t) &= A_3\cos(\omega_{\xi\eta}t) + A_4\sin(\omega_{\xi\eta}t), && (4.45)\\ \eta(t) &= -k_2A_4\cos(\omega_{\xi\eta}t) + k_2A_3\sin(\omega_{\xi\eta}t), && (4.46)\\ \zeta(t) &= C_1\cos(\omega_\zeta t) + C_2\sin(\omega_\zeta t). && (4.47) \end{aligned}$$

With this restriction, the initial conditions that are required to produce bounded motion are given by

$$\begin{aligned} \xi(0) &= A_3, && (4.48)\\ \eta(0) &= -k_2A_4, && (4.49)\\ \dot{\xi}(0) &= \omega_{\xi\eta}A_4, && (4.50)\\ \dot{\eta}(0) &= \omega_{\xi\eta}k_2A_3. && (4.51) \end{aligned}$$

The equations can then be rearranged and expressed in a more convenient form as

$$\begin{aligned} \xi(t) &= A_\xi\cos(\omega_{\xi\eta}t + \phi), && (4.52)\\ \eta(t) &= k_2A_\xi\sin(\omega_{\xi\eta}t + \phi), && (4.53)\\ \zeta(t) &= A_\zeta\cos(\omega_\zeta t + \psi), && (4.54) \end{aligned}$$

where $\omega_{\xi\eta}$ and ω_ζ are the linearized frequencies and k_2 is a constant. The parameters A_ξ and A_ζ are the amplitudes of the in-plane and out-of-plane motion, and ϕ, ψ are the phase angles that are determined by the initial conditions. Analogous solutions will be found in Chapter 5 for the solar sail problem. A sample Lissajous orbit in the vicinity of the L_1 libration point can be seen in Figure 4.2.

4.1.2 Triangular Libration Points

Again, in component form equation (4.4) shows that the linearised equations of motions about the triangular points can be written as

$$\begin{aligned} \ddot{\xi} - 2\dot{\eta} &= U^o_{xx}\xi + U^o_{xy}\eta, && (4.55)\\ \ddot{\eta} + 2\dot{\xi} &= U^o_{xy}\xi + U^o_{yy}\eta, && (4.56)\\ \ddot{\zeta} &= U^o_{zz}\zeta, && (4.57) \end{aligned}$$

Thus, the values of the the partial derivatives of the gravitational potential are given by

$$\begin{aligned} U^o_{xx}|_{L_{4,5}} &= \frac{3}{4}, && (4.58)\\ U^o_{yy}|_{L_{4,5}} &= \frac{9}{4}, && (4.59)\\ U^o_{xy}|_{L_4} &= \frac{3\sqrt{3}}{2}\left(\mu - \frac{1}{2}\right) && (4.60)\\ U^o_{xy}|_{L_5} &= -\frac{3\sqrt{3}}{2}\left(\mu - \frac{1}{2}\right) && (4.61)\\ U^o_{zz}|_{L_{4,5}} &= -1. && (4.62) \end{aligned}$$

The in-plane equations lead to the characteristic equation

$$\begin{aligned} \begin{vmatrix} \lambda^2 - \frac{3}{4} & -2\lambda - \frac{3\sqrt{3}}{2}\left(\frac{1}{2} - \mu\right) \\ 2\lambda - \frac{3\sqrt{3}}{2}\left(\frac{1}{2} - \mu\right) & \lambda^2 - \frac{9}{4} \end{vmatrix} &= 0, && (4.63)\\ \lambda^4 + \lambda^2 + \frac{27}{4}\mu(1-\mu) &= 0, && (4.64) \end{aligned}$$

which results in the eigenvalues

$$\lambda_{1,2} = \pm\sqrt{\frac{-1 + \sqrt{1 - 27\mu + 27\mu^2}}{2}} = \pm i\omega_{\xi\eta_1}, \quad (4.65)$$

$$\lambda_{3,4} = \pm\sqrt{\frac{-1 - \sqrt{1 - 27\mu + 27\mu^2}}{2}} = \pm i\omega_{\xi\eta_2}. \quad (4.66)$$

For the Earth-Moon mass ratio μ, the four eigenvalues λ_i are found to be

$$\begin{aligned} \lambda_{1,2} &= \pm i 0.298207, \\ \lambda_{3,4} &= \pm i 0.954500. \end{aligned}$$

Hence, the stability of the triangular points changes when the discriminant

$$D = 1 - 27\mu^{\pm}_c(1 - \mu^{\pm}_c) = 0. \quad (4.67)$$

The roots of the equation (4.67) are

$$\begin{aligned} \mu^-_c &= \frac{1}{2}\left(1 - \frac{\sqrt{69}}{9}\right), \\ &\approx 0.03852, \end{aligned}$$

and $\mu_c^+ = 1 - \mu_c^- \approx 0.96148$.

The triangular libration points are then stable when the mass parameter is smaller than the critical value μ_c^- $(0 \leq \mu < \mu_c^-)$. This includes the Earth-Moon CRTBP problem, since the mass parameter is less than the critical value.

The general form of the solution for the in-plane motion may be written as

$$\xi(t) = D_1 \cos(\omega_{\xi\eta_1} t) + D_2 \sin(\omega_{\xi\eta_1} t) + D_3 \sin(\omega_{\xi\eta_2} t) + D_4 \sin(\omega_{\xi\eta_2} t), \quad (4.68)$$

$$\eta(t) = E_1 \cos(\omega_{\xi\eta_1} t) + E_2 \sin(\omega_{\xi\eta_1} t) + E_3 \cos(\omega_{\xi\eta_2} t) + E_4 \sin(\omega_{\xi\eta_2} t), \quad (4.69)$$

where D_k and E_k are coefficients to be determined from the initial conditions.

The linear long period is then associated to the frequencies $\lambda_{1,2}$, while the short period is associated to $\lambda_{3,4}$.

However, relationships between D_k and E_k can be derived as follows

$$E_1 = \Gamma_1 \Big(2\omega_{\xi\eta_1} D_2 - D_1 U_{xy}^o \Big), \quad (4.70)$$

$$E_2 = -\Gamma_1 \Big(2\omega_{\xi\eta_1} D_1 + D_2 U_{xy}^o \Big), \quad (4.71)$$

$$E_3 = \Gamma_2 \Big(2\omega_{\xi\eta_2} D_4 - D_3 U_{xy}^o \Big), \quad (4.72)$$

$$E_4 = -\Gamma_2 \Big(2\omega_{\xi\eta_2} D_3 + D_4 U_{xy}^o \Big), \quad (4.73)$$

where

$$\Gamma_1 = \frac{\omega_{\xi\eta_1}^2 + U_{xx}^o}{4\omega_{\xi\eta_1}^2 + (U_{xy}^o)^2},$$

$$\Gamma_2 = \frac{\omega_{\xi\eta_2}^2 + U_{xx}^o}{4\omega_{\xi\eta_2}^2 + (U_{xy}^o)^2}.$$

The short period is approximately the same as the period of the lunar orbit, and the long period is almost three revolutions of the primaries (about three months).

So, either the short- or the long-period terms can be eliminated from the general solution by properly selected initial conditions to render the the complete solution periodic.

This can be achieved by setting the values of the long period coefficients equal to zero $D_1 = D_2 = 0$, so $E_1 = E_2 = 0$ and the initial velocities are given by

$$\dot{\xi}_0 = \frac{1}{2} \left(\xi_0 U_{xy}^o + \frac{\eta_0}{\Gamma_2} \right), \quad (4.74)$$

$$\dot{\eta}_0 = -\frac{1}{2} \left[\xi_0 \left(\omega_{\xi\eta_2}^2 + U_{xx}^o \right) + \eta_0 U_{xy}^o \right]. \quad (4.75)$$

The linearised short-period solution becomes

$$\xi(t) = \xi_0 \cos(\omega_{\xi\eta_2} t) + \frac{\dot{\xi}_0}{\omega_{\xi\eta_2}} \sin(\omega_{\xi\eta_2} t), \tag{4.76}$$

$$\eta(t) = \eta_0 \cos(\omega_{\xi\eta_2} t) + \frac{\dot{\eta}_0}{\omega_{\xi\eta_2}} \sin(\omega_{\xi\eta_2} t). \tag{4.77}$$

Similary, the short-period terms will not occur in the solution if $D_3 = D_4 = 0$, and then $E_3 = E_4 = 0$. Therefore, the initial velocities can be expressed as

$$\dot{\xi}_0 = \frac{1}{2}\left(\xi_0 U^o_{xy} + \frac{\eta_0}{\Gamma_1}\right), \tag{4.78}$$

$$\dot{\eta}_0 = -\frac{1}{2}\left[\xi_0\left(\omega^2_{\xi\eta_1} + U^o_{xx}\right) + \eta_0 U^o_{xy}\right]. \tag{4.79}$$

The linear analytical long-period solution is as follows

$$\xi(t) = \xi_0 \cos(\omega_{\xi\eta_1} t) + \frac{\dot{\xi}_0}{\omega_{\xi\eta_1}} \sin(\omega_{\xi\eta_1} t), \tag{4.80}$$

$$\eta(t) = \eta_0 \cos(\omega_{\xi\eta_1} t) + \frac{\dot{\eta}_0}{\omega_{\xi\eta_1}} \sin(\omega_{\xi\eta_1} t). \tag{4.81}$$

Thus, the orbit after elimination of either the short- or the long-period coefficients becomes an ellipse. Analogous solutions will again be found in Chapter 5 for the solar sail problem.

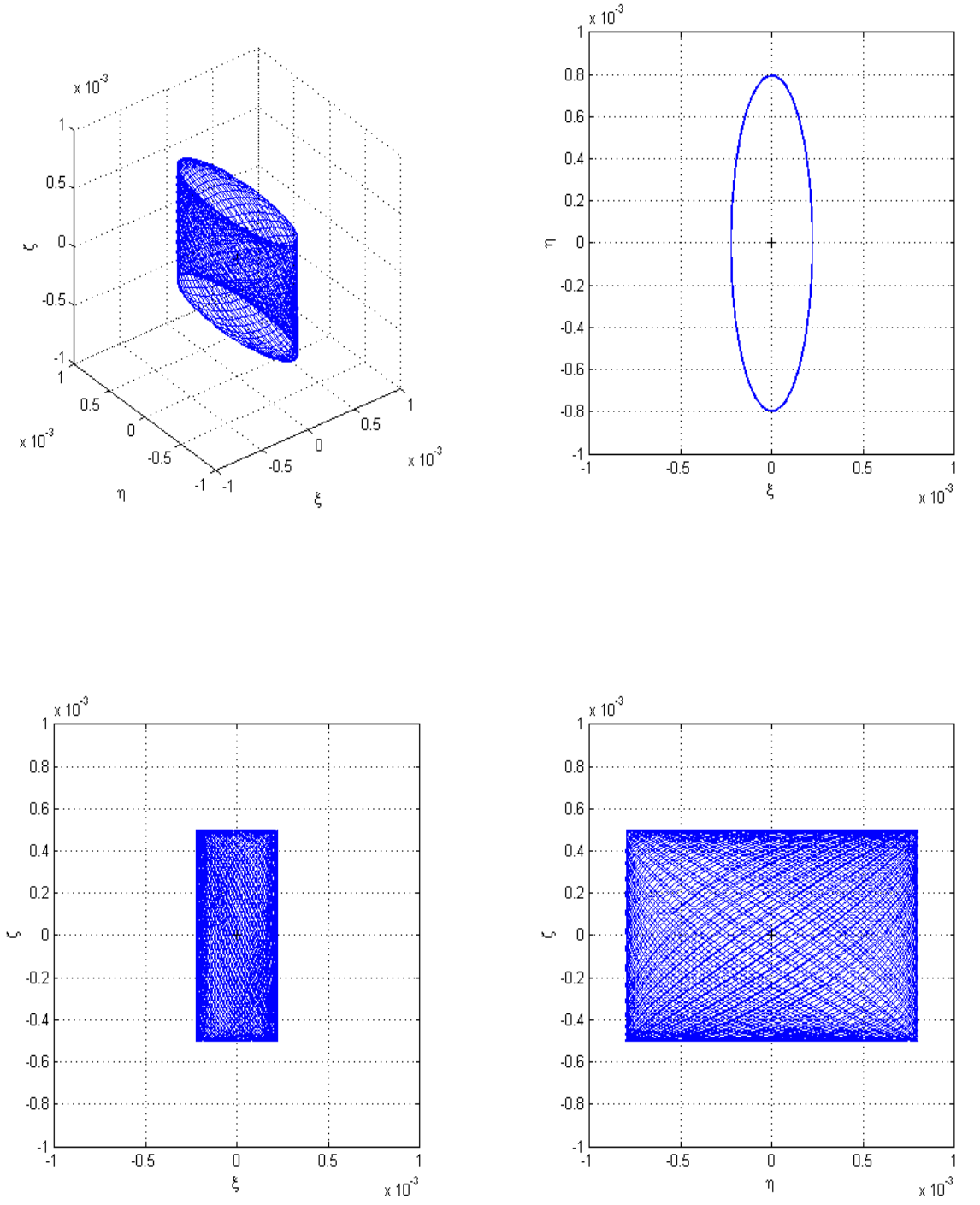

Figure 4.2: Lissajous trajectory near L_1 in the Earth-Moon system. From left to right, top to bottom: $\xi\eta$, $\xi\zeta$ and $\eta\zeta$ projections.

4.2 Summary

The objective of this Chapter was to produce continuous bounded Lissajous solutions analytically from the linear equations of motion. An approximate analytical solution for Lissajous orbits is presented. The examples shown here were computed for the L_1 libration point, as seen in Figure 4.2. However, the approach is quite general and can be applied to other libration points. The linear analytical solution provides valuable information for numerical study, which will be used in Chapter 5 for the solar sail three-body system.

Chapter 5

Solar Sail Trajectories Relative to the Libration Points in the Earth-Moon System

This Chapter investigates displaced periodic orbits at linear order in the circular restricted Earth-Moon system, where the third massless body is a solar sail. These orbits are achieved using an extremely small sail acceleration. A sufficient condition for displaced periodic orbits based on the sail pitch angle and the magnitude of the solar radiation pressure for fixed initial out-of-plane distance has been derived. The solar sail Earth-Moon system differs greatly from the Earth-Sun system as the Sun-line direction varies continuously in the rotating frame and the equations of motion of the sail are given by a set of nonlinear, non-autonomous ordinary differential equations. By introducing a first-order approximation, periodic orbits are derived analytically at linear order. Then, solar sail propulsion is used to provide station-keeping at periodic orbits around the triangular libration points using small variations in the sail's orientation. A control methodology for maintaining the sail in the z-direction is defined. Thus, a linear feedback controller is proposed by linearising the z-dynamics about the triangular libration points. A simulation using this controller is then performed using constant gains. Since the in-plane motion is naturally stable, the out-of-plane motion is controlled through a simple manipulation of the sail pitch angle.

5.1 System Model

Again m_1 represents the larger primary (Earth), m_2 the smaller primary (Moon) and the motion of the sail which has a negligible mass will be considered. It is always assumed that the two more massive bodies are moving in circular orbits with constant angular velocity ω about their common center of mass, and the mass of the third body is too small to affect the motion of the two more massive bodies. The unit mass is taken to be the total mass of the system $(m_1 + m_2)$ and the unit of length is chosen to be the constant separation $R^\star$ between m_1 and m_2. The time unit is defined such that m_2 orbits around m_1 in time 2π.

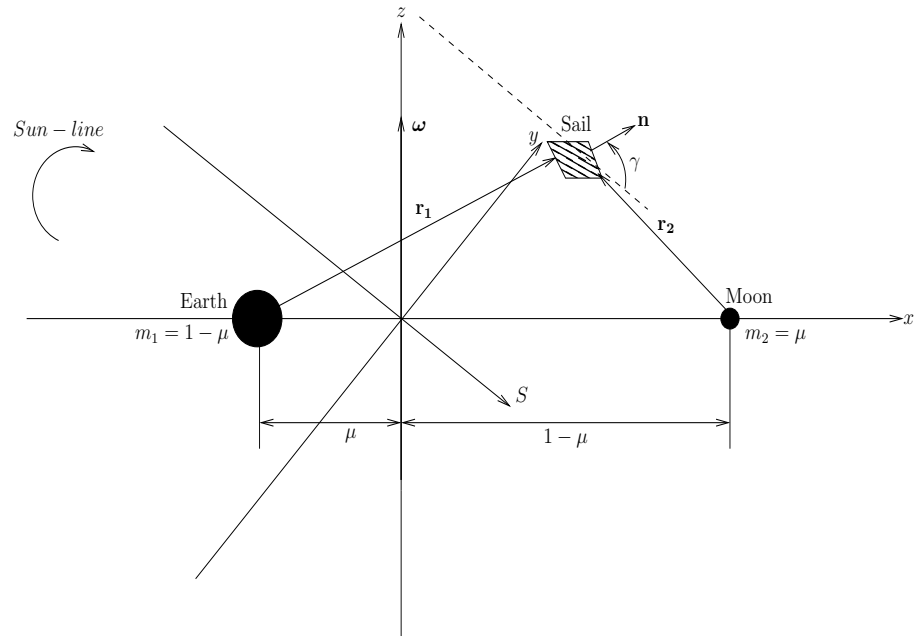

Figure 5.1: Schematic geometry of the Earth-Moon restricted three-body problem.

Under these considerations the masses of the primaries in the normalized system of units are $m_1 = 1 - \mu$ and $m_2 = \mu$, with $\mu = m_2/(m_1 + m_2)$ (see Figure 5.1). The dashed line in Figure 5.1 is a line parallel to the Sun-line direction $\boldsymbol{S}$.

5.1.1 Equations of Motion in Presence of a Solar Sail

The nondimensional equation of a motion of a solar sail in the rotating frame of reference is described by

$$\frac{d^2\boldsymbol{r}}{dt^2} + 2\boldsymbol{\omega} \times \frac{d\boldsymbol{r}}{dt} + \nabla U(\boldsymbol{r}) = \boldsymbol{a}_S, \tag{5.1}$$

where $\boldsymbol{\omega} = \omega\hat{\boldsymbol{z}}$ ($\hat{\boldsymbol{z}}$ is a unit vector pointing in the direction $\boldsymbol{z}$) is the angular velocity vector of the rotating frame and $\boldsymbol{r}$ is the position vector of the sail relative to the center of mass of the two primaries. The small annual changes in the inclination of the Sun-line with respect to the plane of the system will not be considered. By introducing the three-body gravitational potential $V(\boldsymbol{r})$ due to the primaries, and the scalar potential $\Phi(\boldsymbol{r})$ to represent the conservative centripetal acceleration, the new modified potential function (pseudo-potential function) is defined by

$$U(\boldsymbol{r}) = V(\boldsymbol{r}) + \Phi(\boldsymbol{r}), \tag{5.2}$$

where

$$V(\boldsymbol{r}) = -\left[\frac{1-\mu}{r_1} + \frac{\mu}{r_2}\right], \tag{5.3}$$

$$\Phi(\boldsymbol{r}) = -\frac{1}{2}(x^2+y^2), \tag{5.4}$$

with

$$\nabla V(\boldsymbol{r}) = \frac{1-\mu}{r_1^3}\boldsymbol{r}_1 + \frac{\mu}{r_2^3}\boldsymbol{r}_2, \tag{5.5}$$

$$\nabla \Phi(\boldsymbol{r}) = \boldsymbol{\omega} \times (\boldsymbol{\omega} \times \boldsymbol{r}). \tag{5.6}$$

The three-body pseudo-potential $U(\boldsymbol{r})$ and the solar radiation pressure acceleration $\boldsymbol{a}_S$ are defined by

$$U(\boldsymbol{r}) = -\left[\frac{1}{2}|\boldsymbol{\omega} \times \boldsymbol{r}|^2 + \frac{1-\mu}{r_1} + \frac{\mu}{r_2}\right], \tag{5.7}$$

$$\boldsymbol{a}_S = a_0(\boldsymbol{S}\cdot\boldsymbol{n})^2\boldsymbol{n}, \tag{5.8}$$

where μ is the mass ratio for the Earth-Moon system. The sail position vectors w.r.t. m_1 and m_2 respectively (see Figure 5.1) are $\boldsymbol{r}_1 = [x+\mu, y, z\,]^T$ and $\boldsymbol{r}_2 = [x-(1-\mu), y, z]^T$, a_0 is the magnitude of the solar radition pressure acceleration exerted on the sail, as discussed in Chapter 2, and the unit vector $\boldsymbol{n}$ denotes the thrust direction. The sail is oriented such that it is always directed along the Sun-line $\boldsymbol{S}$, pitched at an angle γ to provide a constant out-of-plane force. The unit normal to the sail surface $\boldsymbol{n}$ and the Sun-line direction $\boldsymbol{S}$ are given by

$$\boldsymbol{n} = \left[\begin{array}{ccc} \cos(\gamma)\cos(\omega_\star t) & -\cos(\gamma)\sin(\omega_\star t) & \sin(\gamma) \end{array}\right]^T, \tag{5.9}$$

$$\boldsymbol{S} = \left[\begin{array}{ccc} \cos(\omega_\star t) & -\sin(\omega_\star t) & 0 \end{array}\right]^T, \tag{5.10}$$

where $\omega_\star = 0.923$ is the angular rate of the Sun-line in the corotating frame in a dimensionless synodic coordinate system. The sail normal is chosen to follow the Sun-line and maintain a fixed pitch angle γ, as shown in Figure 5.1.

5.1.2 Linearised System

The dynamics of the sail in the neighborhood of the libration points will now be investigated. The coordinates of the equilibrium point are defined as $\boldsymbol{r}_L = (x_{L_i}, y_{L_i}, z_{L_i})^T$ with $i = 1, \cdots, 5$. Let a small displacement in $\boldsymbol{r}_L$ be $\delta\boldsymbol{r}$ such that $\boldsymbol{r} \to \boldsymbol{r}_L + \delta\boldsymbol{r}$. The equation of motion for the solar sail in the neighborhood of $\boldsymbol{r}_L$ is therefore

$$\frac{d^2\delta\boldsymbol{r}}{dt^2} + 2\boldsymbol{\omega} \times \frac{d\delta\boldsymbol{r}}{dt} + \nabla U(\boldsymbol{r}_L + \delta\boldsymbol{r}) = \boldsymbol{a}_S(\boldsymbol{r}_L + \delta\boldsymbol{r}). \tag{5.11}$$

Then, retaining only the first-order term in $\delta\boldsymbol{r} = (\xi, \eta, \zeta)^T$ in a Taylor-series expansion, where (ξ, η, ζ) are attached to the Lagrange points as shown in Figure 4.1, the gradient of the potential and the acceleration can be expressed as

$$\nabla U(\boldsymbol{r}_L + \delta\boldsymbol{r}) = \nabla U(\boldsymbol{r}_L) + \left.\frac{\partial \nabla U(\boldsymbol{r})}{\partial \boldsymbol{r}}\right|_{r=r_L} \delta\boldsymbol{r} + O(\delta\boldsymbol{r}^2), \tag{5.12}$$

$$\boldsymbol{a}_S(\boldsymbol{r}_L + \delta\boldsymbol{r}) = \boldsymbol{a}_S(\boldsymbol{r}_L) + \left.\frac{\partial \boldsymbol{a}_S(\boldsymbol{r})}{\partial \boldsymbol{r}}\right|_{r=r_L} \delta\boldsymbol{r} + O(\delta\boldsymbol{r}^2). \tag{5.13}$$

It is assumed that $\nabla U(\boldsymbol{r}_L) = 0$, and the acceleration is constant with respect to the small displacement $\delta\boldsymbol{r}$, so that

$$\left.\frac{\partial \boldsymbol{a}_S(\boldsymbol{r})}{\partial \boldsymbol{r}}\right|_{r=r_L} = 0. \tag{5.14}$$

The linear variational system associated with the libration points at $\boldsymbol{r}_L$ can be determined by substituting equations (5.12) and (5.13) into (5.11)

$$\frac{d^2\delta\boldsymbol{r}}{dt^2} + 2\boldsymbol{\omega} \times \frac{d\delta\boldsymbol{r}}{dt} + K\delta\boldsymbol{r} = 0, \tag{5.15}$$

where the matrix K is defined as

$$K = -\left[\left.\frac{\partial \nabla U(\boldsymbol{r})}{\partial \boldsymbol{r}}\right|_{r=r_L}\right]. \tag{5.16}$$

Using matrix notation the linearised equation of motion about the libration point (Equation (5.15)) can be represented by the inhomogeneous linear system $\dot{\mathbf{X}} = A\mathbf{X} + \boldsymbol{b}(t)$, where the state vector $\mathbf{X} = (\delta\boldsymbol{r}, \delta\dot{\boldsymbol{r}})^T$, and $\boldsymbol{b}(t)$ is a 6×1 vector, which represents the solar sail acceleration.

The Jacobian matrix A has the general form

$$A = \begin{pmatrix} 0_3 & I_3 \\ K & \Omega \end{pmatrix}, \tag{5.17}$$

where I_3 is a identity matrix, and

$$\Omega = \begin{pmatrix} 0 & 2 & 0 \\ -2 & 0 & 0 \\ 0 & 0 & 0 \end{pmatrix}. \tag{5.18}$$

For convenience the sail attitude is fixed such that the sail normal vector $\boldsymbol{n}$, points always along the direction of the Sun-line with the following constraint $\boldsymbol{S} \cdot \boldsymbol{n} \geq 0$. Its direction is described by the pitch angle γ relative to the Sun-line, which represents the sail attitude.

Collinear libration points

By making the transformation $\boldsymbol{r} \rightarrow \boldsymbol{r}_L + \delta\boldsymbol{r}$ and retaining only the first-order term in $\delta\boldsymbol{r} = (\xi, \eta, \zeta)^T$ in a Taylor-series expansion, the linearised nondimensional equations of motion relative to the collinear libration points can be written as

$$\ddot{\xi} - 2\dot{\eta} - U^o_{xx}\xi = a_\xi, \tag{5.19}$$
$$\ddot{\eta} + 2\dot{\xi} - U^o_{yy}\eta = a_\eta, \tag{5.20}$$
$$\ddot{\zeta} - U^o_{zz}\zeta = a_\zeta, \tag{5.21}$$

where U^o_{xx}, U^o_{yy}, and U^o_{zz} are the partial derivatives of the gravitational potential evaluated at the collinear libration points as defined in Section 4.1.1, and the solar sail acceleration is defined in terms of three auxiliary variables a_ξ, a_η, and a_ζ.

From equation (5.8), the acceleration components are given by

$$\begin{aligned} a_\xi &= a_0 \cos(\omega_\star t)\cos^3(\gamma), \\ a_\eta &= -a_0 \sin(\omega_\star t)\cos^3(\gamma), \\ a_\zeta &= a_0 \cos^2(\gamma)\sin(\gamma). \end{aligned}$$

Equilateral libration points

In a similar fashion, recalling the linearised equations of motion obtained in the equation (5.15) describing the behavior of the system in the vicinity of the Lagrange points, it can be shown that the linear variational equations of motion in component form at the triangular points then become

$$\ddot{\xi} - 2\dot{\eta} - U^o_{xx}\xi - U^o_{xy}\eta = a_\xi, \tag{5.22}$$
$$\ddot{\eta} + 2\dot{\xi} - U^o_{xy}\xi - U^o_{yy}\eta = a_\eta, \tag{5.23}$$
$$\ddot{\zeta} - U^o_{zz}\zeta = a_\zeta, \tag{5.24}$$

where U^o_{xx}, U^o_{xy}, U^o_{yy}, and U^o_{zz} are again the partial derivatives of the gravitational potential evaluated at the triangular libration points as defined in Section 4.1.2.

5.2 Solution of the linearised equations of motion for the three-body model

Collinear libration points

Considering the dynamics of motion near the collinear libration points, a particular periodic solution in the plane as provided by Farquhar [152] can be chosen as

$$\xi(t) = \xi_0 \cos(\omega_\star t), \tag{5.25}$$
$$\eta(t) = \eta_0 \sin(\omega_\star t). \tag{5.26}$$

By inserting equations (5.25) and (5.26) in the differential equations ((5.19)-(5.20)), the linear system in ξ_0 and η_0 is obtained as

$$\begin{cases} \Big(U^o_{xx} - \omega^2_\star\Big)\xi_0 - 2\omega_\star\eta_0 = a_0\cos^3(\gamma), \\ -2\omega_\star\xi_0 + \Big(U^o_{yy} - \omega^2_\star\Big)\eta_0 = -a_0\cos^3(\gamma). \end{cases} \tag{5.27}$$

Then the amplitudes ξ_0 and η_0 are given by

$$\xi_0 = a_0\frac{\Big(U^o_{yy} - \omega^2_\star - 2\omega_\star\Big)\cos^3(\gamma)}{\Big(U^o_{xx} - \omega^2_\star\Big)\Big(U^o_{yy} - \omega^2_\star\Big) - 4\omega^2_\star}, \tag{5.28}$$

$$\eta_0 = a_0\frac{\Big(-U^o_{xx} + \omega^2_\star + 2\omega_\star\Big)\cos^3(\gamma)}{\Big(U^o_{xx} - \omega^2_\star\Big)\Big(U^o_{yy} - \omega^2_\star\Big) - 4\omega^2_\star}, \tag{5.29}$$

and so

$$\frac{\xi_0}{\eta_0} = \frac{\omega^2_\star + 2\omega_\star - U^o_{yy}}{-\omega^2_\star - 2\omega_\star + U^o_{xx}}. \tag{5.30}$$

Then the trajectory will be an ellipse centered on the collinear libration points. The required radiation pressure acceleration can be found by solving the equation (5.28)

$$a_0 = \cos^{-3}(\gamma)\left[\frac{\omega^4_\star - \omega^2_\star(U^o_{xx} + U^o_{yy} + 4) + U^o_{xx}U^o_{yy}}{U^o_{yy} - 2\omega_\star - \omega^2_\star}\right]\xi_0. \tag{5.31}$$

By applying the Laplace transform, the uncoupled out-of-plane ζ-motion defined by the equation (5.21) can be solved. The transform version is obtained as

$$s^2Z(s) - s\xi_0 - \dot{\xi}_0 - U^o_{zz}Z(s) = \frac{a_0\cos^2(\gamma)\sin(\gamma)}{s}, \tag{5.32}$$

$$(s^2 - U^o_{zz})Z(s) = \dot{\xi}_0 + s\xi_0 + \frac{a_0\cos^2(\gamma)\sin(\gamma)}{s}, \tag{5.33}$$

so that

$$Z(s) = \frac{1}{s^2 - U^o_{zz}}\left(\dot{\xi}_0 + s\xi_0 + \frac{a_0\cos^2(\gamma)\sin(\gamma)}{s}\right). \tag{5.34}$$

The frequency of the out-of-plane motion is given by solving the equation

$$s^2 - U^o_{zz} = 0,$$

where $s_{1,2} = \pm i\sqrt{|U^o_{zz}|} = \pm i\omega_\zeta$, as discussed in Section 4.1.1.

The inverse Laplace transform can be found, which will be the general solution of the out-of-plane component

$$\begin{aligned}\zeta(t) &= \zeta_0 \cos(\omega_\zeta t) + \dot{\zeta}_0 |U^o_{zz}|^{-1/2} \sin(\omega_\zeta t) \\ &\quad + a_0 \cos^2(\gamma) \sin(\gamma) |U^o_{zz}|^{-1} [U(t) - \cos(\omega_\zeta t)], \\ &= U(t) a_0 \cos^2(\gamma) \sin(\gamma) |U^o_{zz}|^{-1} + \dot{\zeta}_0 |U^o_{zz}|^{-1/2} \sin(\omega_\zeta t) \\ &\quad + \cos(\omega_\zeta t)[\zeta_0 - a_0 \cos^2(\gamma) \sin(\gamma) |U^o_{zz}|^{-1}],\end{aligned} \tag{5.35}$$

where the nondimensional frequency is defined as

$$\omega_\zeta = |U^o_{zz}|^{1/2}$$

and $U(t)$ is the unit step function.

Specifically for the choice of the initial data $\dot{\zeta}_0 = 0$, equation (5.35) can be more conveniently expressed as

$$\begin{aligned}\zeta(t) &= U(t) a_0 \cos^2(\gamma) \sin(\gamma) |U^o_{zz}|^{-1} \\ &\quad + \cos(\omega_\zeta t)[\zeta_0 - a_0 \cos^2(\gamma) \sin(\gamma) |U^o_{zz}|^{-1}].\end{aligned} \tag{5.36}$$

The solution can then be made to contain only a constant displacement at an out-of-plane distance

$$\zeta_0 = a_0 \cos^2(\gamma) \sin(\gamma) |U^o_{zz}|^{-1}. \tag{5.37}$$

Furthermore, the out-of-plane distance can be maximised by an optimal choice of the sail pitch angle determined by

$$\begin{aligned}\frac{d}{d\gamma} \cos^2(\gamma) \sin(\gamma) \Big|_{\gamma=\gamma^\star} &= 0, \\ \gamma^\star &= \tan^{-1}(2^{-1/2}), \\ \gamma^\star &= 35.264^\circ.\end{aligned} \tag{5.38}$$

Equilateral libration points

Following the idea already presented for the collinear points, since the particular solution in the plane defined by equations (5.25) and (5.26) cannot satisfy the linear ODEs for the triangular points, the subsequent discussion is to find the solutions that satisfy the differential equations ((5.22)-(5.23)).

Assume that a solution to the linearised equations of motion ((5.22)-(5.23)) is periodic of the form

$$\xi(t) = A_\xi \cos(\omega_\star t) + B_\xi \sin(\omega_\star t), \tag{5.39}$$
$$\eta(t) = A_\eta \cos(\omega_\star t) + B_\eta \sin(\omega_\star t), \tag{5.40}$$

where A_ξ, A_η, B_ξ and B_η are free parameters to be determined.

By substituting Equations (5.39) and (5.40) in the differential equations, a linear system in A_ξ, A_η, B_ξ and B_η is obtained as

$$\begin{cases} -(\omega_\star^2 + U^o_{xx})B_\xi + 2\omega_\star A_\eta - U^o_{xy}B_\eta = 0, \\ -U^o_{xy}A_\xi + 2\omega_\star B_\xi - (\omega_\star^2 + U^o_{xx})A_\eta = 0, \\ -(\omega_\star^2 + U^o_{xx})A_\xi - U^o_{xy}A_\eta - 2\omega_\star B_\eta = a_0\cos(\gamma)^3, \\ -2\omega_\star A_\xi - U^o_{xy}B_\xi - (\omega_\star^2 + U^o_{yy})B_\eta = -a_0\cos(\gamma)^3. \end{cases} \tag{5.41}$$

Thus, the linear system may be solved to find the coefficient A_ξ, B_ξ, A_η and B_η, which will satisfy the ODEs.

For convenience, define

$$\mathbf{x} = \begin{bmatrix} A_\xi & B_\xi & A_\eta & B_\eta \end{bmatrix}^T, \quad \mathbf{A} = \begin{bmatrix} A_1 & B_1 \\ C_1 & D_1 \end{bmatrix},$$

and

$$\mathbf{b} = \begin{bmatrix} 0 & 0 & a_0\cos^3(\gamma) & -a_0\cos^3(\gamma) \end{bmatrix}^T,$$

where the submatrices of $\mathbf{A}$ are given by

$$A_1 = \begin{bmatrix} 0 & -\omega_\star^2 - U^o_{xx} \\ -U^o_{xy} & 2\omega_\star \end{bmatrix}, \quad B_1 = \begin{bmatrix} 2\omega_\star & -U^o_{xy} \\ -\omega_\star^2 - U^o_{yy} & 0 \end{bmatrix},$$

$$C_1 = \begin{bmatrix} -\omega_\star^2 - U^o_{xx} & 0 \\ -2\omega_\star & -U^o_{xy} \end{bmatrix}, \quad D_1 = \begin{bmatrix} -U^o_{xy} & -2\omega_\star \\ 0 & -\omega_\star^2 - U^o_{yy} \end{bmatrix}.$$

The equation (5.41) is in matrix form $\mathbf{Ax} = \mathbf{b}$, and the solution to the linear system is given by

$$\mathbf{x} = \mathbf{A}^{-1}\mathbf{b}.$$

The coefficients A_ξ, A_η, B_ξ and B_η to be found are amplitudes that characterise the orbit.

As mentioned before (for the collinear points), the out-of-plane motion (equation (5.24)) is decoupled from the in-plane equations of motion ((5.22)-(5.23)), hence the solution of the third equation is given by equation (5.37). Therefore, the required sail acceleration for a fixed out-of-plane displacement distance can be given by

$$a_0 = \frac{\zeta_0 |U^o_{zz}|}{\cos(\gamma)^2 \sin(\gamma)}. \tag{5.42}$$

5.2.1 Effect of a Non-ideal flat sail model

Considering the non-ideal flat sail model, the total force vector can be written in terms of normal and transversal components from the equation (2.37) as

$$\begin{aligned} \boldsymbol{F}_{Sail} &= \sqrt{F_n^2 + F_t^2}\boldsymbol{m}, \\ &= PA\sqrt{(a_1\cos(\gamma) + a_2)^2 + a_3^2\sin^2(\gamma)}\cos(\gamma)\boldsymbol{m}, \end{aligned} \tag{5.43}$$

where $\boldsymbol{m}$ is the unit vector in the direction of the total force.

Furthermore, the solar radiation pressure acceleration is given by

$$\begin{aligned} \boldsymbol{a}_{Sail} &= \frac{P}{\sigma}\sqrt{(a_1\cos(\gamma) + a_2)^2 + a_3^2\sin^2(\gamma)}\cos(\gamma)\boldsymbol{m}, \\ &= \frac{a_0}{2}\sqrt{(a_1\cos(\gamma) + a_2)^2 + a_3^2\sin^2(\gamma)}\cos(\gamma)\boldsymbol{m}, \end{aligned} \tag{5.44}$$

where a_0 is the characteristic acceleration of the non-ideal sail. Thus, the acceleration now acts in direction $\boldsymbol{m}$ rather than normal to the sail surface in direction $\boldsymbol{n}$, as shown in Section 2.1.3 for the ideal sail. It is also observed that there is a significant deviation in force magnitude between the realistic solar sail and the ideal solar sail model. The sail optical parameters given in Table 5.1 for a 100×100 m square solar sail are now used to compare the optical solar sail model (realistic solar sail model) to an ideal solar sail, as shown in Figure 5.2 (a). Then, the force exerted on the realistic solar sail is less than that on the ideal solar sail.

Using the values given in Table 5.1, the characteristic acceleration of the non-ideal sail can be expressed as

$$\begin{aligned} a_0 &= \frac{PA(a_1 + a_2)}{m}, \\ &= \frac{P(a_1 + a_2)}{\sigma}. \end{aligned} \tag{5.45}$$

Similarly, the characteristic acceleration for an ideal sail defined in equation 2.15 is given by

$$a_0 = \frac{2P}{\sigma}. \tag{5.46}$$

Recall that the required sail acceleration for a fixed distance ζ_0 is again given by equation (5.37) as

$$a_0 = \frac{\zeta_0|U_{zz}^o|}{\cos(\gamma)^2\sin(\gamma)}. \tag{5.47}$$

For the realistic solar sail, the out-of-plane distance may then be written approximately as

Table 5.1: Optical coefficients for an ideal solar sail and **JPL** (Jet Propulsion Laboratory) square sail.

	$\tilde{\rho}$	s	ε_f	ε_b	B_f	B_b
Ideal sail	1	1	0	0	$\frac{2}{3}$	$\frac{2}{3}$
Square sail	0.88	0.94	0.05	0.55	0.79	0.55

$$\begin{aligned} \zeta_0^{rss} &= a_0 \cos^2(\gamma) \sin(\gamma) |U_{zz}^o|^{-1}, \\ &= \frac{P(a_1 + a_2)}{\sigma} \cos^2(\gamma) \sin(\gamma) |U_{zz}^o|^{-1}. \end{aligned} \tag{5.48}$$

Similarly, the out-of-plane distance for the ideal solar sail is again given by

$$\zeta_0^{iss} = \frac{2P}{\sigma} \cos^2(\gamma) \sin(\gamma) |U_{zz}^o|^{-1}. \tag{5.49}$$

Comparing equation (5.48) and (5.49), one can see that

$$\begin{aligned} \frac{\zeta_0^{rss}}{\zeta_0^{iss}} &= \frac{a_1 + a_2}{2}, \\ &\approx 0.9081. \end{aligned} \tag{5.50}$$

Therefore, the out-of-plane distance due to the realistic solar sail is less by a factor of order 0.0919 than that on the ideal solar sail. The main effect of the non-perfect sail is to reduce the out-of-plane displacement distance which may be achieved for a given characteristic acceleration.

Again, the realistic solar sail model can be compared with an ideal solar sail using the cone angle, as shown in Figure 5.2 (b). Most importantly, the realistic square solar sail model can only direct its force vector to a maximum cone angle of 55.5° (corresponding to a sail pitch angle of 72.6°) due to the center-line effect. It should be noted that the center-line angle for a perfectly reflecting solar sail vanishes since the force vector is always directed normal to the sail surface, while the non-perfect solar sail has a center-line angle due to the optical absorption. Then, Figure 5.3 shows the variation of the centerline angle as a function of the pitch angle.

Equation (5.48) is approximate since the angle γ is the pitch angle, while for a realistic sail, one should use the cone angle, but the difference will be small.

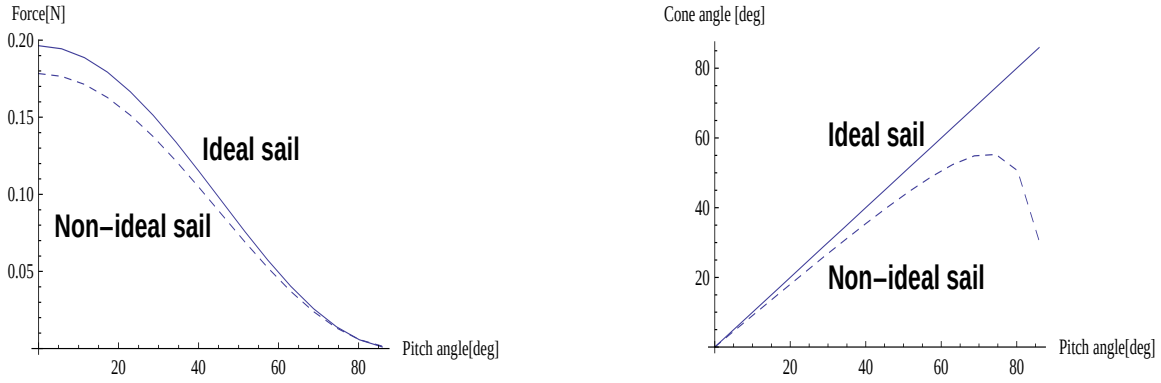

(a) (b)

Figure 5.2: (a) Force exerted on a 100×100 m ideal square solar sail and non-ideal square solar sail at 1 AU; (b) Cone angle for an ideal solar sail and non-ideal solar sail model.

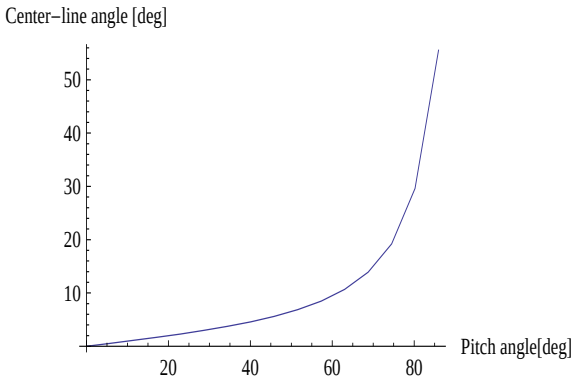

Figure 5.3: Center-line angle for a non-ideal solar sail model.

5.3 One-Month Orbits

This section is concerned with the numerical computation of displaced periodic orbits around the Lagrange points in the Earth-Moon system. The initial conditions are given for different displaced orbits in Table 5.2, 5.3, 5.4 and 5.5. For example, the numerical nonlinear results for the Lagrange points L_3 (Figure 5.4), L_4 (Figure 5.6 (a)), and L_5 (Figure 5.6 (b)) demonstrate, that displaced periodic orbits appear in their vicinity with a period of 28 days (synodic lunar month). As seen from Figure 5.5, the linear analytic solutions (dashed line) match the numerical nonlinear solutions (solid line) for a small displaced orbit but only in some intervals of time since the L_3 point is weakly unstable. The curve of the numerical nonlinear solution for the out-of-plane motion revives and reaches a minimum around $t = 2$, while the curve of the linear analytic solution remains constant. Then, the difference between the linear analytic and numerical nonlinear solutions is about 1 km. The other revival of the numerical nonlinear solution is observed at $t = 5$. At this point, the maximum difference between the linear analytic and numerical nonlinear solutions is approximately 4 km. Furthermore, the numerically integrated nonlinear (solid line) equations match the linear analytic solutions (dashed line) for a small displaced orbit (Figure 5.7, 5.9, 5.11 (a) for L_4 and Figure 5.7, 5.9, 5.11 (b) for L_5). Good agreement was obtained between the linear analytic solutions (dashed line) and the numerical nonlinear solutions (solid line) over the entire period. It was found that for a given displacement distance above/below the Earth-Moon plane it is easier by a factor of order 3.19 to do so at L_4/L_5 compared to L_1/L_2 - ie. for a fixed sail acceleration the displacement distance at L_4/L_5 is greater than that at L_1/L_2. In addition, displaced L_4/L_5 orbits are passively stable, making them more forgiving to sail pointing errors than highly unstable orbits at L_1/L_2. To understand this analysis, recall that the required sail acceleration for a fixed distance ζ_0 depends on the value of U^o_{zz}, which is related to the mass parameter μ. The out-of-plane motion is simple harmonic with a nondimensional frequency of $\omega_\zeta = \sqrt{|U^o_{zz}|}$. Specifically for the L_2 point in the Earth-Moon system $\omega_\zeta = 1.78618$, which corresponds to the factor $|U^o_{zz}| = 3.19043$ as already mentioned above since $|U^o_{zz}| = 1$ at the triangular libration points.

The drawback of the new family of orbits at L_4 and L_5 is the increased telecommunications path-length, particularly the Moon-L_4 distance compared to the Moon-L_2 distance. The collinear libration points L_1, L_2, and L_3 are unstable equilibria, which implies the instability of any trajectory around these points, such that the exact computation of the displaced orbits is required for their maintenance.

Table 5.2: Initial conditions related to L_3 (see Figure 5.4 for the orbit and Figure 5.5 for the comparison between the analytical and nonlinear results) for a constant displacement distance of $\zeta = 100\ km$.

	L_3
ξ_0	6.6986×10^{-3}
η_0	-1.4254×10^{-2}
$a_0[mms^{-2}]$	0.0018

Table 5.3: Initial conditions related to L_4 (see Figure 5.6 (a) for the orbit and Figure 5.7 (a) for the comparison between the analytical and nonlinear results), and L_5 (see Figure 5.6 (b) for the orbit and Figure 5.7 (b) for the comparison between the analytical and nonlinear results) for a constant displacement distance of $\zeta = 100\ km$.

	L_4	L_5
A_ξ	4.0539×10^{-2}	4.0539×10^{-2}
B_ξ	-1.0383×10^{-2}	1.0383×10^{-2}
A_η	1.0383×10^{-2}	-1.0383×10^{-2}
B_η	-2.8251×10^{-2}	-2.8251×10^{-2}
$a_0[mms^{-2}]$	0.0018	0.0018

Table 5.4: Initial conditions related to L_4 (see Figure 5.8 (a) for the orbit and Figure 5.9 (a) for the comparison between the analytical and nonlinear results), and L_5 (see Figure 5.8 (b) for the orbit and Figure 5.9 (b) for the comparison between the analytical and nonlinear results) for a constant displacement distance of $\zeta = 200\ km$.

	L_4	L_5
A_ξ	8.6238×10^{-2}	8.6238×10^{-2}
B_ξ	-2.2053×10^{-2}	2.2053×10^{-2}
A_η	2.2053×10^{-2}	-2.2053×10^{-2}
B_η	-6.0139×10^{-2}	-6.0139×10^{-2}
$a_0[mms^{-2}]$	0.0036	0.0036

Table 5.5: Initial conditions related to L_4 (see Figure 5.10 (a) for the orbit and Figure 5.11 (a) for the comparison between the analytical and nonlinear results), and L_5 (see Figure 5.10 (b) for the orbit and Figure 5.11 (b) for the comparison between the analytical and nonlinear results) for a constant displacement distance of $\zeta = 500\ km$.

	L_4	L_5
A_ξ	2.0269×10^{-1}	2.0269×10^{-1}
B_ξ	-5.1915×10^{-2}	5.1915×10^{-2}
A_η	5.1915×10^{-2}	-5.1915×10^{-2}
B_η	-1.4125×10^{-1}	-1.4125×10^{-1}
$a_0[mms^{-2}]$	0.0092	0.0092

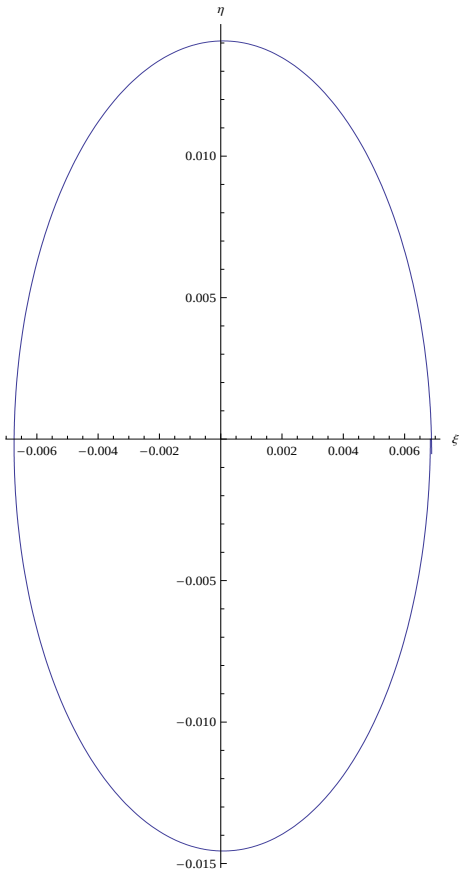

Figure 5.4: Periodic orbit at linear order around L_3 ($\zeta = 100\ km$).

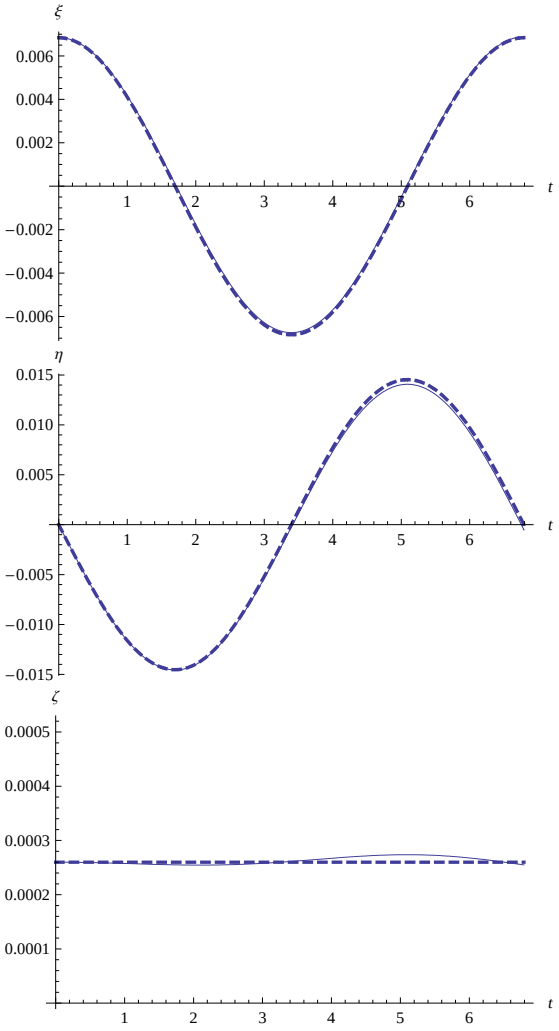

Figure 5.5: Comparison between the analytical (dashed line) and nonlinear (solid line) results (L_3) for a constant displacement distance of $\zeta = 100\ km$.

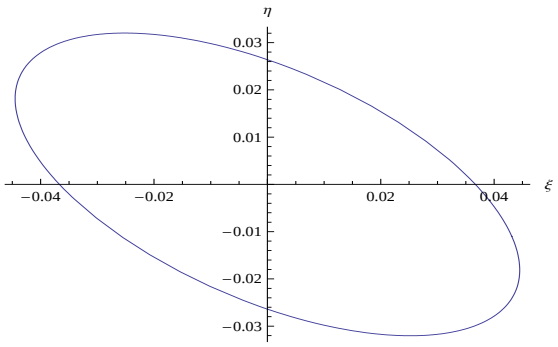

(a)

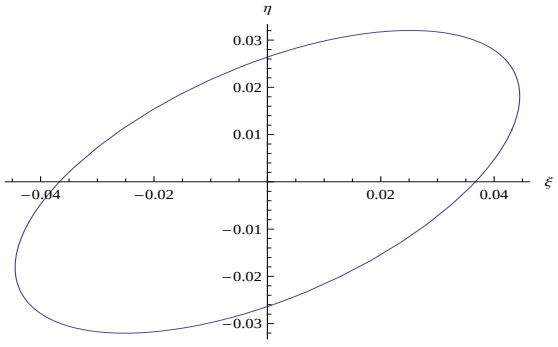

(b)

Figure 5.6: (a) Periodic orbits at linear order around L_4; (b) Periodic orbits at linear order around L_5 ($\zeta = 100\ km$).

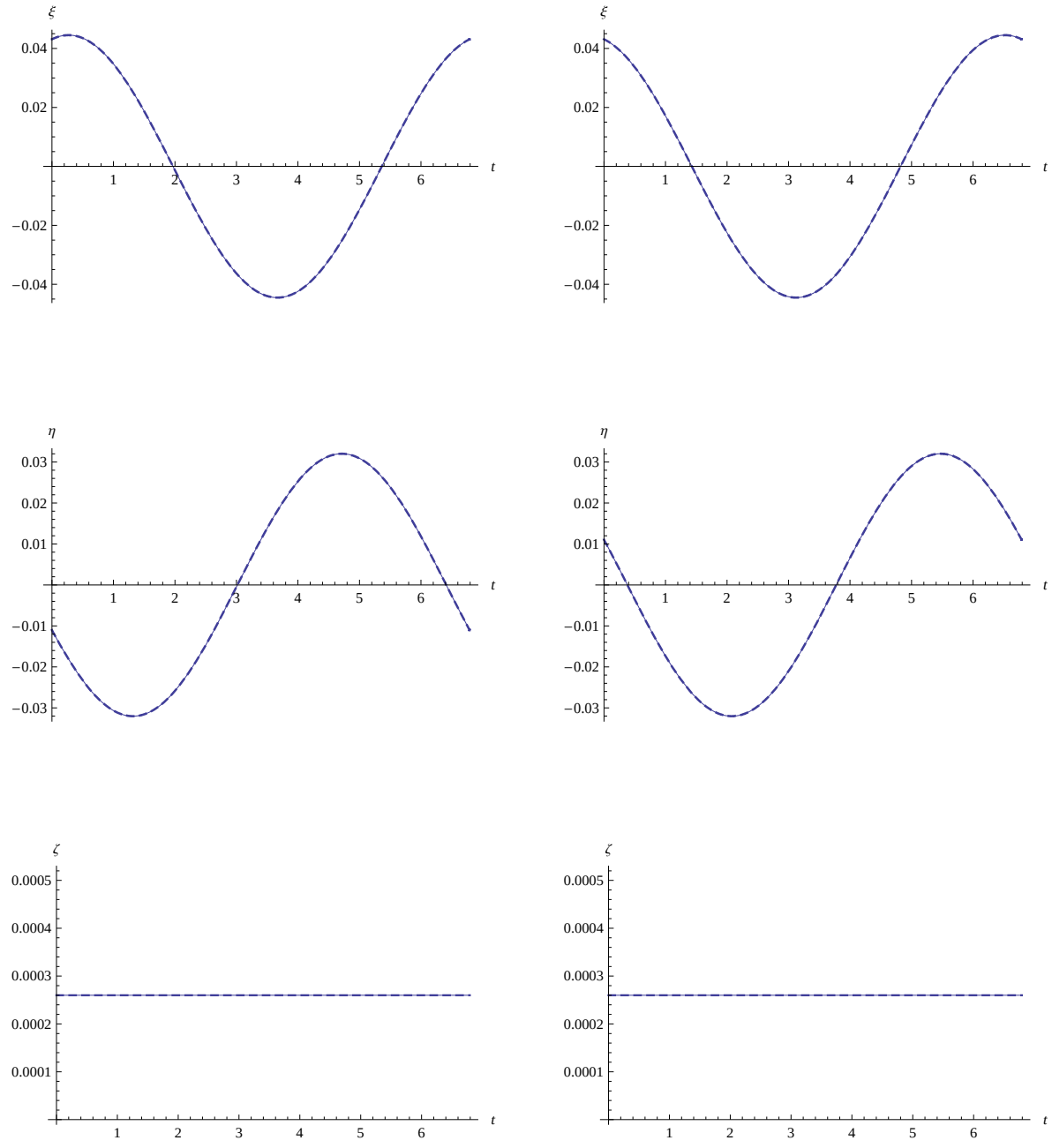

(a) (b)

Figure 5.7: (a) Comparison between the analytical (dashed line) and nonlinear (solid line) results (L_4) for a constant displacement distance of $\zeta = 100\ km$; (b) Comparison between the analytical (dashed line) and nonlinear (solid line) results (L_5) for a constant displacement distance of $\zeta = 100\ km$.

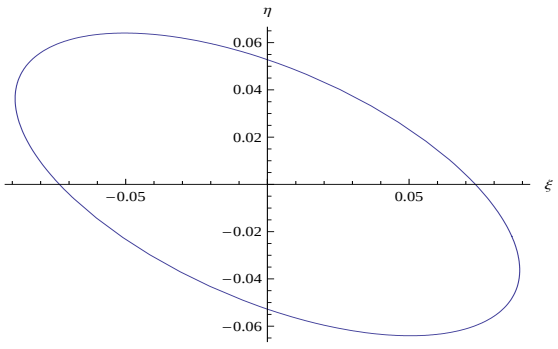

(a)

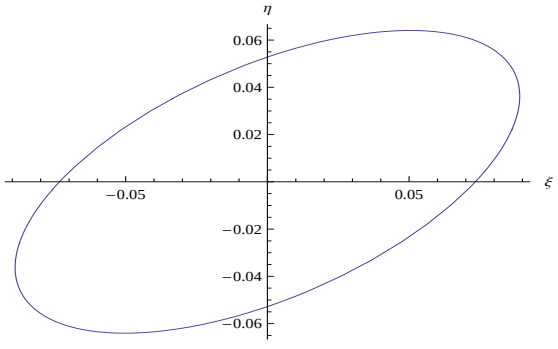

(b)

Figure 5.8: (a) Periodic orbits at linear order around L_4; (b) Periodic orbits at linear order around L_5 ($\zeta = 200\ km$).

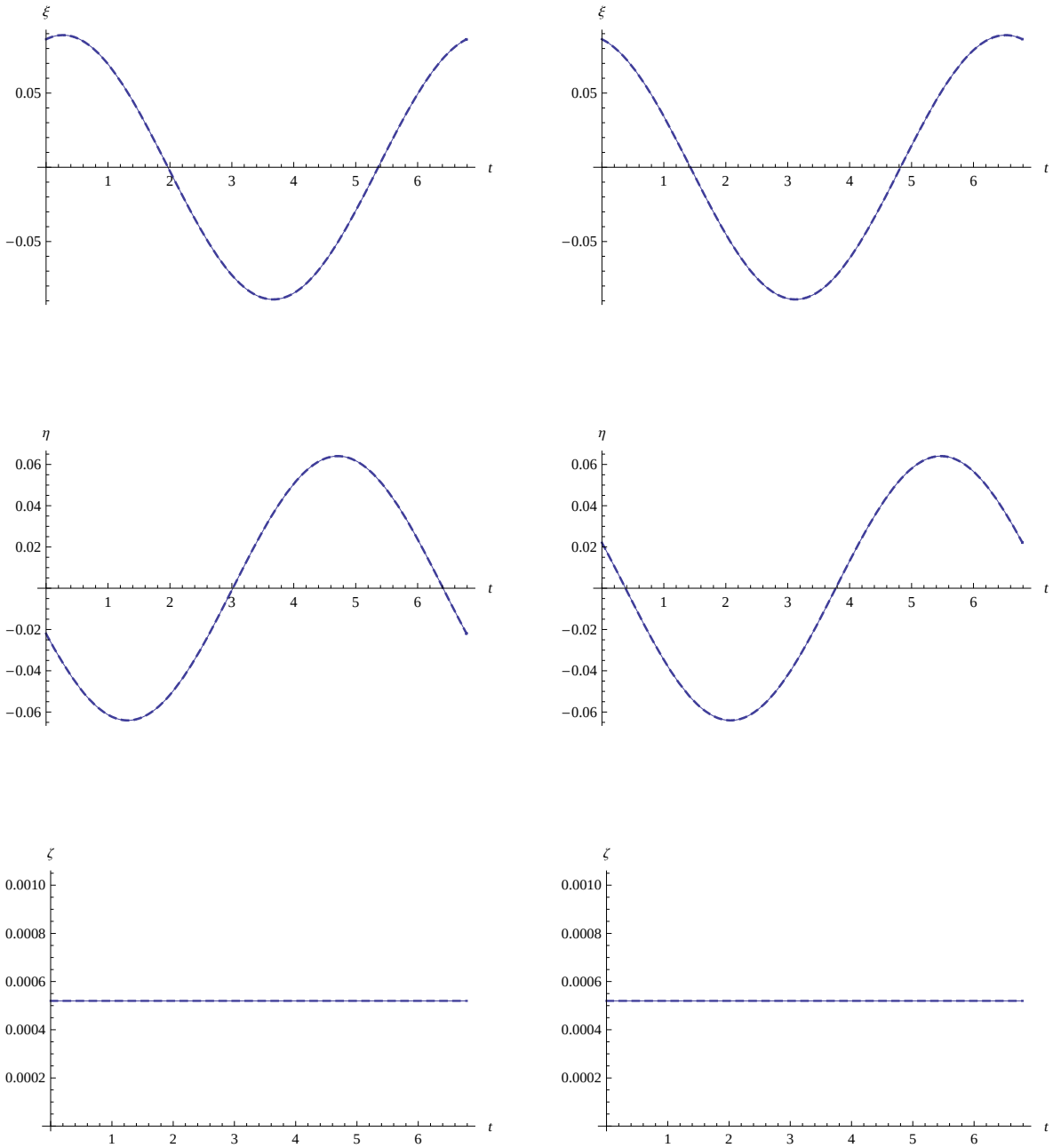

(a) (b)

Figure 5.9: (a) Comparison between the analytical (dashed line) and nonlinear (solid line) results (L_4) for a constant displacement distance of $\zeta = 200\ km$; (b) Comparison between the analytical (dashed line) and nonlinear (solid line) results (L_5 for a constant displacement distance of $\zeta = 200\ km$).

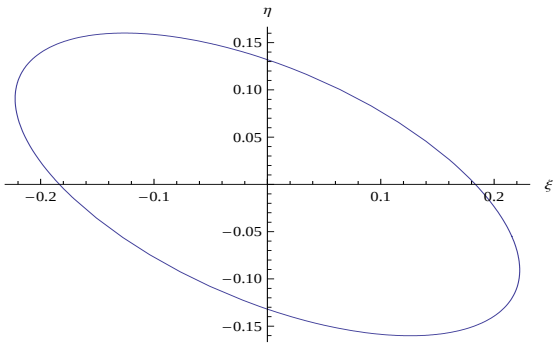

(a)

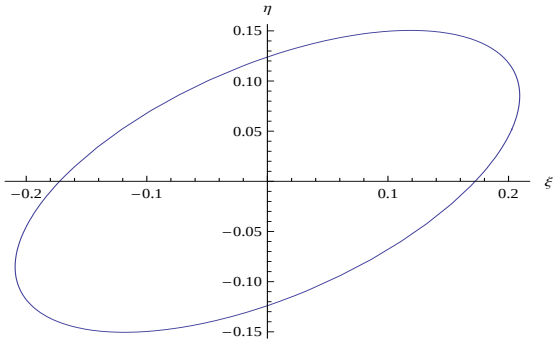

(b)

Figure 5.10: (a) Periodic orbits at linear order around L_4; (b) Periodic orbits at linear order around L_5 ($\zeta = 500\ km$).

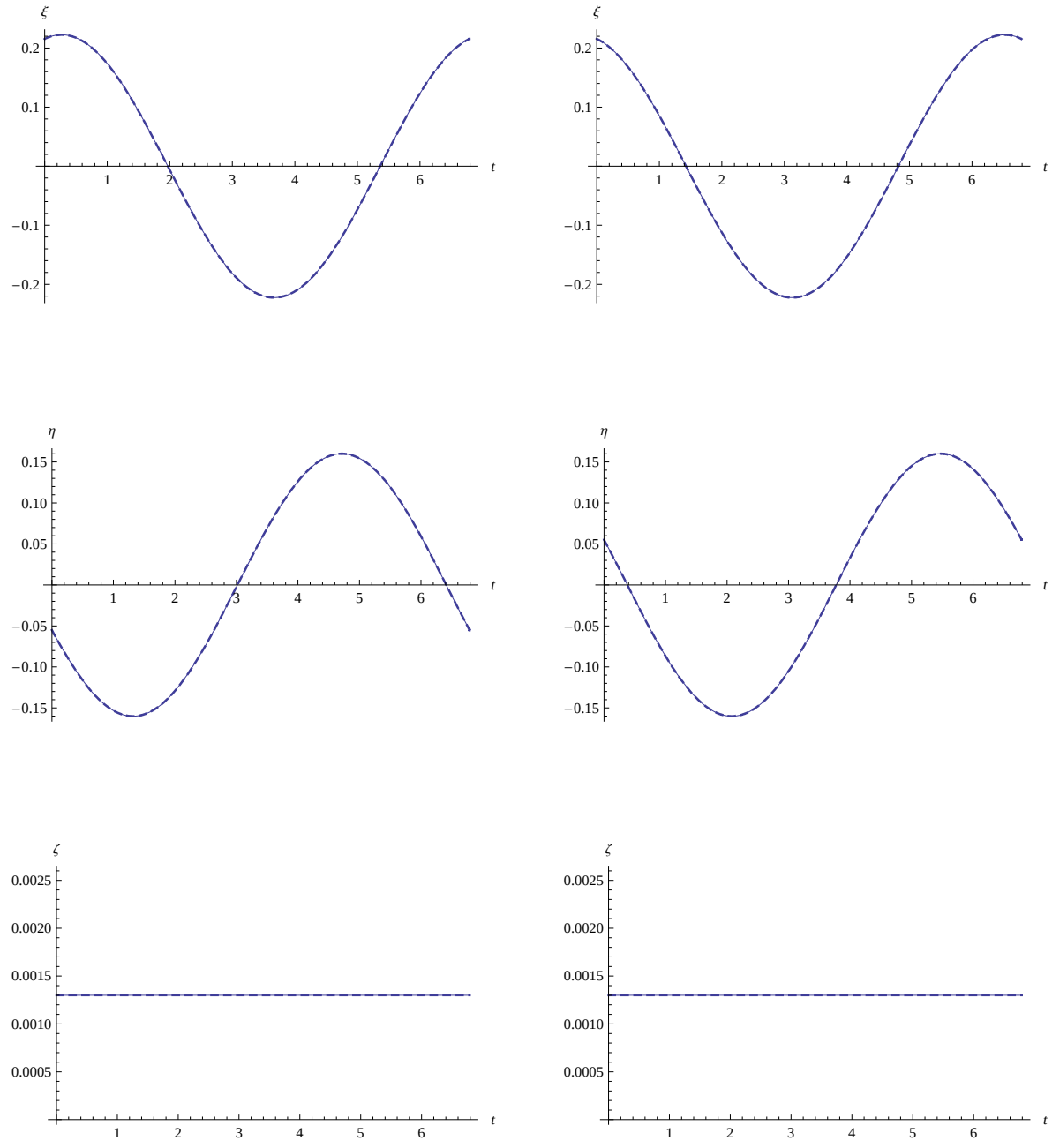

(a) (b)

Figure 5.11: (a) Comparison between the analytical (dashed line) and nonlinear (solid line) results (L_4) for a constant displacement distance of $\zeta = 500\ km$; (b) Comparison between the analytical (dashed line) and nonlinear (solid line) results (L_5) for a constant displacement distance of $\zeta = 500\ km$.

5.4 Control of Sail z-Position

In this section the problem of maintaining a constant sail displacement at a passively stable triangular libration point is considered. To accomplish this task a simple control methodology is developed for stationing the solar sail. The control is achieved by using small variations in the sail's orientation.

Recall that the motion along the z-axis is independent of the motion in the xy-plane. Thus, a z-axis control of the sail orbit is studied. The z-position is maintained at the triangular libration points by adjusting the control angle γ in such a way that it will cancel disturbances that drive the sail away from those points. In particular the constant displacement distance found from the analytic solution will be maintained in the full nonlinear system using the simple feedback control to the sail pitch angle.

The linear feedback controller is developed by linearising the z-dynamics around the triangular libration points and some sail attitude γ_0.

From the equation (5.24), the linearisation of the uncoupled motion about γ_0 gives

$$\ddot{\zeta} = \left.\frac{\partial^2 U}{\partial z^2}\right|_o \zeta + a_0 \cos^2(\gamma_0)\sin(\gamma_0), \tag{5.51}$$

where the subscript o refers to the triangular libration point. If $\ddot{\zeta} = 0$, the condition for out-of-plane equilibrium is given by

$$a_0 \cos^2(\gamma_0)\sin(\gamma_0) = -\left.\frac{\partial^2 U}{\partial z^2}\right|_o \zeta_0. \tag{5.52}$$

Now let

$$\zeta = \zeta_0 + \delta\zeta, \tag{5.53}$$
$$\gamma = \gamma_0 + \delta\gamma. \tag{5.54}$$

By making use of Eqs. (5.53) and (5.54), the uncoupled motion (Eq. (5.24)) can be stated as

$$\begin{aligned}\frac{d^2}{dt^2}\Big(\zeta_0 + \delta\zeta\Big) &= \left.\frac{\partial^2 U}{\partial z^2}\right|_o \Big(\zeta_0 + \delta\zeta\Big) + a_0 \cos^2(\gamma_0)\sin(\gamma_0) \\ &\quad + a_0\Big(\cos^3(\gamma_0) - 2\cos(\gamma_0)\sin^2(\gamma_0)\Big)\delta\gamma.\end{aligned} \tag{5.55}$$

Applying Eq. (5.52), then Eq. (5.55) can now be rewritten as

$$\delta\ddot{\zeta} = \left.\frac{\partial^2 U}{\partial z^2}\right|_o \delta\zeta + a_0\Big(\cos^3(\gamma_0) - 2\cos(\gamma_0)\sin^2(\gamma_0)\Big)\delta\gamma, \tag{5.56}$$

where $\gamma_0 \neq 35.264°$, since the last term of Eq. (5.56) would vanish.

By setting

$$A = \left.\frac{\partial^2 U}{\partial z^2}\right|_o, \tag{5.57}$$

$$B = a_0\Big(\cos^2(\gamma_0) - 2\cos(\gamma_0)\sin^2(\gamma_0)\Big)\delta\gamma, \tag{5.58}$$

Eq. (5.56) can also be rearranged as

$$\delta\ddot{\zeta} = A\cdot\delta\zeta + B\cdot\delta\gamma. \tag{5.59}$$

Now it is possible to design the linear feedback controller of the form

$$\delta\gamma = C\cdot\delta\zeta + D\cdot\delta\dot{\zeta}, \tag{5.60}$$

where C and D are the controller gains. Thus, the controller will maintain the sail at a fixed displacement above the triangular libration points. Again, this is of benefit for lunar communication applications.

Substituting Eq. (5.60) into Eq. (5.59), it can be seen that

$$\begin{aligned}\delta\ddot{\zeta} &= A\cdot\delta\zeta + B(C\cdot\delta\zeta + D\cdot\delta\dot{\zeta}),\\ &= (A+BC)\cdot\delta\zeta + D\cdot\delta\dot{\zeta},\end{aligned} \tag{5.61}$$

and so

$$\delta\ddot{\zeta} - (A+BC)\cdot\delta\zeta - D\cdot\delta\dot{\zeta} = 0, \tag{5.62}$$

where D the damping coefficient is chosen such that the system converges as a critically damped system.

Figure 5.12(a) (resp. 5.12(b)) shows the sail's trajectory around L_4 (resp. L_5) using the linear feedback controller on the nonlinear system. Figure 5.13(a) (resp. 5.13(b)) shows the simulation results for L_4 (resp. L_5) using this controller on sail x, y, z-position. The control angle history for the L_4 (resp. L_5) quasi-periodic orbits is shown in Figure 5.14 (a) (resp. 5.14 (b)). It should be noted that while the z displacement is almost constant, in-plane dynamics are excited, but are however passively stable. The controller is able to compensate for the out-of-plane disturbances due to the nonlinear system [154, 155, 156, 157, 158].

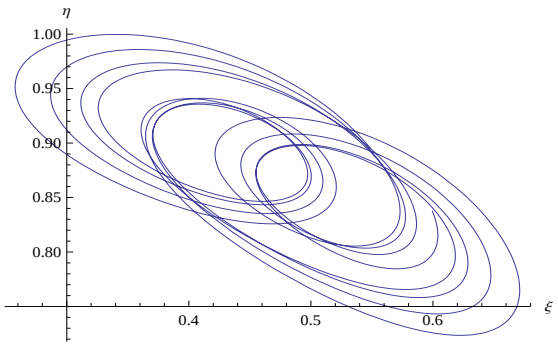

(*a*)

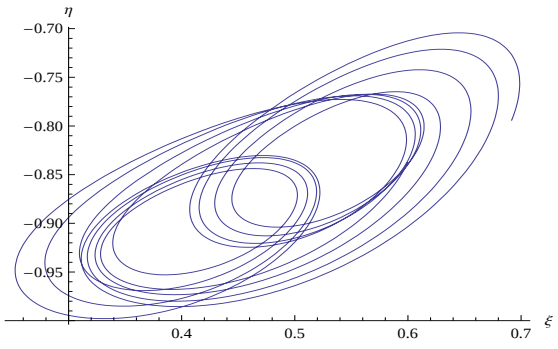

(*b*)

Figure 5.12: (*a*) Quasi-periodic orbits around L_4; (*b*) Quasi-periodic orbits around L_5.

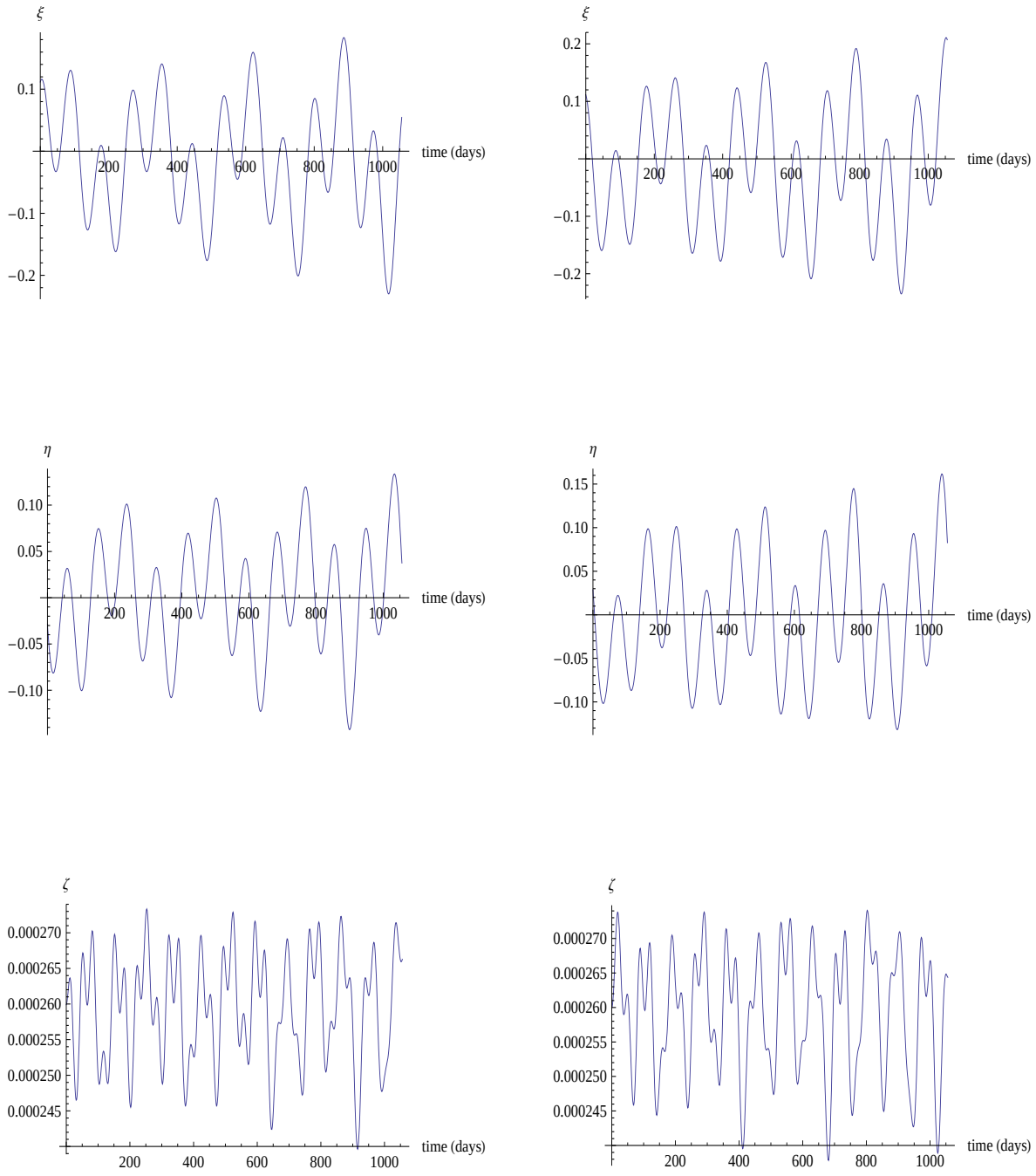

(a) (b)

Figure 5.13: (a) Linear feedback control on sail x, y, z-position (L_4); (b) Linear feedback control on sail x, y, z-position (L_5).

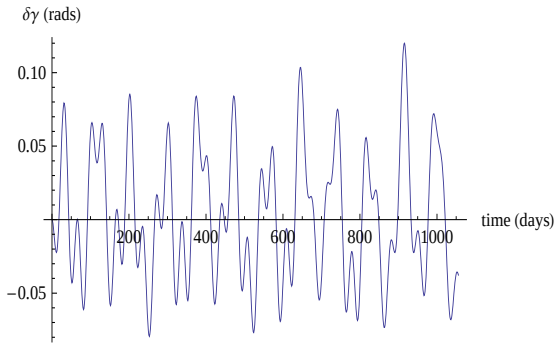

(a)

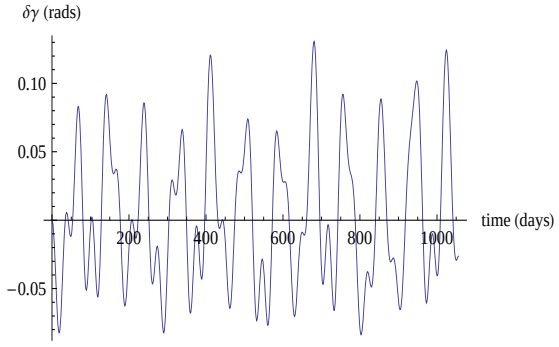

(b)

Figure 5.14: (a) Control history for the L_4 quasi-periodic orbits; (b) Control history for the L_5 quasi-periodic orbits.

5.5 Catalogue of Orbits

Recall that the the linearised equations of motion of a solar sail around the collinear libration points are given from equation (5.19) to equation (5.21).

From Section 4.1.1 the homogeneous solution to the linearized equations of motion ((5.19)-(5.21)) is given by

$$\begin{aligned}
\xi_h(t) &= A_1 e^{\nu_{\xi\eta} t} + A_2 e^{-\nu_{\xi\eta} t} + A_3 \cos(\omega_{\xi\eta} t) + A_4 \sin(\omega_{\xi\eta} t), \\
\eta_h(t) &= k_1 A_1 e^{\nu_{\xi\eta} t} - k_1 A_2 e^{-\nu_{\xi\eta} t} - k_2 A_4 \cos(\omega_{\xi\eta} t) + k_2 A_3 \sin(\omega_{\xi\eta} t), \\
\zeta_h(t) &= C_1 \cos(\omega_\zeta t) + C_2 \sin(\omega_\zeta t),
\end{aligned}$$

which for periodic motion can then be written as

$$\begin{aligned}
\xi_h(t) &= A_3 \cos(\omega_{\xi\eta} t) + A_4 \sin(\omega_{\xi\eta} t), \\
\eta_h(t) &= -k_2 A_4 \cos(\omega_{\xi\eta} t) + k_2 A_3 \sin(\omega_{\xi\eta} t), \\
\zeta_h(t) &= C_1 \cos(\omega_\zeta t) + C_2 \sin(\omega_\zeta t).
\end{aligned}$$

After rearranging, the solution can be expressed in a more convenient form as

$$\begin{aligned}
\xi_h(t) &= A_\xi \cos(\omega_{\xi\eta} t + \phi), \\
\eta_h(t) &= k_2 A_\xi \sin(\omega_{\xi\eta} t + \phi), \\
\zeta_h(t) &= A_\zeta \cos(\omega_\zeta t + \psi),
\end{aligned}$$

where again $\omega_{\xi\eta}$ and ω_ζ are the linearized frequencies and k_2 is a constant. The parameters A_ξ and A_ζ are the amplitudes of the in-plane and out-of-plane motion, and ϕ, ψ are the phase angles.

The particular solutions to the inhomogeneous linear equations can be obtained as follows

$$\begin{aligned}
\xi_p(t) &= -a_0 \cos^3(\gamma) \cos(\omega_\star t) \frac{(\omega_\star^2 + 2\omega_\star^2 + 1 - c_2)}{\omega_\star^4 + \omega_\star^2(c_2 - 2) - 2c_2^2 + c_2 + 1}, \\
\eta_p(t) &= a_0 \cos^3(\gamma) \sin(\omega_\star t) \frac{(\omega_\star^2 + 2\omega_\star^2 + 2c_2 + 1)}{\omega_\star^4 + \omega_\star^2(c_2 - 2) - 2c_2^2 + c_2 + 1}, \\
\zeta_p(t) &= \frac{a_0 \cos^2(\gamma) \sin(\gamma)}{\omega_\zeta}.
\end{aligned}$$

Thus, the general solution is obtained by adding the homogeneous solution to a particular solution of the inhomogeneous linear equation ($\xi(t) = \xi_h(t) + \xi_p(t),\ \eta(t) = \eta_h(t) + \eta_p(t),\ \zeta(t) = \zeta_h(t) + \zeta_p(t)$). The analytical solutions to the three-body solar sail of the

linearised equations of motion about the libration points are obtained. The approximate analytical solutions are utilised to determine Lissajous trajectories. A sample Lissajous orbit in the vicinity of the L_1 and L_2 libration points are generated in the Earth-Moon system. As already mentioned, the input amplitudes are required for the analytical results and numerical simulations. The orbit size is represented by the input amplitudes A_ξ and A_ζ, which were arbitrarily selected for illustration. The result is a small (see Figure (5.15), (5.16) about L_1 and Figure (5.19), (5.20) about L_2), and large (see Figure (5.17), (5.18) about L_1 and Figure (5.21, (5.22) about L_2) Lissajous trajectories associated with the L_1 and L_2 point in the Earth-Moon system. The rotation of the in-plane motion can be explained by the fact that the forcing term is not at the in-plane frequency $\omega_{\xi\eta}$.

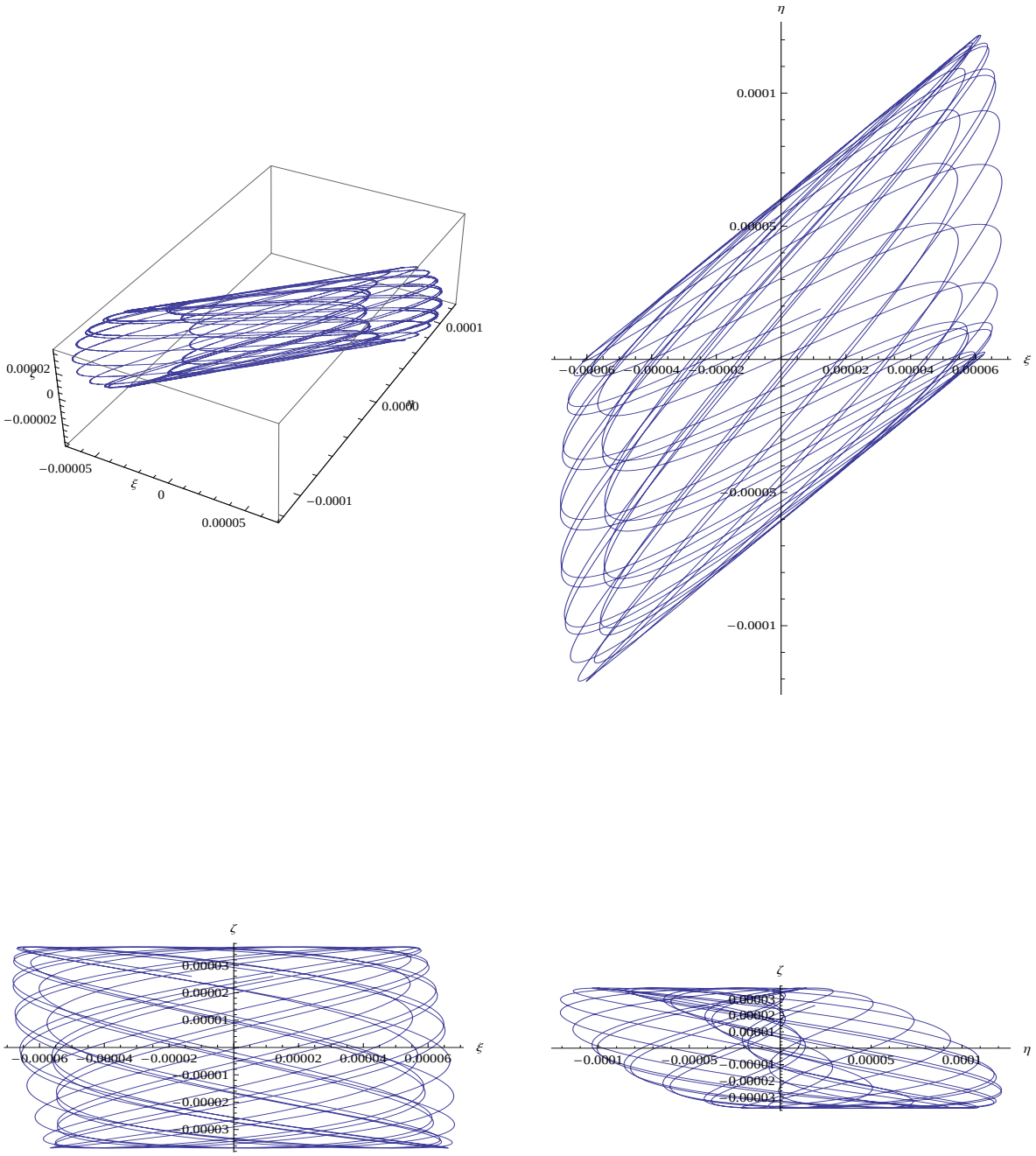

Figure 5.15: Small L_1 trajectory ($a_0 = 0.00094\ mm/s^2$). From left to right, top to bottom: $\xi\eta$, $\xi\zeta$ and $\eta\zeta$ projections ($A_\xi = 2.42\ km$, $A_\zeta = 10\ km$).

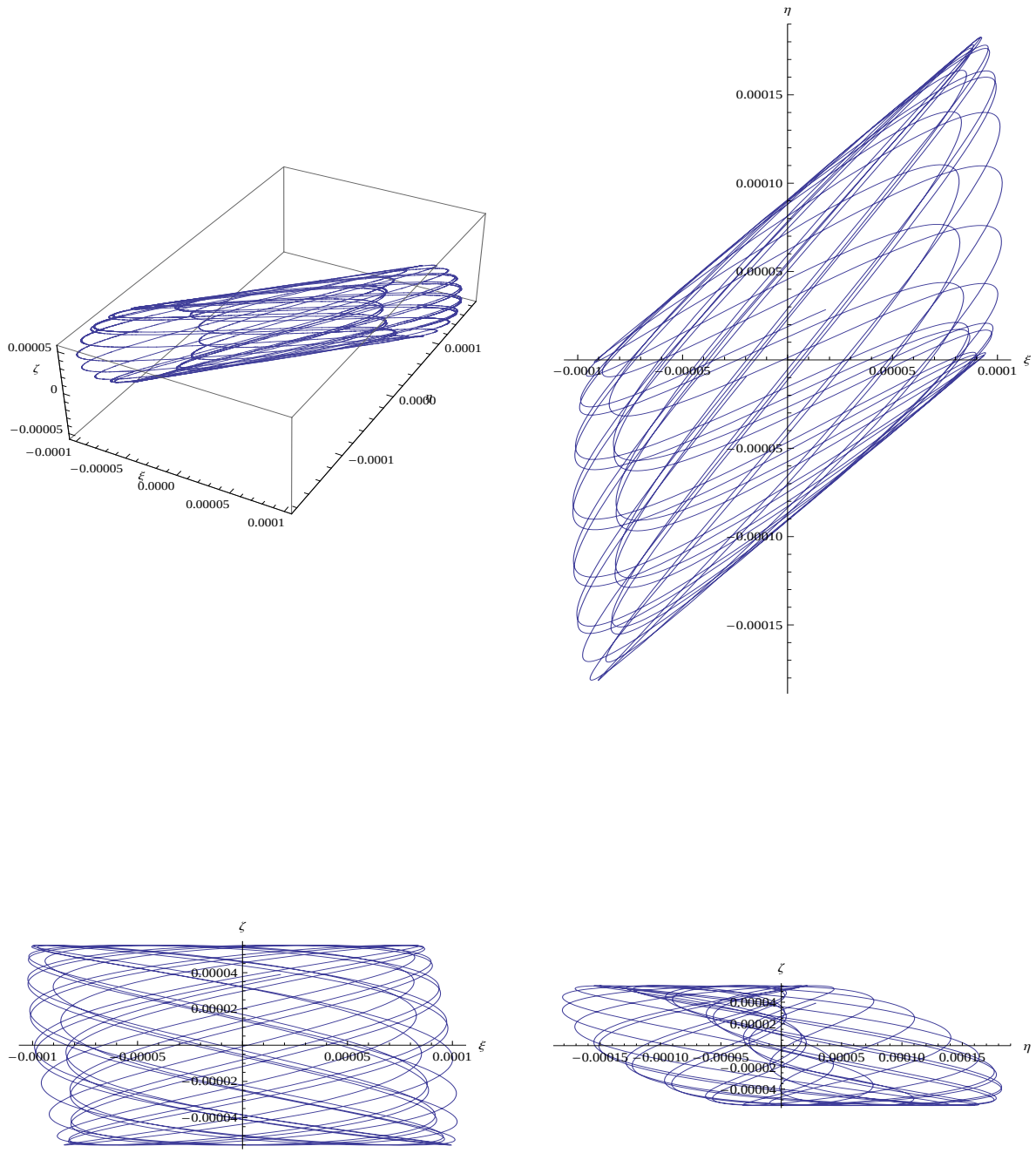

Figure 5.16: Small L_1 trajectory ($a_0 = 0.0014\ mm/s^2$). From left to right, top to bottom: $\xi\eta$, $\xi\zeta$ and $\eta\zeta$ projections ($A_\xi = 3.63\ km$, $A_\zeta = 15\ km$).

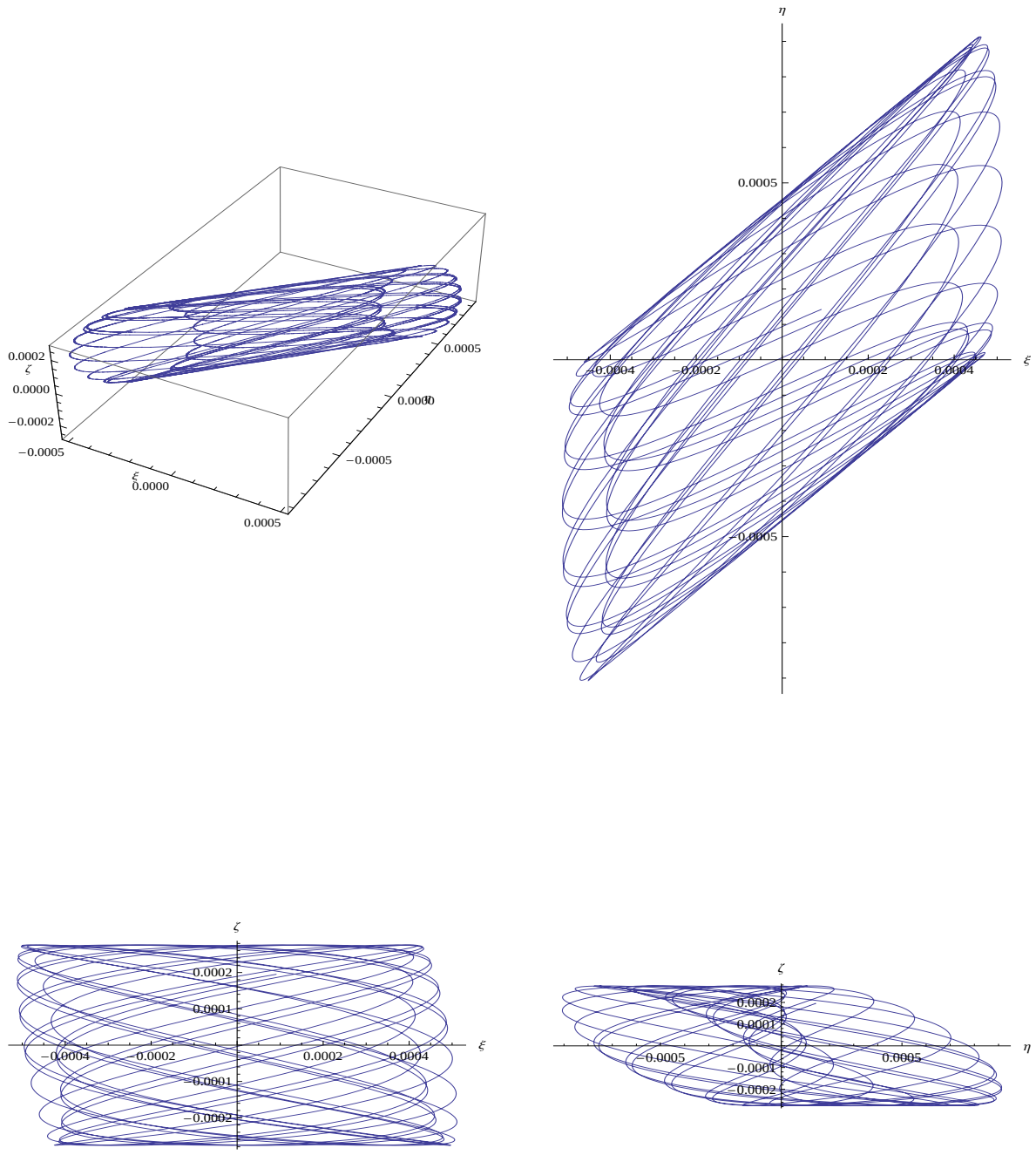

Figure 5.17: Large L_1 trajectory ($a_0 = 0.0071\ mm/s^2$). From left to right, top to bottom: $\xi\eta$, $\xi\zeta$ and $\eta\zeta$ projections ($A_\xi = 18.13\ km$, $A_\zeta = 75\ km$).

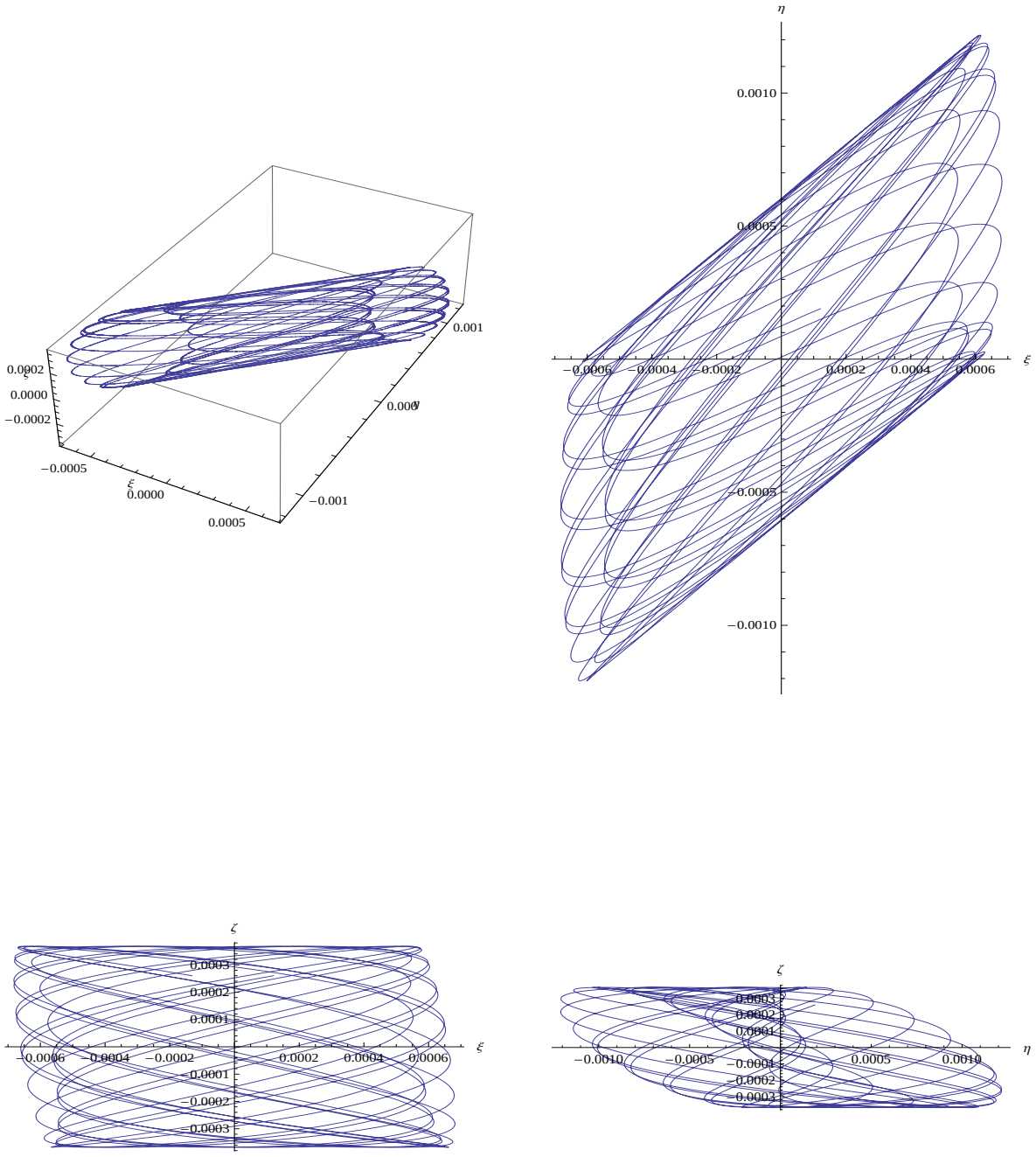

Figure 5.18: Large L_1 trajectory ($a_0 = 0.0094\ mm/s^2$). From left to right, top to bottom: $\xi\eta$, $\xi\zeta$ and $\eta\zeta$ projections ($A_\xi = 24.16\ km$, $A_\zeta = 100\ km$).

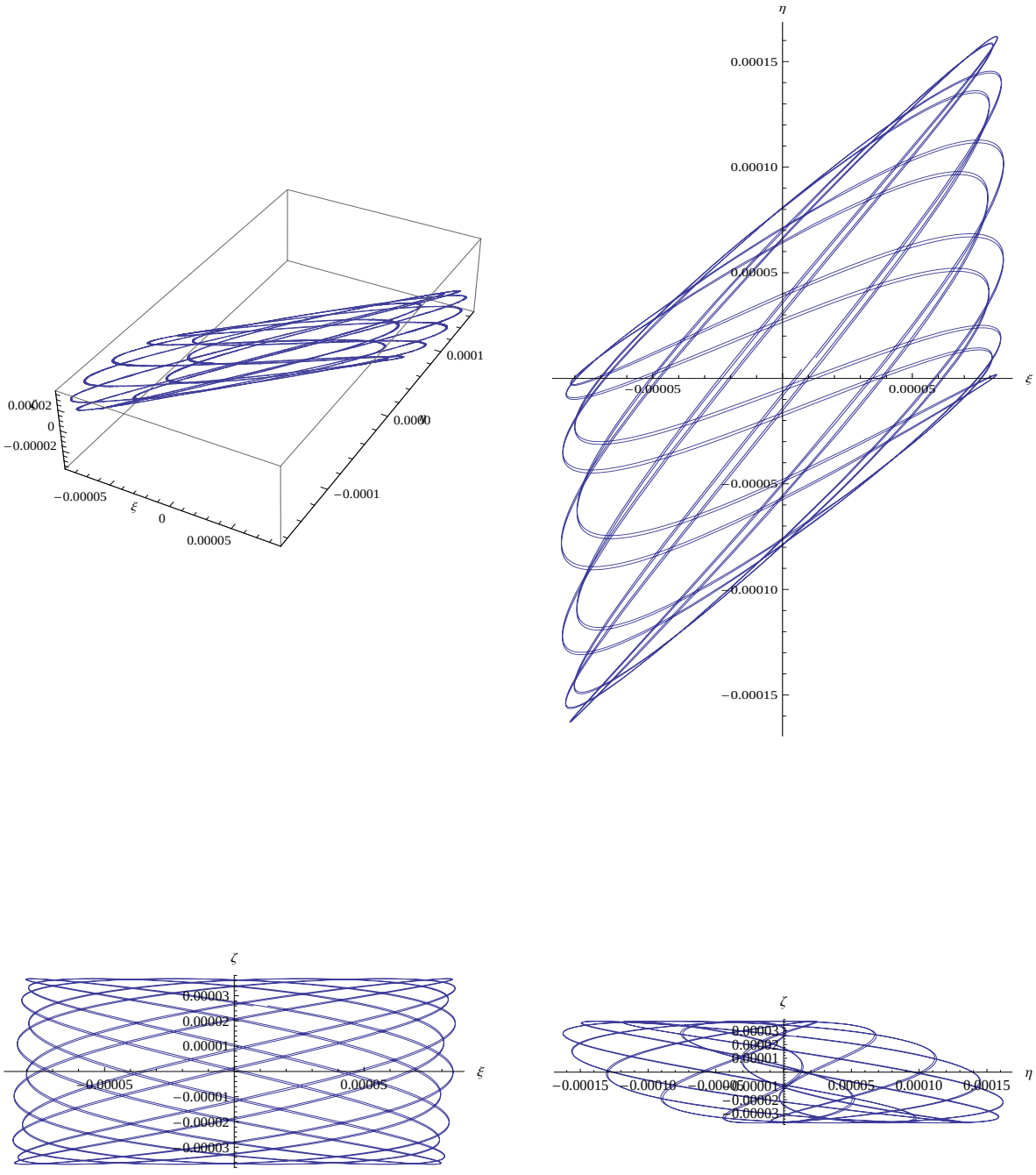

Figure 5.19: Small L_2 trajectory ($a_0 = 0.00058\ mm/s^2$). From left to right, top to bottom: $\xi\eta$, $\xi\zeta$ and $\eta\zeta$ projections ($A_\xi = 1.62\ km$, $A_\zeta = 10\ km$).

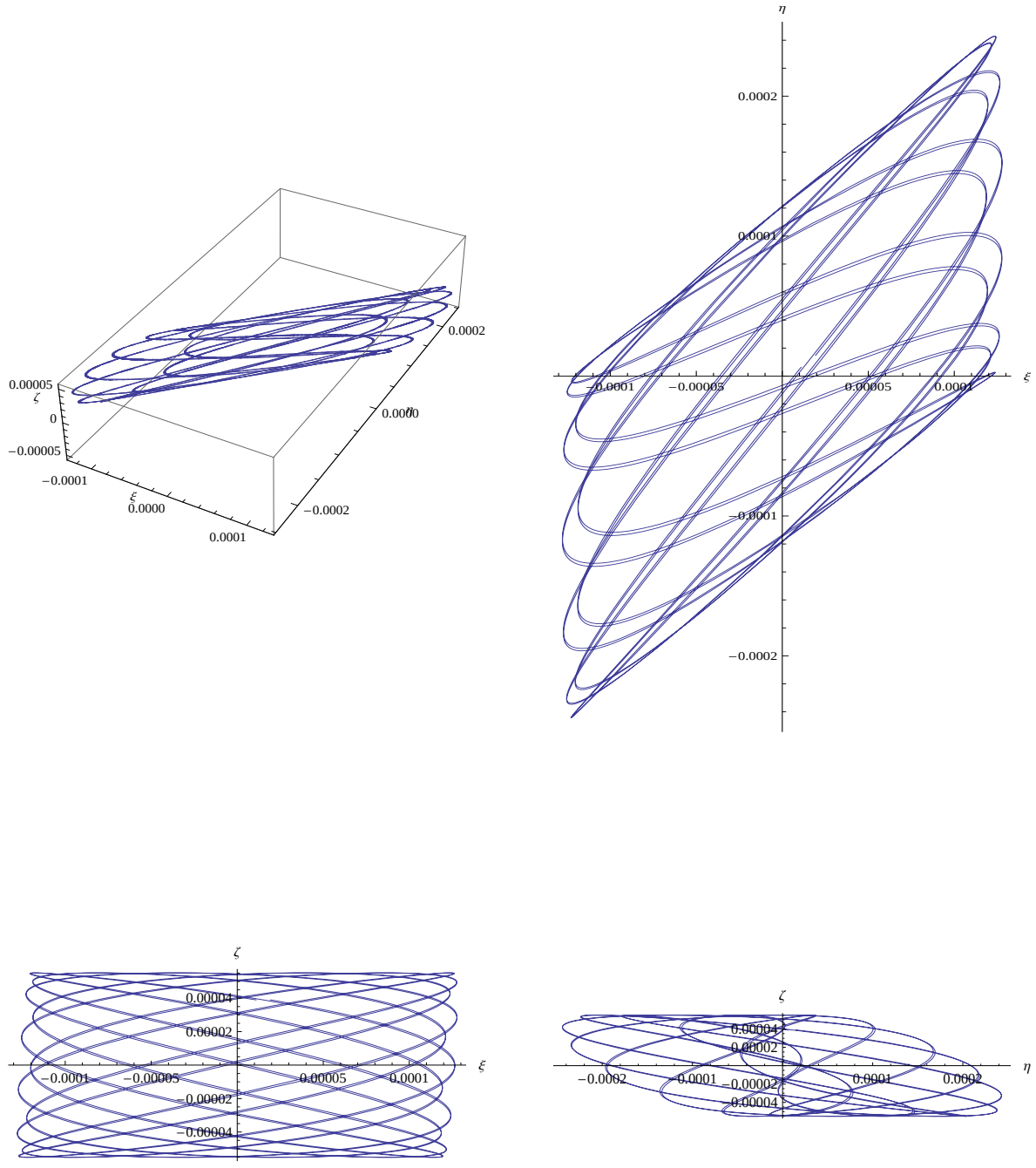

Figure 5.20: Small L_2 trajectory ($a_0 = 0.00088\ mm/s^2$). From left to right, top to bottom: $\xi\eta$, $\xi\zeta$ and $\eta\zeta$ projections ($A_\xi = 2.42\ km$, $A_\zeta = 15\ km$).

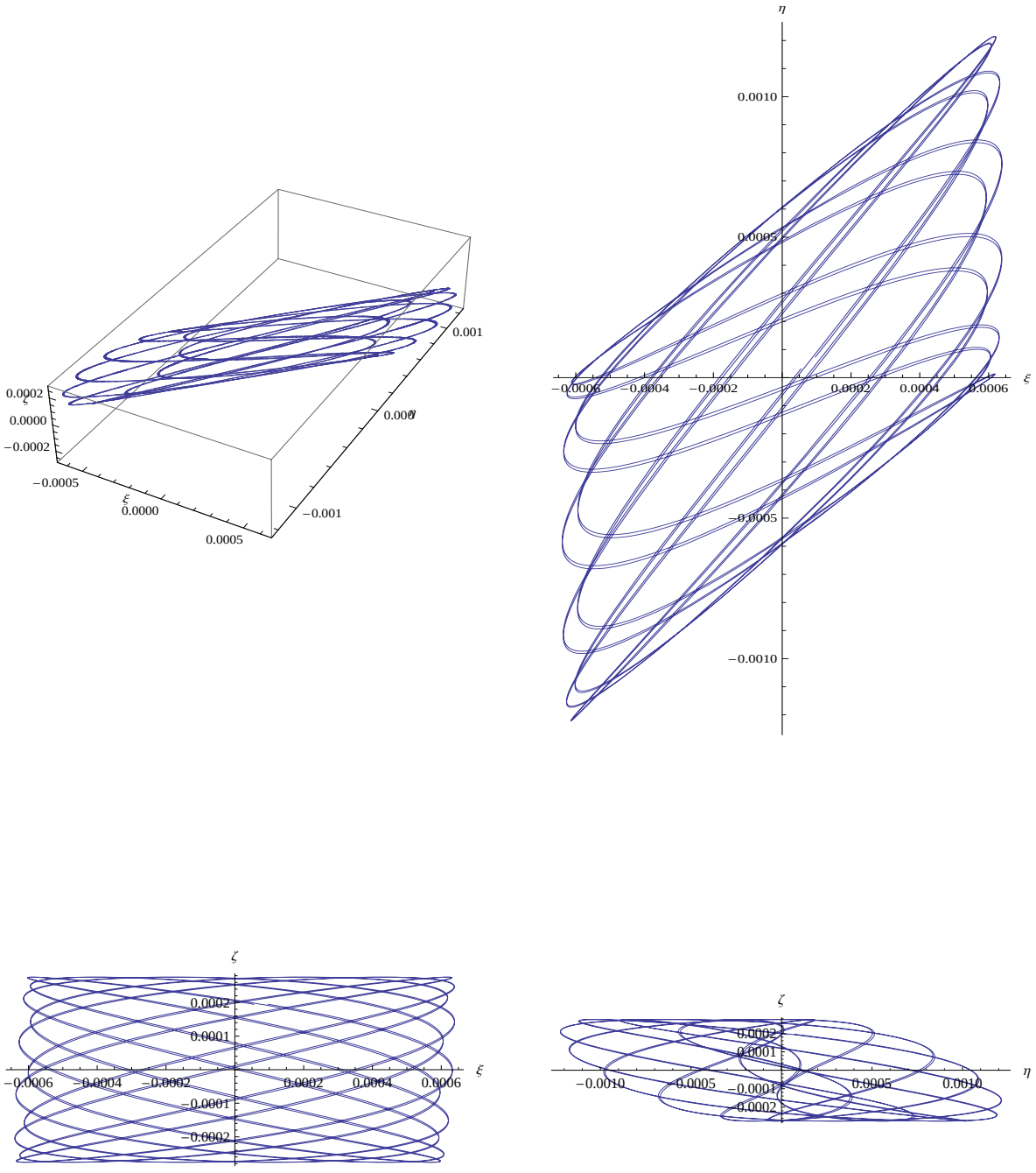

Figure 5.21: Large L_2 trajectory ($a_0 = 0.0044\ mm/s^2$). From left to right, top to bottom: $\xi\eta$, $\xi\zeta$ and $\eta\zeta$ projections ($A_\xi = 12.11\ km$, $A_\zeta = 75\ km$).

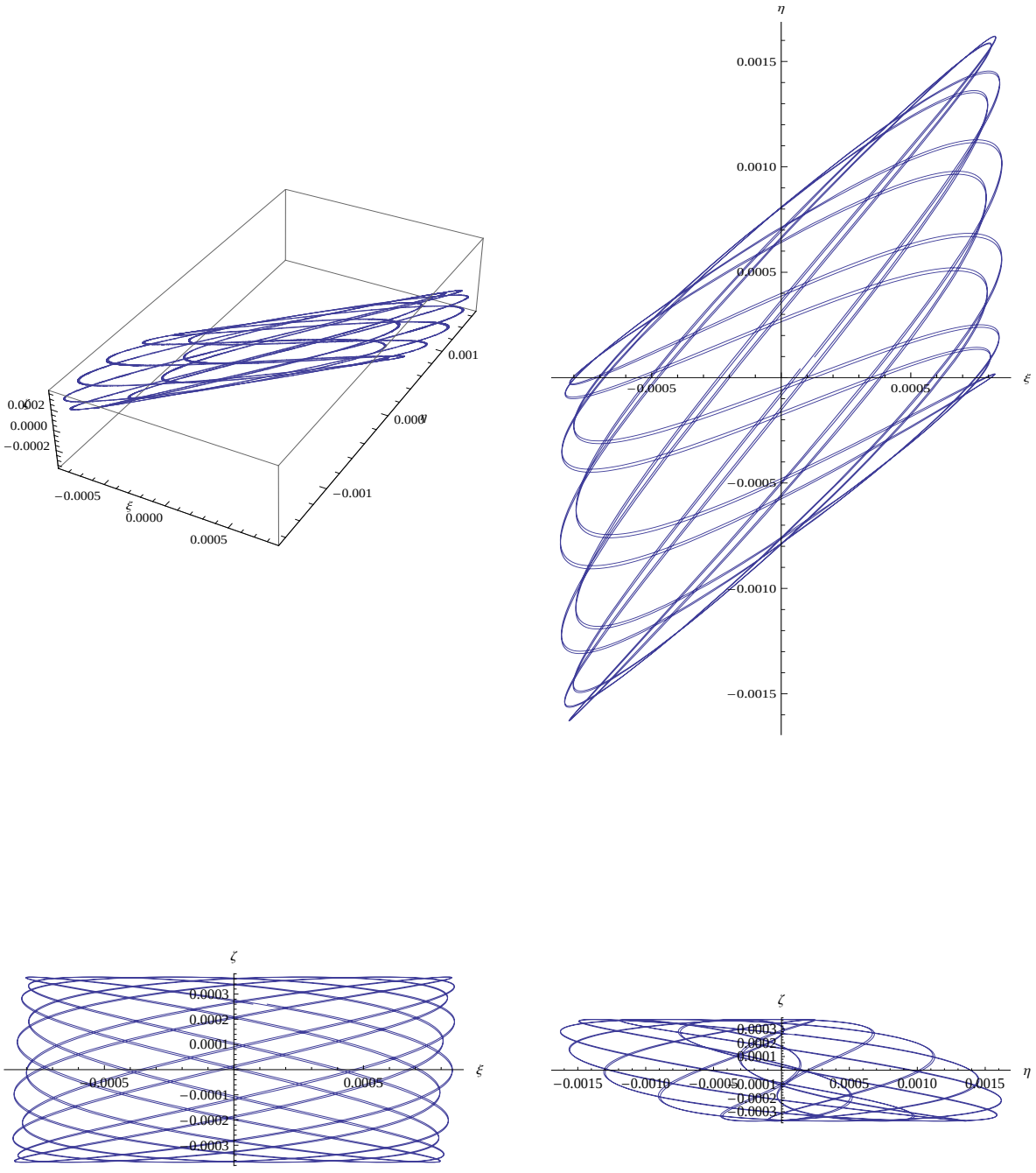

Figure 5.22: Large L_2 trajectory ($a_0 = 0.0058\ mm/s^2$). From left to right, top to bottom: $\xi\eta$, $\xi\zeta$ and $\eta\zeta$ projections ($A_\xi = 16.15\ km$, $A_\zeta = 100\ km$).

5.6 Summary

In this Chapter a novel family of displaced periodic orbits at linear order using solar sail propulsion have been presented from the non-autonomous Earth-Moon system. Using the linearised equations of motion around the Lagrange points, periodic orbits that are displaced can be derived, which will be interesting for future mission design for lunar communication applications. Even though these results offer insight into the dynamics of the system, it has to be noted that the Earth and the lunar pole can only be viewed if the out-of-plane displacement is large enough compared to the radius of the moon. However, these results demonstrate that displaced periodic orbits exist at linear order at all libration points. Due to the high instability of the L_1 and L_2 points of the Earth-Moon system, the next Chapter will be focussed on nonlinear control techniques to the problem of tracking and maintaining the solar sail on prescribed orbits [159, 160, 161]. A simple linear controller was found to generate near constant displacement at the L_4 and L_5 points, since the in-plane motion is passively stable.

Chapter 6

Displaced Periodic Orbits using Low-Thrust Propulsion

The use of solar electric propulsion (SEP) technology is now a realistic option for designing trajectories for interplanetary missions, while solar sail technology is currently under development. The topics covered in this Chapter are the results of displaced periodic orbits in the Earth-Moon system in which the third body uses a hybrid solar sail. The hybrid sail model is composed of two low thrust propulsion systems, namely a solar sail and solar electric propulsion.

Solar sailing and solar electric technology provide alternative forms of spacecraft propulsion. These propulsion systems can enable exciting new space-science mission concepts such as solar system exploration and deep space observation. The aim of this Chapter is to investigate new families of highly non-Keplerian orbits, within the frame of the Earth-Moon circular restricted three-body problem (CRTBP), where the third massless body utilises a hybrid of solar sail and a solar electric thruster. The augmented thrust acceleration is applied to ensure a constant displacement periodic orbit above the L_1 and L_2 Lagrange points, leading to simpler tracking from the lunar surface for communication applications. Using an approximate, first order analytical solution to the nonlinear non-autonomous ordinary differential equations, periodic orbits can be derived that are displaced above/below the plane of the CRTBP.

6.1 System Model

Again m_1 represents the larger primary (Earth), m_2 the smaller primary (Moon) and the motion of the hybrid sail which has a negligible mass will be considered. These two massive bodies (primaries) are assumed to rotate about their common center of mass and the mass of the third body is too small to affect the motion of the two more massive bodies. The system is normalised such that the total mass $(m_1 + m_2)$ is the unit mass, and the unit of length is the distance between the primaries. Thus, the orbital period of the system becomes 2π. The dashed line in Figure 6.1 is a line parallel to the Sun-line direction. The

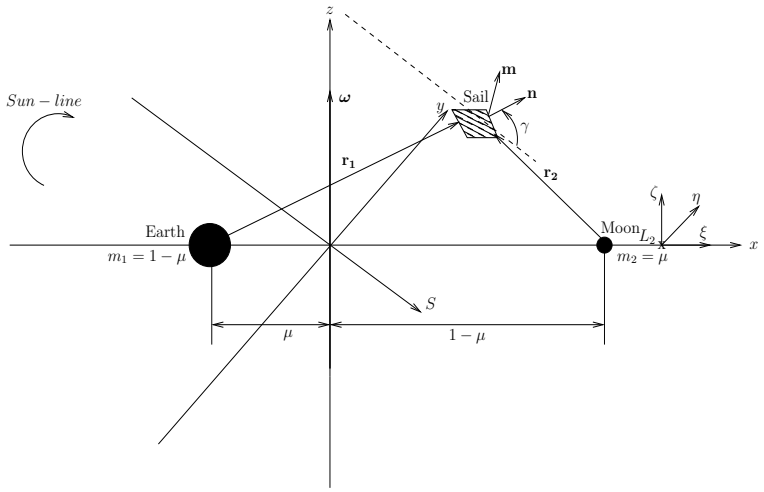

Figure 6.1: Schematic geometry of the Hybrid Sail in the Earth-Moon circular restricted three-body problem.

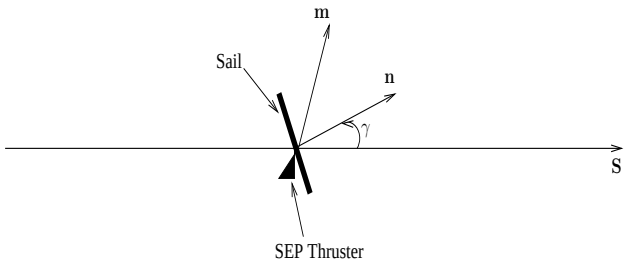

Figure 6.2: Angle γ between the Hybrid Sail surface normal $\boldsymbol{n}$ and the Sun-line direction $\boldsymbol{S}$, and SEP thrust vector direction $\boldsymbol{m}$.

angle γ between the hybrid sail surface normal $\boldsymbol{n}$ and the Sun-line direction $\boldsymbol{S}$ can be seen in Figure 6.2.

6.1.1 Equations of Motions in Presence of the Hybrid Sail

The nondimensional equation of a motion of a hybrid sail in the rotating frame of reference is described by

$$\frac{d^2\boldsymbol{r}}{dt^2} + 2\boldsymbol{\omega} \times \frac{d\boldsymbol{r}}{dt} + \nabla U(\boldsymbol{r}) = \boldsymbol{a}_S + \boldsymbol{a}_{SEP}, \tag{6.1}$$

where $\boldsymbol{\omega} = \omega\hat{\boldsymbol{z}}$ ($\hat{\boldsymbol{z}}$ is a unit vector pointing in the direction $\boldsymbol{z}$) is the angular velocity vector of the rotating frame and $\boldsymbol{r}$ is the position vector of the hybrid sail relative to the center of mass of the two primaries. Again, the small annual changes in the inclination of the Sun-line with respect to the plane of the system will not be considered. The three-body pseudo-potential $U(\boldsymbol{r})$, the solar radiation pressure acceleration $\boldsymbol{a}_S$ and the nondimensional

acceleration due to the SEP thruster $\boldsymbol{a}_{SEP}$ are defined by

$$\begin{aligned} U(\boldsymbol{r}) &= -\left[\frac{1}{2}|\boldsymbol{\omega}\times\boldsymbol{r}|^2+\frac{1-\mu}{r_1}+\frac{\mu}{r_2}\right], \\ \boldsymbol{a}_S &= a_0(\boldsymbol{S}\cdot\boldsymbol{n})^2\boldsymbol{n}, \qquad (6.2) \\ \boldsymbol{a}_{SEP} &= a_{SEP}\boldsymbol{m}, \qquad (6.3) \end{aligned}$$

where μ is the mass ratio for the Earth-Moon system. The hybrid sail position vectors w.r.t. m_1 and m_2 respectively (see Figure 6.1), are defined as $\boldsymbol{r}_1 = [x+\mu, y, z]^T$ and $\boldsymbol{r}_2 = [x-(1-\mu), y, z]^T$, a_0 is the magnitude of the solar radition pressure acceleration exerted on the hybrid sail and the unit vector $\boldsymbol{n}$ denotes the thrust direction, $\boldsymbol{a}_{SEP}$ is the acceleration from the SEP system and the unit vector $\boldsymbol{m}$ denotes the thrust direction. The sail is oriented such that it is always directed along the Sun-line $\boldsymbol{S}$, pitched at an angle γ to provide a constant out-of-plane force. The unit normal to the hybrid sail surface $\boldsymbol{n}$ and the Sun-line direction are given by

$$\begin{aligned} \boldsymbol{n} &= \begin{bmatrix} \cos(\gamma)\cos(\omega_\star t) & -\cos(\gamma)\sin(\omega_\star t) & \sin(\gamma) \end{bmatrix}^T, \qquad (6.4) \\ \boldsymbol{S} &= \begin{bmatrix} \cos(\omega_\star t) & -\sin(\omega_\star t) & 0 \end{bmatrix}^T, \qquad (6.5) \end{aligned}$$

where $\omega_\star$ is the angular rate of the Sun-line in the corotating frame in a dimensionless synodic coordinate system.

6.1.2 Linearised System

The dynamics of the hybrid sail in the neighborhood of the libration points will now be investigated. The coordinates of the equilibrium point are defined as $\boldsymbol{r}_L = (x_{L_i}, y_{L_i}, z_{L_i})^T$ with $i = 1, \cdots, 5$. Let a small displacement in $\boldsymbol{r}_L$ be $\delta\boldsymbol{r}$ such that $\boldsymbol{r} \to \boldsymbol{r}_L + \delta\boldsymbol{r}$. The equations for the hybrid sail can then be written as

$$\frac{d^2\delta\boldsymbol{r}}{dt^2} + 2\boldsymbol{\omega}\times\frac{d\delta\boldsymbol{r}}{dt} + \nabla U(\boldsymbol{r}_L+\delta\boldsymbol{r}) = \boldsymbol{a}_S(\boldsymbol{r}_L+\delta\boldsymbol{r}) + \boldsymbol{a}_{SEP}(\boldsymbol{r}_L+\delta\boldsymbol{r}), \qquad (6.6)$$

and retaining only the first-order term in $\delta\boldsymbol{r} = (\xi, \eta, \zeta)^T$ in a Taylor-series expansion, the gradient of the potential and the acceleration can be expressed as

$$\begin{aligned} \nabla U(\boldsymbol{r}_L+\delta\boldsymbol{r}) &= \nabla U(\boldsymbol{r}_L) + \left.\frac{\partial\nabla U(\boldsymbol{r})}{\partial\boldsymbol{r}}\right|_{\boldsymbol{r}=\boldsymbol{r}_L}\delta\boldsymbol{r} + O(\delta\boldsymbol{r}^2), \qquad (6.7) \\ \boldsymbol{a}_S(\boldsymbol{r}_L+\delta\boldsymbol{r}) &= \boldsymbol{a}_S(\boldsymbol{r}_L) + \left.\frac{\partial\boldsymbol{a}_S(\boldsymbol{r})}{\partial\boldsymbol{r}}\right|_{\boldsymbol{r}=\boldsymbol{r}_L}\delta\boldsymbol{r} + O(\delta\boldsymbol{r}^2). \qquad (6.8) \\ \boldsymbol{a}_{SEP}(\boldsymbol{r}_L+\delta\boldsymbol{r}) &= \boldsymbol{a}_{SEP}(\boldsymbol{r}_L) + \left.\frac{\partial\boldsymbol{a}_{SEP}(\boldsymbol{r})}{\partial\boldsymbol{r}}\right|_{\boldsymbol{r}=\boldsymbol{r}_L}\delta\boldsymbol{r} + O(\delta\boldsymbol{r}^2). \qquad (6.9) \end{aligned}$$

It is assumed that $\nabla U(\boldsymbol{r}_L) = 0$, and the accelerations $\boldsymbol{a}_S$ and $\boldsymbol{a}_{SEP}$ are constant with respect to the small displacement $\delta\boldsymbol{r}$, so that

$$\left.\frac{\partial \boldsymbol{a}_S(\boldsymbol{r})}{\partial \boldsymbol{r}}\right|_{r=r_L} = 0, \tag{6.10}$$

$$\left.\frac{\partial \boldsymbol{a}_{SEP}(\boldsymbol{r})}{\partial \boldsymbol{r}}\right|_{r=r_L} = 0. \tag{6.11}$$

The linear variational system associated with the libration points at $\boldsymbol{r}_L$ can be determined through a Taylor series expansion by substituting Eqs. (6.7) and (6.8) into (6.6) so that

$$\frac{d^2\delta\boldsymbol{r}}{dt^2} + 2\boldsymbol{\omega} \times \frac{d\delta\boldsymbol{r}}{dt} - K\delta\boldsymbol{r} = \boldsymbol{a}_S(\boldsymbol{r}_L) + \boldsymbol{a}_{SEP}(\boldsymbol{r}_L), \tag{6.12}$$

where the matrix K is defined as

$$K = -\left[\left.\frac{\partial \nabla U(\boldsymbol{r})}{\partial \boldsymbol{r}}\right|_{r=r_L}\right]. \tag{6.13}$$

Using matrix notation the linearised equation about the libration point (Equation (6.12)) can be represented by the inhomogeneous linear system $\dot{\mathbf{X}} = A\mathbf{X} + \boldsymbol{b}(t)$, where the state vector $\mathbf{X} = (\delta\boldsymbol{r}, \delta\dot{\boldsymbol{r}})^T$, and for which $\boldsymbol{b}(t)$ (a 6×1 vector) is equal to the sum of control accelerations of the sail and the SEP.

The Jacobian matrix A has the general form

$$A = \begin{pmatrix} 0_3 & I_3 \\ K & \Omega \end{pmatrix}, \tag{6.14}$$

where I_3 is a identity matrix, and

$$\Omega = \begin{pmatrix} 0 & 2 & 0 \\ -2 & 0 & 0 \\ 0 & 0 & 0 \end{pmatrix}. \tag{6.15}$$

Again, the sail attitude is fixed such that the sail normal vector $\boldsymbol{n}$, which is the unit vector that is perpendicular to the sail surface, points always along the direction of the Sun-line with the following constraint $\boldsymbol{S}\cdot\boldsymbol{n} \geq 0$. Its direction is described by the pitch angle γ relative to the Sun-line, which represents the sail attitude. By making the transformation $\boldsymbol{r} \rightarrow \boldsymbol{r}_L + \delta\boldsymbol{r}$ and retaining only the first-order term in $\delta\boldsymbol{r} = (\xi, \eta, \zeta)^T$ in the Taylor-series expansion where (ξ, η, ζ) are axes attached to the libration point as shown in Figure 6.1 (a), the linearised nondimensional equations of motion relative to the collinear libration points can be written as

$$\ddot{\xi} - 2\dot{\eta} - U^o_{xx}\xi = a_\xi + a_{SEP_\xi}, \tag{6.16}$$

$$\ddot{\eta} + 2\dot{\xi} - U^o_{yy}\eta = a_\eta + a_{SEP_\eta}, \tag{6.17}$$

$$\ddot{\zeta} - U^o_{zz}\zeta = a_\zeta + a_{SEP_\zeta}, \tag{6.18}$$

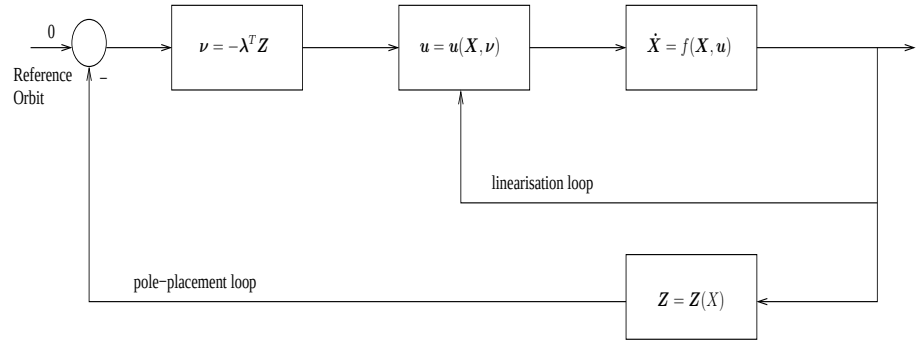

Figure 6.3: Block diagram of feedback linearization.

where U^o_{xx}, U^o_{yy}, and U^o_{zz} are the partial derivatives of the gravitational potential evaluated at the collinear libration points, and the solar sail acceleration is defined in terms of three auxiliary variables a_ξ, a_η, and a_ζ.

The solar sail acceleration components are again given by

$$a_\xi = a_0 \cos(\omega_\star t) \cos^3(\gamma), \tag{6.19}$$
$$a_\eta = -a_0 \sin(\omega_\star t) \cos^3(\gamma), \tag{6.20}$$
$$a_\zeta = a_0 \cos^2(\gamma) \sin(\gamma), \tag{6.21}$$

where a_0 is the characteristic acceleration. The SEP acceleration components $\boldsymbol{a}_{SEP}$ are used for feedback control as described later.

6.2 Tracking by Feedback Linearisation

6.2.1 Description

Linearisation by feedback is a well-known approach to control nonlinear systems. This method transforms a nonlinear state space model into a new coordinate system where the nonlinearities can be cancelled by feedback. It is a way of transforming system models into equivalent models of simpler form. For example, a change of variables $\boldsymbol{Z} = \Phi(\boldsymbol{X})$ is used to transform the state equation from the $\boldsymbol{X}$-coordinates to the $\boldsymbol{Z}$-coordinates, where the map $\Phi(.)$ must be invertible, such that $\boldsymbol{X} = \Phi^{-1}(\boldsymbol{Z})$ for $\boldsymbol{Z} \in \Phi(D)$ where D is the domain of Φ. Furthermore, the derivatives of $\boldsymbol{X}$ and $\boldsymbol{Z}$ should be continous and therefore the map Φ and its inverse $\Phi^{-1}(.)$ are continously differentiable. Such a map is a diffeomorphism and can be viewed as a generalization of the coordinate transformation. In order to understand this approach, a formal definition is necessary.

Definition 1. *A nonlinear system*

$$\dot{\boldsymbol{X}} = f(\boldsymbol{X}, \boldsymbol{u}) \tag{6.22}$$

where $f : D \to \mathbb{R}^n$ is sufficiently smooth on a domain $D \subset \mathbb{R}^n$ is said to be feedback linearisable (or input-state linearisable) if there exits a diffeomorphism $\Phi : D \to \mathbb{R}^n$, and a nonlinear feedback control law $\boldsymbol{u} = (\boldsymbol{X}, \boldsymbol{\nu})$ such that the new state variables

$$\boldsymbol{Z} = \Phi(\boldsymbol{X}) \tag{6.23}$$

and the new control input $\boldsymbol{\nu}$ satisfy a linear time-invariant relation

$$\dot{\boldsymbol{Z}} = A\boldsymbol{Z} + B\boldsymbol{\nu} \tag{6.24}$$

where the pair (A, B) is completely controllable.

6.2.2 Objectives

Given the nonlinear system of equation (6.22), the problem of feedback linearisation consists of finding, if possible, a change of coordinates of the form of equation (6.23) and a static state feedback control $\boldsymbol{u} = (\boldsymbol{X}, \boldsymbol{\nu})$, such that the new control input $\boldsymbol{\nu}$ satisfies a linear time-invariant relation $\dot{\boldsymbol{Z}} = A\boldsymbol{Z} + B\boldsymbol{\nu}$ where the pair (A, B) is controllable. This technique is completely different from a Jacobian linearisation, on which linear control is based. The block diagram of the feedback linearisation is depicted in Figure 6.3.

From equation (6.1) the motion of the hybrid solar sail in the CRTBP is described by the scalar equations in the form

$$\ddot{\xi} = 2\dot{\eta} + (x_{L_2} + \xi) - (1-\mu)\frac{(x_{L_2} + \xi) + \mu}{r_1^3} - \mu\frac{(x_{L_2} + \xi) - 1 + \mu}{r_2^3} + a_\xi + u_\xi, \tag{6.25}$$

$$\ddot{\eta} = -2\dot{\xi} + \eta - \left(\frac{1-\mu}{r_1^3} + \frac{\mu}{r_2^3}\right)\eta + a_\eta + u_\eta, \tag{6.26}$$

$$\ddot{\zeta} = -\left(\frac{1-\mu}{r_1^3} + \frac{\mu}{r_2^3}\right)\zeta + a_\zeta + u_\zeta, \tag{6.27}$$

where the vector

$$\boldsymbol{u}(t) = \begin{bmatrix} u_\xi & u_\eta & u_\zeta \end{bmatrix}^T \tag{6.28}$$

is the applied control acceleration due to the SEP thruster, such that $\boldsymbol{u}(t) \triangleq \boldsymbol{a}_{SEP}$.

To develop a feedback linearisation scheme, the motion of the hybrid solar sail moving in the CRTBP is separated into linear and nonlinear components, such that

$$\ddot{\xi} = f^{\xi}_{Non-Linear} + f^{\xi}_{Linear} + a_\xi + u_\xi, \tag{6.29}$$

$$\ddot{\eta} = f^{\eta}_{Non-Linear} + f^{\eta}_{Linear} + a_\eta + u_\eta, \tag{6.30}$$

$$\ddot{\zeta} = f^{\zeta}_{Non-Linear} + f^{\zeta}_{Linear} + a_\zeta + u_\zeta, \tag{6.31}$$

where the f functions are defined as the linear and the nonlinear terms in the equations (6.25), (6.26) and (6.27)

$$
\begin{aligned}
f^{\xi}_{Non-Linear} &= -(1-\mu)\frac{(x_{L_2}+\xi)+\mu}{r_1^3} - \mu\frac{(x_{L_2}+\xi)-1+\mu}{r_2^3}, && (6.32)\\
f^{\xi}_{Linear} &= 2\dot{\eta} + (x_{L_2}+\xi), && (6.33)\\
f^{\eta}_{Non-Linear} &= -\left(\frac{1-\mu}{r_1^3} + \frac{\mu}{r_2^3}\right)\eta, && (6.34)\\
f^{\eta}_{Linear} &= -2\dot{\eta} + (x_{L_2}+\xi), && (6.35)\\
f^{\zeta}_{Non-Linear} &= -\left(\frac{1-\mu}{r_1^3} + \frac{\mu}{r_2^3}\right)\zeta, && (6.36)\\
f^{\zeta}_{Linear} &= 0, && (6.37)
\end{aligned}
$$

with $r_1 = \sqrt{((x_{L_2}+\xi)+\mu)^2+\eta^2+\zeta^2}$ *and* $r_2 = \sqrt{((x_{L_2}+\xi)-1+\mu)^2+\eta^2+\zeta^2}$.

The solar sail acceleration components are given in equations (6.19), (6.20) and (6.21). The SEP control $\boldsymbol{u}(t)$ is then selected such that

$$
\boldsymbol{u}(t) = \begin{bmatrix} u_\xi \\ u_\eta \\ u_\zeta \end{bmatrix} = \boldsymbol{U}(t) + \tilde{\boldsymbol{u}}(t), \tag{6.38}
$$

where

$$
\boldsymbol{U}(t) = -\begin{bmatrix} (x_{L_2}+\xi) - (1-\mu)\frac{(x_{L_2}+\xi)+\mu}{r_1^3} - \mu\frac{(x_{L_2}+\xi)-1+\mu}{r_2^3} - U^o_{xx}\xi \\ -\left(\frac{1-\mu}{r_1^3} + \frac{\mu}{r_2^3}\right)\eta - U^o_{yy}\eta \\ -\left(\frac{1-\mu}{r_1^3} + \frac{\mu}{r_2^3}\right)\zeta - U^o_{zz}\zeta \end{bmatrix} \tag{6.39}
$$

is the canceling term and $\tilde{\boldsymbol{u}}(t)$ the stabilising term.

The equations (6.25), (6.26) and (6.27) then become

$$
\begin{aligned}
\ddot{\xi} &= 2\dot{\eta} + U^o_{xx}\xi + a_0\cos(\omega_\star t)\cos^3(\gamma) + \tilde{u}_\xi, && (6.40)\\
\ddot{\eta} &= -2\dot{\xi} + U^o_{yy}\eta - a_0\sin(\omega_\star t)\cos^3(\gamma) + \tilde{u}_\eta, && (6.41)\\
\ddot{\zeta} &= U^o_{zz}\zeta + a_0\cos^2(\gamma)\sin(\gamma) + \tilde{u}_\zeta. && (6.42)
\end{aligned}
$$

By removing the nonlinear dynamics from the system, the control acceleration vector $\tilde{\boldsymbol{u}}(t)$ is determined such that the desired response characteristics of the linear time-invariant dynamics are produced and so Eq. (6.40) - (6.42) are identical to the linear system defined by Eq. (6.16) - (6.18). In particular, it can be ensured that the displacement distance of the periodic orbit is constant, which provides key advantages for lunar polar telecommunications.

6.3 Tracking a Reference Trajectory

After transforming the nonlinear dynamics into a linear form, one can easily design controllers for either stabilisation or tracking purposes.

6.3.1 Linear Feedback Control

Let us consider the nonlinear system described by

$$\ddot{\boldsymbol{x}} = f(\boldsymbol{x}, \dot{\boldsymbol{x}}) + \boldsymbol{u}, \tag{6.43}$$

where $\boldsymbol{x} \in \mathbb{R}^3$ is the position. Let $\boldsymbol{e}(t) = \boldsymbol{x}(t) - \boldsymbol{x}_{ref}(t)$ denote the position error relative to some reference solution, where the reference trajectory

$$\boldsymbol{x}_{ref}(t) = \left[\begin{array}{ccc} \xi_{ref} & \eta_{ref} & \zeta_{ref} \end{array} \right]^T \tag{6.44}$$

is given by the analytical solution

$$\begin{aligned} \xi_{ref}(t) &= \xi_0 \cos(\omega_\star t), & (6.45)\\ \eta_{ref}(t) &= \eta_0 \sin(\omega_\star t), & (6.46)\\ \zeta_{ref}(t) &= \zeta_0. & (6.47) \end{aligned}$$

The term $\boldsymbol{e}(t)$ is then differentiated until the control appears so that

$$\begin{aligned} \boldsymbol{e}(t) &= \boldsymbol{x}(t) - \boldsymbol{x}_{ref}(t), & (6.48)\\ \dot{\boldsymbol{e}}(t) &= \dot{\boldsymbol{x}}(t) - \dot{\boldsymbol{x}}_{ref}(t), & (6.49)\\ \ddot{\boldsymbol{e}}(t) &= \ddot{\boldsymbol{x}}(t) - \ddot{\boldsymbol{x}}_{ref}(t), & \\ &= f(\boldsymbol{x}, \dot{\boldsymbol{x}}) + \boldsymbol{u} - \ddot{\boldsymbol{x}}_{ref}(t), & \\ &= -\lambda_1 \dot{\boldsymbol{e}} - \lambda_2 \boldsymbol{e}, & (6.50) \end{aligned}$$

and so

$$\boldsymbol{u}(t) = -f(\boldsymbol{x}, \dot{\boldsymbol{x}}) + \ddot{\boldsymbol{x}}_{ref}(t) - \lambda_1 \dot{\boldsymbol{e}} - \lambda_2 \boldsymbol{e}, \tag{6.51}$$

where

$$f = \left[\begin{array}{c} f^{\xi}_{Non-Linear} \\ f^{\eta}_{Non-Linear} \\ f^{\zeta}_{Non-Linear} \end{array} \right] \tag{6.52}$$

and $-\lambda_1 \dot{\boldsymbol{e}} - \lambda_2 \boldsymbol{e}$ is the stabilising term.

6.3.2 Trajectory Tracking

Consider the system given by equation (6.43), where our objective is to make the output $\boldsymbol{x} \in \mathbb{R}^3$ track a desired trajectory given by the reference trajectory $\boldsymbol{x}_{ref} \in \mathbb{R}^3$ while keeping the position bounded. Therefore, a control law for the input $\tilde{\boldsymbol{u}} \in \mathbb{R}^3$ will be

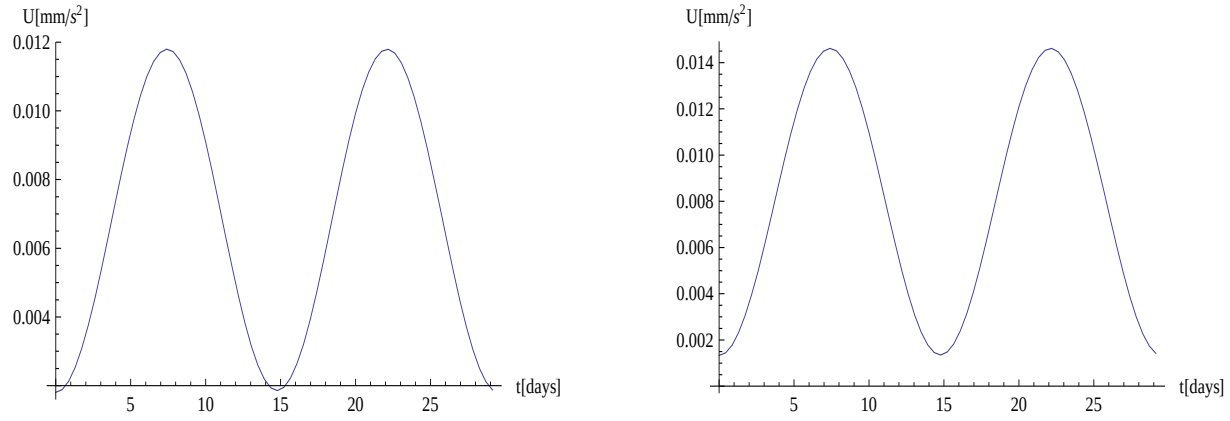

Figure 6.4: (a) Magnitude of the total control effort about the L_1 point; (b) Magnitude of the total control effort about the L_2 point.

found, such that starting from any initial position in a domain $D \subset \mathbb{R}^3$, the tracking error $\boldsymbol{e}(t) = \boldsymbol{x}(t) - \boldsymbol{x}_{ref}(t)$ goes to zero. Hence, asymptotic tracking will be achieved if a state feedback control law is designed to ensure that $\boldsymbol{e}(t)$ is bounded and converges to zero as t tends to infinity. Thus, the control law

$$\tilde{\boldsymbol{u}} = -\lambda_1 \dot{\boldsymbol{e}} - \lambda_2 \boldsymbol{e} \tag{6.53}$$

yields the tracking error equation

$$\ddot{\boldsymbol{e}} + \lambda_1 \dot{\boldsymbol{e}} + \lambda_2 \boldsymbol{e} = 0, \tag{6.54}$$

where λ_1 and λ_2 are chosen positive constants.

6.4 Evaluation of Hybrid Sail Performance

6.4.1 Evaluation

Let us investigate the performance of a hybrid sail system, constituted by a solar sail combined with solar electric propulsion. A minimum displacement distance of 1750 km has been considered for the simulations, as given in Table 6.1. This allows the spacecraft to view both the lunar pole and the Earth for communication applications. The simulation was performed around the collinear libration points for a period of one month. The magnitude of the total control effort appears in Figure 6.4. Thus, the control acceleration effort $\boldsymbol{U}(t)$ required to track the reference orbit while rejecting the nonlinearities varies up to 0.004 (0.012 mm/s^2) for the orbit about L_1 and 0.005 (0.014 mm/s^2) for the orbit about the L_2 point. The control accelerations are continous smooth signals. The acceleration derived from the solar sail (denoted by a_ξ, a_η, a_ζ) is plotted in terms of components for

Table 6.1: Parameters of reference trajectory.

	$\xi_0[km]$	$\eta_0[km]$	$\zeta_0[km]$	$a_0[mms^{-2}]$
L_1	-422.849	-4108.13	1750	0.16
L_2	282.613	-5525.23	1750	0.10

one-month orbits in Figure 6.5 (a) about L_1, Figure 6.7 (a) about L_2, and the SEP acceleration components appears in Figure 6.5 (b) about L_1, Figure 6.7 (b) about L_2. The control acceleration effort derived from the thruster (denoted by U_ξ, U_η, U_ζ) is order of 10^{-3} - 10^{-4}, while the acceleration derived from the solar sail is approximately 10^{-2}. The small control acceleration from the SEP thruster is then applied to ensure that the displacement of the periodic orbit is constant. The solar sail provides a constant out-of-plane force. Figure 6.6 (critically damped motion) illustrates the position error components with $\boldsymbol{e}(0) = (-42.28, -410.81, 175)^T\ km$, denoted by e_ξ, e_η, e_ζ and the velocity error components, denoted by $e_{\xi d}, e_{\eta d}, e_{\zeta d}$, under the nonlinear control and the SEP thruster around L_1. Figure 6.8 (critically damped motion) shows the corresponding errors in the position with $\boldsymbol{e}(0) = (28.26, -552.52, 175)^T\ km$ and velocity components around L_2.

These figures show that the motion is bounded and periodic. This observation implies that the augmented thrust acceleration ensures a constant displacement orbit. The orbit resulting from tracking the reference orbit using the nonlinear control and the SEP thruster around L_1 are also depicted in Figure 6.9 (a) and Figure 6.9 (b) for the orbit around L_2 point.

The parameters of the reference trajectory used for the simulations are summarised in Table 6.1. A sample of results for a constant displacement distance of 2500 km can be found in Appendix B Section B.1.

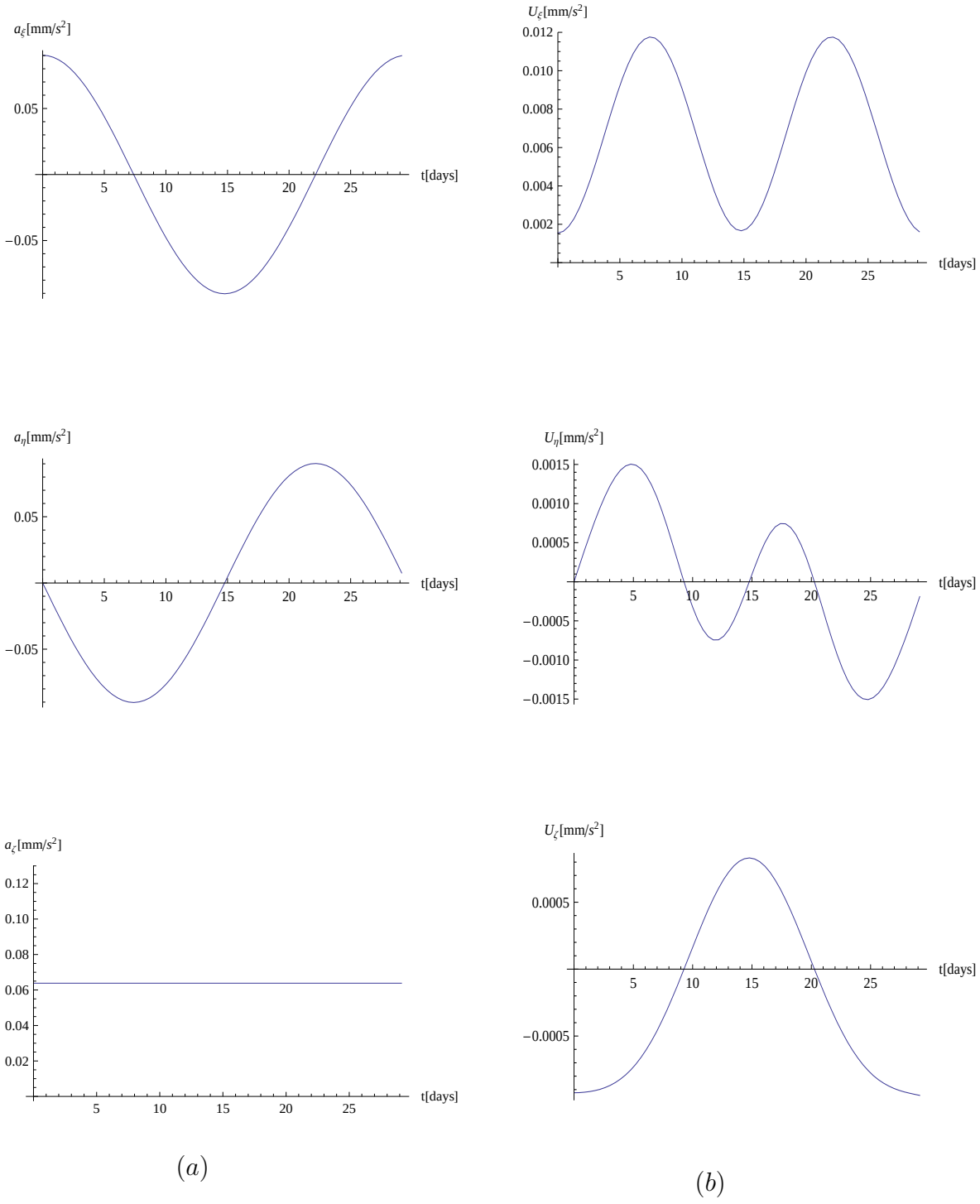

(a) (b)

Figure 6.5: (a) Acceleration derived from the solar sail about the L_1 point; (b) Acceleration derived from the thruster about the L_1 point.

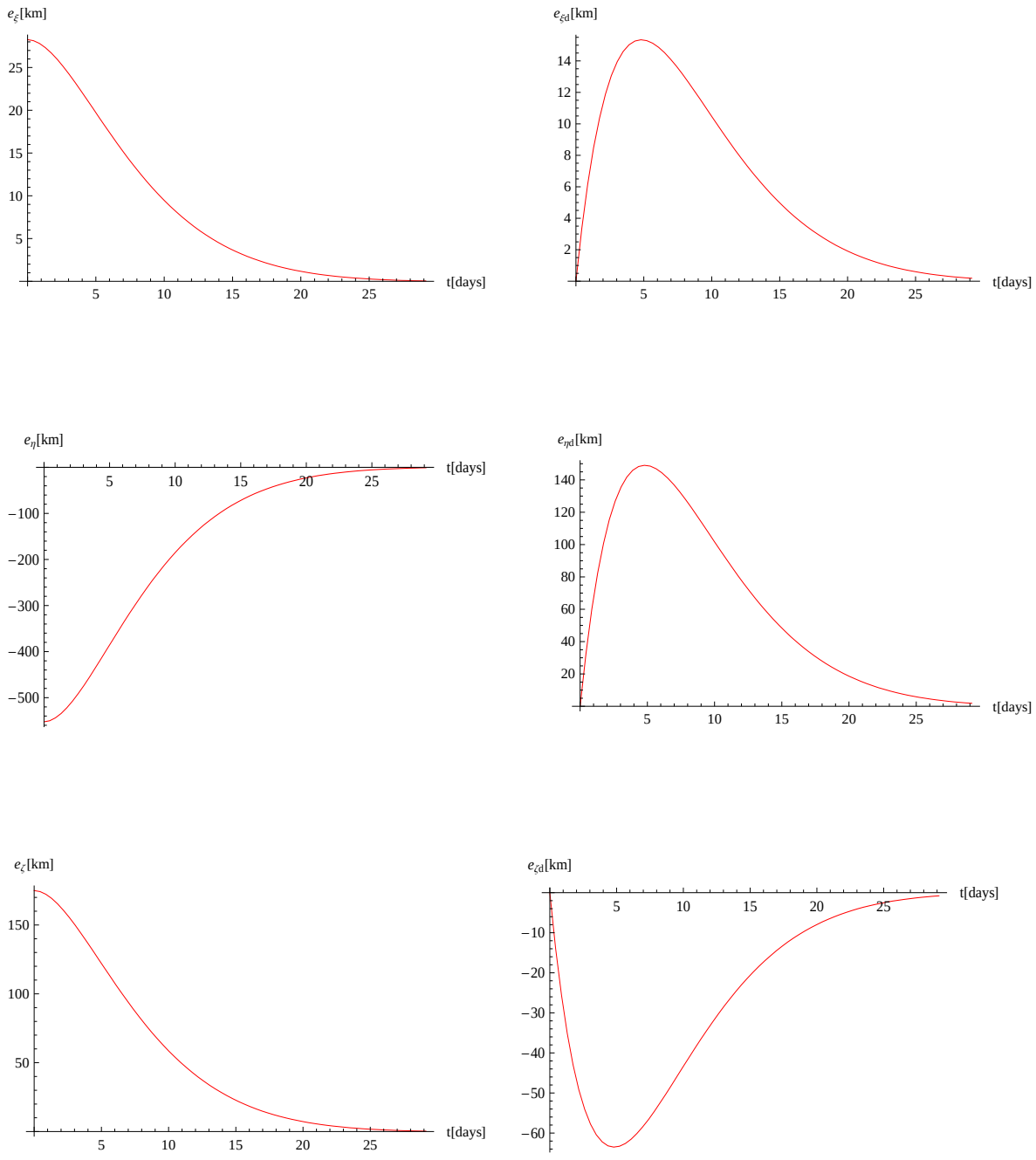

(a) (b)

Figure 6.6: (a) Position error components about the L_1 point; (b) Velocity Error components about the L_1 point.

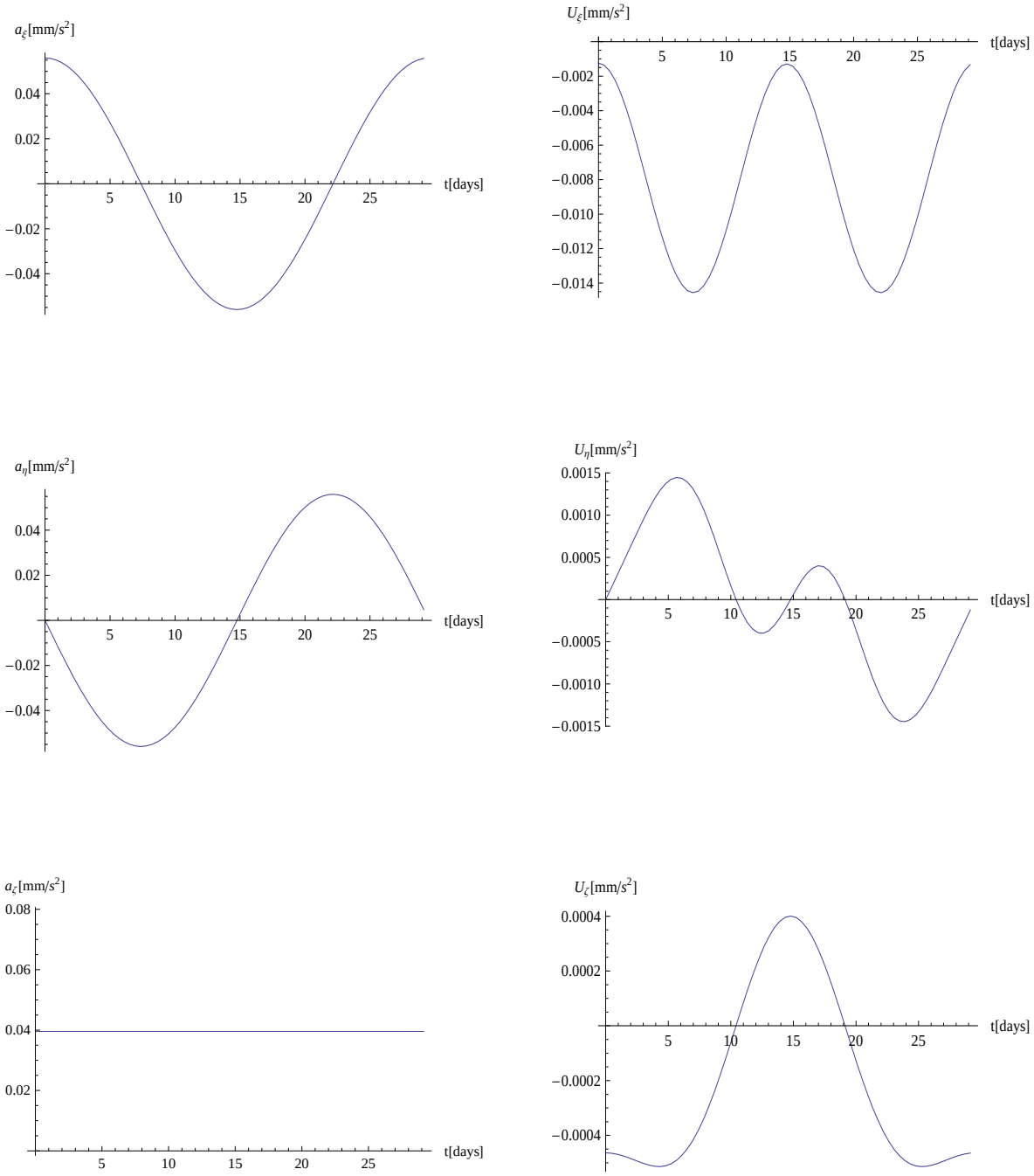

(a) (b)

Figure 6.7: (a) Acceleration derived from the solar sail about the L_2 point; (b) Acceleration derived from the SEP thruster about the L_2 point.

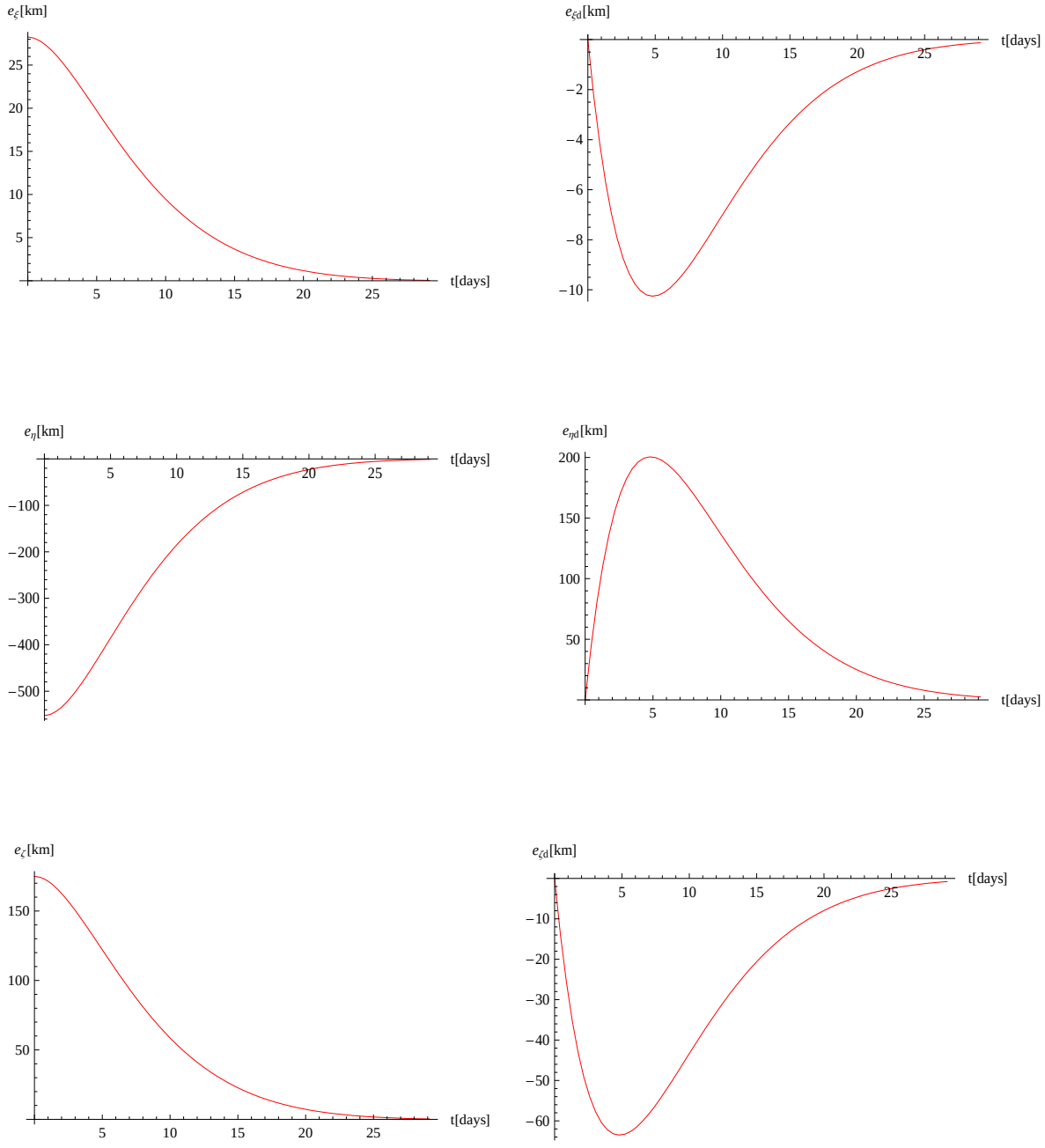

(a) (b)

Figure 6.8: (a) Position error components about the L_2 point; (b) Velocity Error components about the L_2 point.

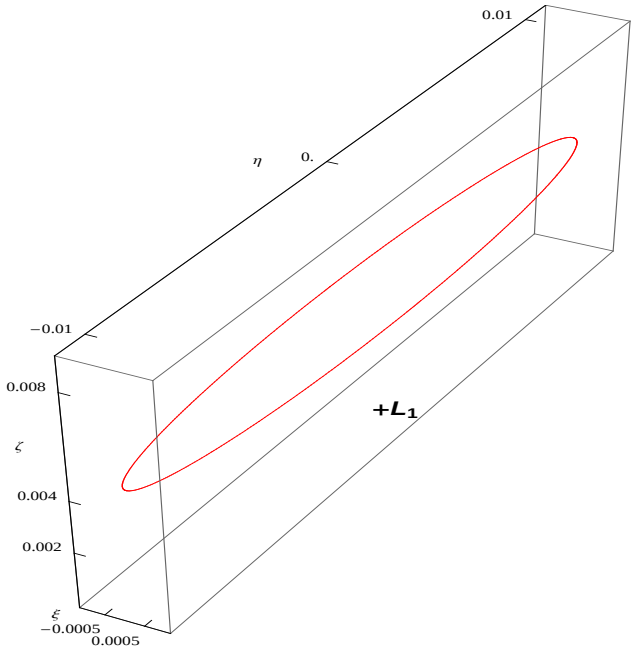

(a)

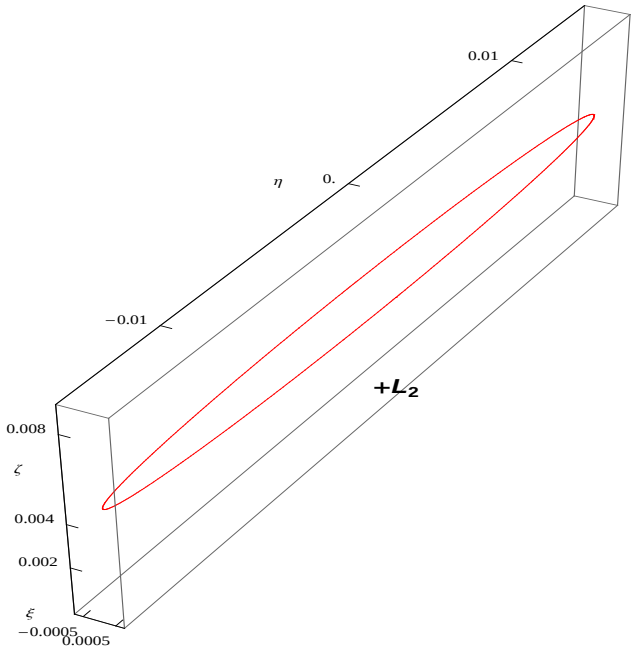

(b)

Figure 6.9: Orbit resulting from tracking the reference orbit using the nonlinear control and SEP thruster: (*a*) Above L_1; (*b*) Above L_2.

6.4.2 Propellant Usage

Propellant usage for the SEP thruster is proportional to the total ΔV, which is the integration over time of the magnitude of the control acceleration produced by using the SEP thruster so that

$$\Delta V = \int_0^{2\pi/\omega_\star} |\boldsymbol{u}| dt. \tag{6.55}$$

The total ΔV_{Total} over a 5 year mission is given by

$$\Delta V_{Total} = \Delta V per\ orbit \times no, \tag{6.56}$$

where no is the total number of orbits. Once the total ΔV is computed, the propellant usage can be found using the rocket equation.

Let us define the mass m of the rocket at a time t, as a function of the initial mass m_i, ΔV and the effective exhaust velocity $v_e = I_{sp} \cdot g$,

$$m = m_i e^{-\Delta V/g \cdot I_{sp}}. \tag{6.57}$$

The mass of propellant is then the difference between the initial and the final masses

$$m_{prop} = m_i - m = m_i(1 - e^{-\Delta V_{Total}/g \cdot I_{sp}}), \tag{6.58}$$

where I_{sp} is the specific impulse ($\approx 3000\ sec$ for an electric thruster).

Assume a specific impulse of $I_{sp} = 3000\ sec$ and an initial mass of $m_i = 500\ kg$, it is obtained from equation (6.55) the average ΔV per orbit of approximately 23 m/s. Then, the total ΔV per orbit over 5 years is 1536 m/s. The consumed propellant mass is then $m_{prop} = 25\ kg$. The parameters are summarized in Table 6.2.

Table 6.2: Summary of Parameters.

Parameter	*Description*	*Value*
$m_i\ (kg)$	Initial Mass	500
$I_{sp}\ (sec)$	Specific Impulse	3000
$\Delta V_{Total}\ (m/s)$	Total ΔV over 5 years	1536
$m_{prop}(kg)$	Propellant Mass Consummed (kg)	25

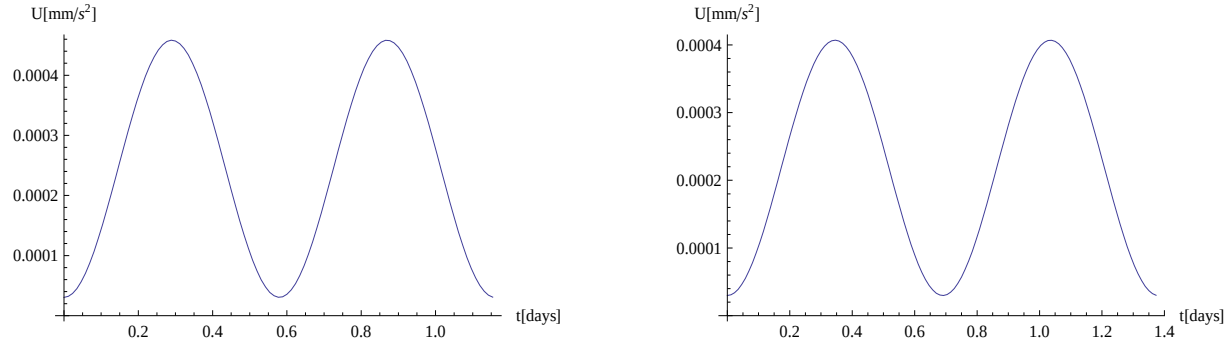

Figure 6.10: (a) Magnitude of the total control effort, $\mu = 0.25$; (b) Magnitude of the total control effort, $\mu = 0.5$.

6.5 Applications to Binary Asteroid Systems

Using the Earth-Moon System as the primaries previously in the circular restricted three-body problem, a hybrid concept for displaced lunar orbits has been developed. Attention is now directed to binary asteroid systems in this section as an application of the restricted problem. Thus, several set of curves of the control acceleration effort required to track a reference orbit while rejecting the nonlinearities are shown from $\mu = 0.15$ to $\mu = 0.5$.

The magnitude of the total control effort appears in Figure 6.10 (a) for system mass ratio $\mu = 0.25$, and Figure 6.10 (b) for $\mu = 0.5$. The control acceleration effort $\boldsymbol{U}(t)$ required to track the reference orbit while rejecting the nonlinearities varies up to 0.0008 mm/s^2 for $\mu = 0.25$ and 0.0010 mm/s^2 for $\mu = 0.5$. Again, the control accelerations are continous smooth signals. The acceleration derived from the solar sail (denoted by a_ξ, a_η, a_ζ) is plotted in terms of components for one revolution of the asteroid orbit in Figure 6.11 (a), and the SEP acceleration components appears in Figure 6.11 (b) for system mass ratio $\mu = 0.25$. Similarly, the acceleration derived from the solar sail is plotted in terms of components for one revolution of the asteroid orbit in Figure 6.12 (a), and the SEP acceleration components appears in Figure 6.12 (b) for system mass ratio $\mu = 0.5$. The control acceleration effort derived from the thruster (denoted by U_ξ, U_η, U_ζ) is order of 10^{-4} - 10^{-5}, while the acceleration derived from the solar sail is approximately 10^{-2} for $\mu = 0.25$ and $\mu = 0.5$.

The numerical results indicate that these conclusions might be extended up to $\mu = 0.5$ (see Appendix B Section B.2 for other cases and further simulations). The practical importance of such trajectories is due to the fact that the sensitivity to errors in guidance is small.

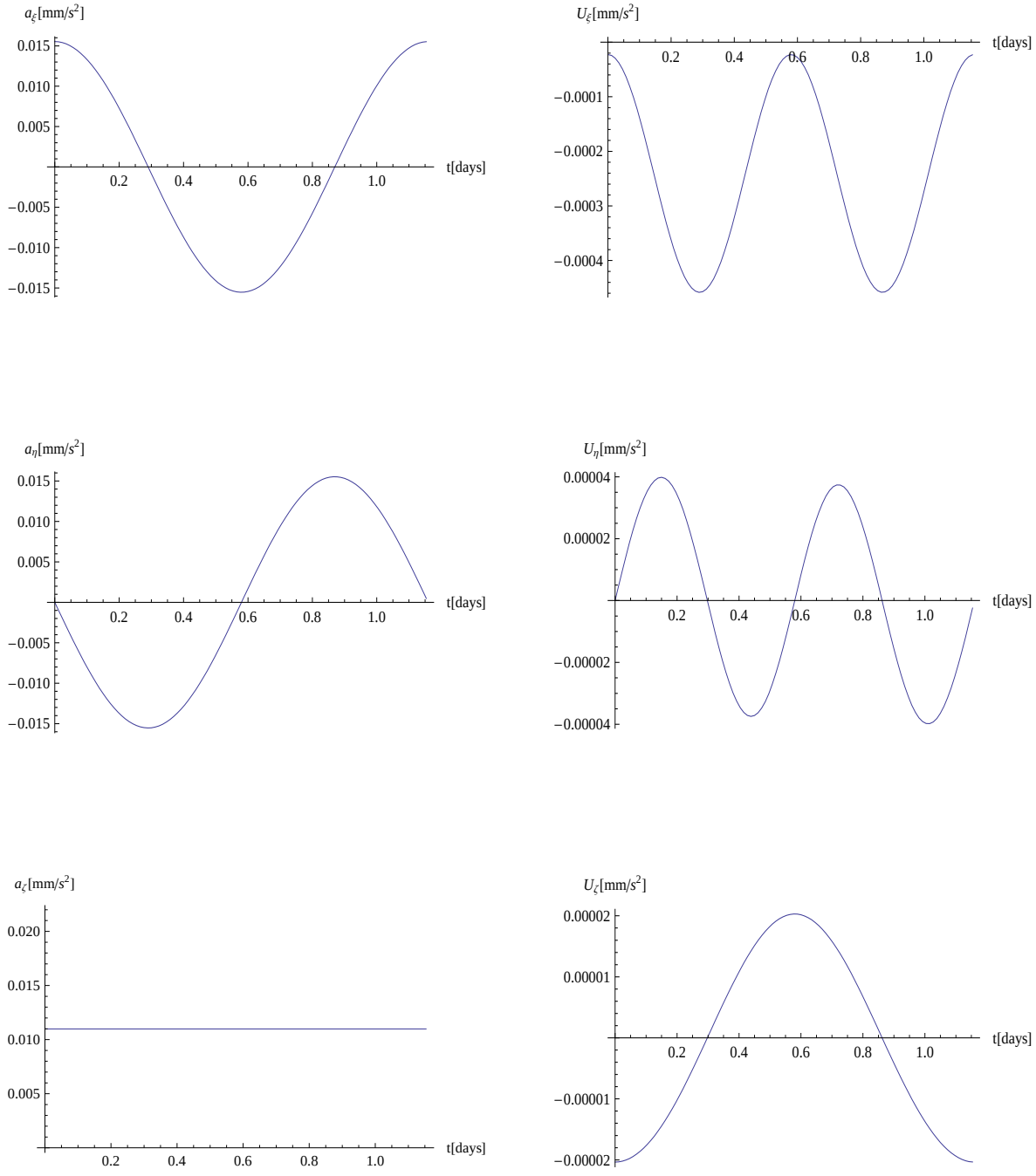

Figure 6.11: (a) Acceleration derived from the solar sail with the system mass ratio $\mu = 0.25$; (b) Acceleration derived from the SEP thruster with the system mass ratio $\mu = 0.25$.

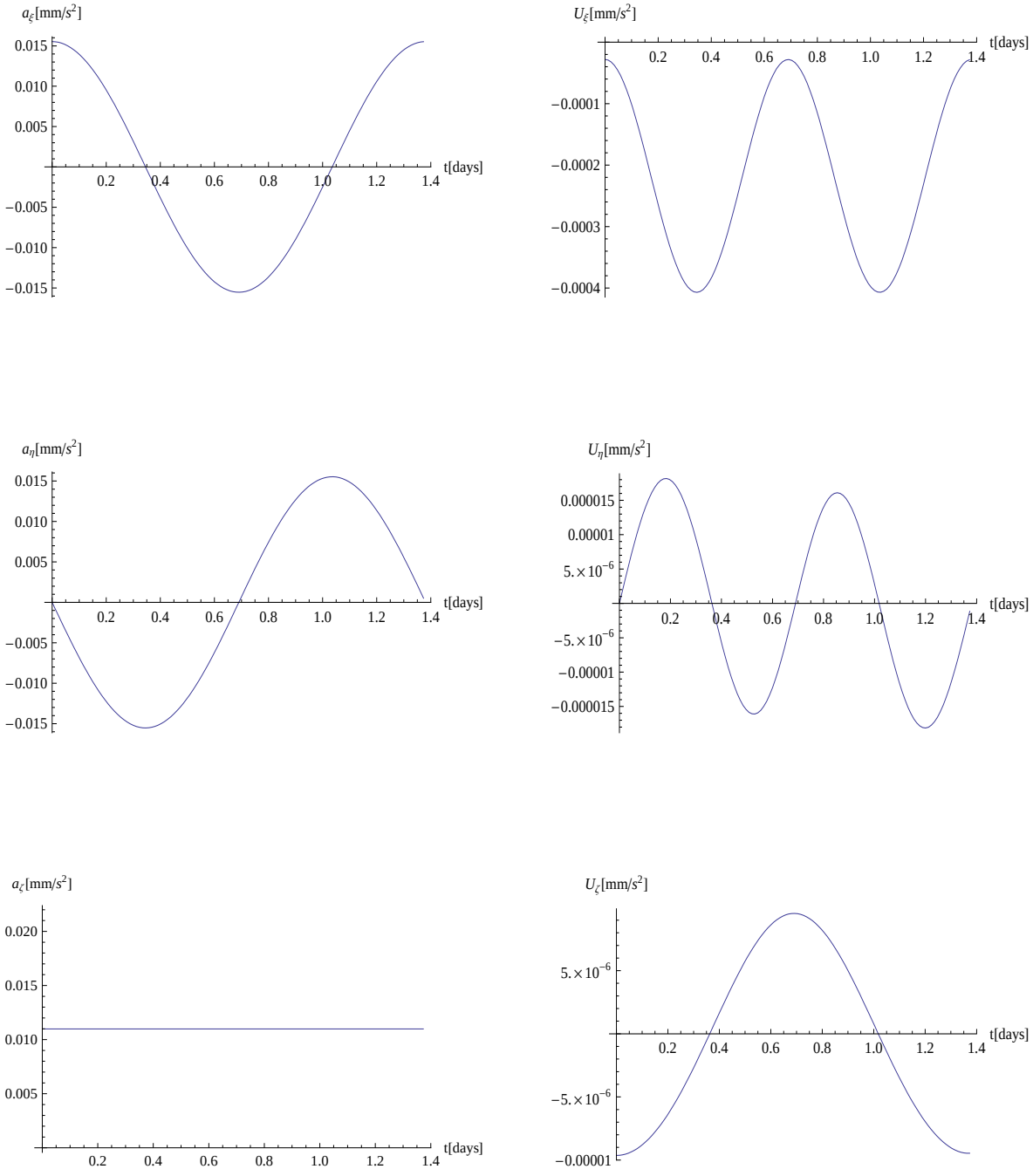

(*a*) (*b*)

Figure 6.12: (*a*) Acceleration derived from the solar sail with the system mass ratio $\mu = 0.5$; (*b*) Acceleration derived from the SEP thruster with the system mass ratio $\mu = 0.5$.

6.6 Artificial Equilibria

A brief discussion is presented for equilibrium solutions in the rotating frame of reference, while a somewhat more eleborate discussion is presented in Chapter 7 on the dynamics of displaced orbits in the Earth-Moon circular restricted three-body problem that are of special interest in connection to an approximate two-body Earth-Moon problem with a constant radiation pressure.

Recall from Chapter 5 that the nondimensional equation of a motion of a spacecraft in the rotating frame of reference is described by

$$\frac{d^2\boldsymbol{r}}{dt^2} + 2\boldsymbol{\omega} \times \frac{d\boldsymbol{r}}{dt} + \nabla U(\boldsymbol{r}) = \boldsymbol{a}, \tag{6.59}$$

where $\boldsymbol{\omega} = \omega\hat{\boldsymbol{z}}$ ($\hat{\boldsymbol{z}}$ is a unit vector pointing in the direction $\boldsymbol{z}$) is the angular velocity vector of the rotating frame, $\boldsymbol{r}$ is the position vector of the sail relative to the center of mass of the two primaries, $\boldsymbol{a}$ is the thrust-induced acceleration and the three-body pseudo-potential $U(\boldsymbol{r})$ is defined by

$$U(\boldsymbol{r}) = -\left[\frac{1}{2}|\boldsymbol{\omega} \times \boldsymbol{r}|^2 + \frac{1-\mu}{r_1} + \frac{\mu}{r_2}\right].$$

Thus, if a spacecraft remains stationary with respect to the rotating frame so that $\boldsymbol{a} = \nabla U(\boldsymbol{r})$, the magnitude of the required thrust-induced acceleration is given simply by

$$a = ||\nabla U(\boldsymbol{r})||. \tag{6.60}$$

In accordance with these conditions, the reduced equation (6.60) may now be used to form an equilibrium solution to the equations of motion in the rotating frame of reference. With the value of $||\nabla U(\boldsymbol{r})||$, the derived acceleration will remain stationary at a given spatial location in the $x - z$ projection. Figure 6.13 shows the contour plot of $||\nabla U(\boldsymbol{r})||$, that apprximates the required acceleration values at a given point in space for feasible trajectories.

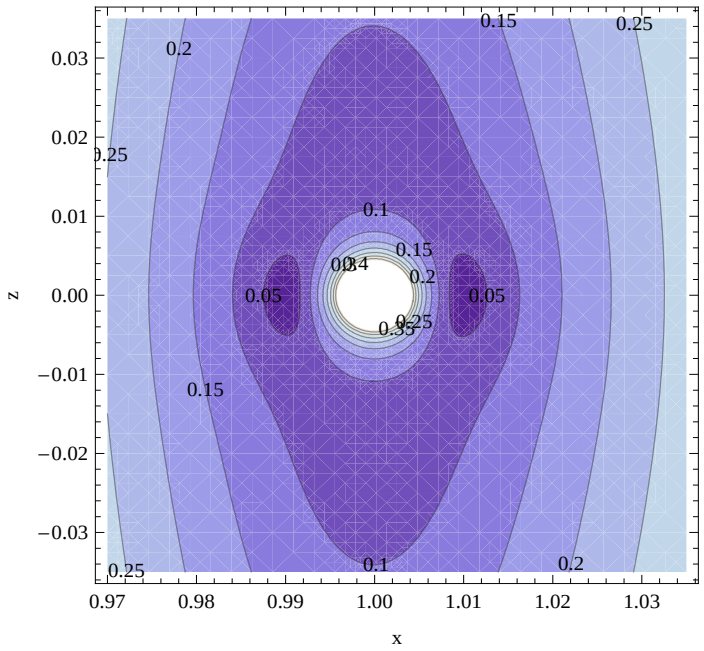

Figure 6.13: A contour plot of the derived acceleration (in mms^{-2}).

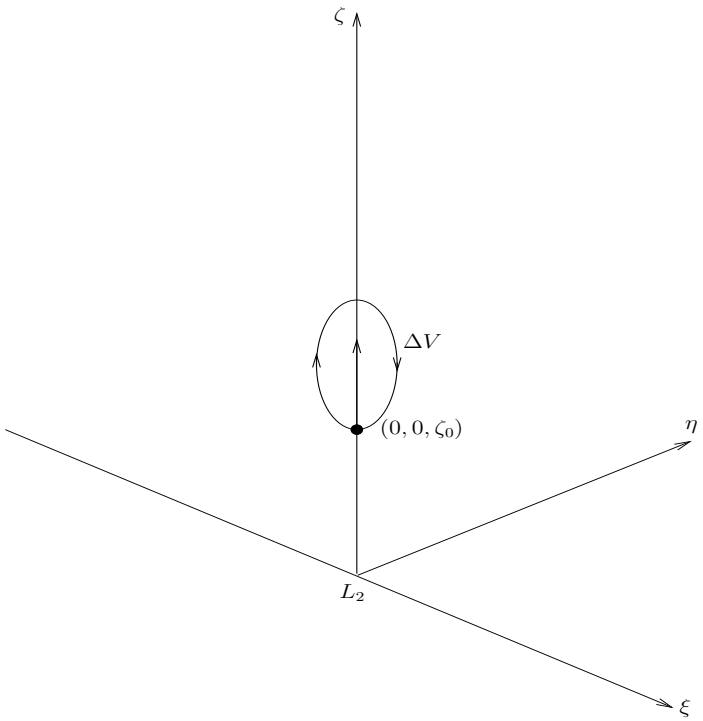

Figure 6.14: Orbit reference frame for impulse control (Out-of-plane maneuvers).

6.7 Impulse control

The displaced orbits investigated in the previous sections may also be generated using impulse control. The out-of-plane displacement is then achieved by repeatedly reversing the vertical component of the spacecraft velocity in a periodic manner. In order to compare the continuous thrust and impulse control orbits, linearised equations of motion will now be considered for small displacements, as shown in Figure 6.14. The representation of this technique can be seen in Figure 6.15. As presented in Chapter 4 Section 4.1, the nondimensional linearised equations of motion near the collinear libration points are given by

$$\ddot{\xi} - 2\dot{\eta} - U^o_{xx}\xi = a_\xi, \tag{6.61}$$

$$\ddot{\eta} + 2\dot{\xi} - U^o_{yy}\eta = a_\eta, \tag{6.62}$$

$$\ddot{\zeta} - U^o_{zz}\zeta = a_\zeta, \tag{6.63}$$

where U^o_{xx}, U^o_{yy}, and U^o_{zz} are the partial derivatives of the gravitational potential evaluated at the collinear libration points.

For continuous thrust, the required acceleration components for displaced artificial equilibrium solutions may be obtained from Eqs. ((6.61)-(6.63)) as

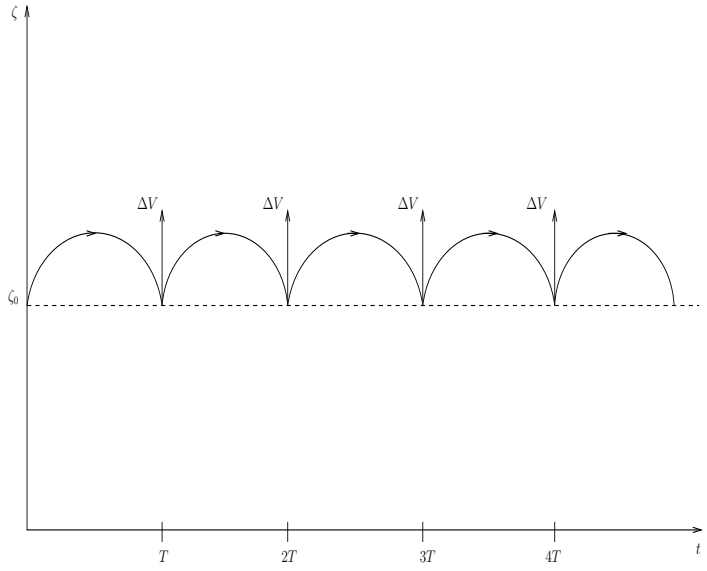

Figure 6.15: Impulse control scheme.

$$\begin{aligned} a_\xi &= -U^o_{xx}\xi, \\ a_\eta &= -U^o_{yy}\eta, \\ a_\zeta &= -U^o_{zz}\zeta. \end{aligned}$$

6.7.1 Out-of-plane Maneuvers

In order to maintain an out-of-plane displacement, repeated vertical impulses are required such that $\zeta(0) = \zeta(T) = \zeta_0$, where T is the period between impulses. By making use of the equation (4.26) in Chapter 4 and Section 4.1, it is found that

$$\cos(\omega_\zeta T) + \frac{\dot{\zeta}_0}{\omega_\zeta \zeta_0}\sin(\omega_\zeta T) = 1, \tag{6.64}$$

$$\frac{\dot{\zeta}_0}{\omega_\zeta \zeta_0} = \frac{1-\cos(\omega_\zeta T)}{\sin(\omega_\zeta T)}, \tag{6.65}$$

$$\dot{\zeta}_0 = \omega_\zeta \zeta_0 \left[\frac{1-\cos(\omega_\zeta T)}{\sin(\omega_\zeta T)}\right]. \tag{6.66}$$

Thus, the required initial out-of-plane velocity reduces to

$$\dot{\zeta}_0 = \omega_\zeta \zeta_0 \tan\left[\frac{\omega_\zeta T}{2}\right]. \tag{6.67}$$

There is an important symmetry in these equations of motion given by $\dot{\zeta}(T) = -\dot{\zeta}(0)$. This symmetry can thus be exploited, in a standard way, to obtain the effective out-of-plane acceleration $\bar{a}_\zeta$ by the repeated impulses. More explicitly

$$\bar{a}_\zeta \approx \frac{\Delta V_\zeta}{T} = \frac{2\dot{\zeta}_0}{T}, \tag{6.68}$$

and

$$\bar{a}_\zeta = \frac{2\omega_\zeta \zeta_0}{T} \tan\left[\frac{\omega_\zeta T}{2}\right]. \tag{6.69}$$

Let us assume now that the time between impulses is small. In this case, the effective out-of-plane acceleration can be approximated as

$$\bar{a}_\zeta \approx \omega_\zeta^2 \zeta_0 + \frac{1}{12}\omega_\zeta^4 \zeta_0 T^2 + \dots \tag{6.70}$$

The relative displacement is given by

$$\begin{aligned} \Delta\zeta &= \zeta_{max} - \zeta_0, \\ &= \zeta\left(\frac{T}{2}\right) - \zeta_0, \\ &= -\zeta_0\left[1 - \cos\left(\frac{\omega_\zeta T}{2}\right)\right] + \frac{\dot{\zeta}_0}{\omega_\zeta}\sin\left(\frac{\omega_\zeta T}{2}\right), \\ &= -2\zeta_0 \sin^2\left(\frac{\omega_\zeta T}{4}\right) + \frac{\dot{\zeta}_0}{\omega_\zeta}\sin\left(\frac{\omega_\zeta T}{2}\right). \end{aligned} \tag{6.71}$$

By the use of equation (6.67), equation (6.71) can be rewritten as

$$\Delta\zeta = \xi_0\left[-2\sin^2\left(\frac{\omega_\zeta T}{4}\right) + \sin\left(\frac{\omega_\zeta T}{2}\right)\tan\left(\frac{\omega_\zeta T}{2}\right)\right]. \tag{6.72}$$

6.7.2 In-plane Maneuvers

Assume that a radial displacement has been performed, then the following conditions will be used

$$\xi(0) = \xi(T) = \xi_0, \tag{6.73}$$
$$\eta(0) = \eta(T) = \eta_0. \tag{6.74}$$

The representation of this technique is given in Figure 6.16.

From the equations (4.27) and (4.28) in Chapter 4 and Section 4.1, it is obtained for the in-plane motion, respectively

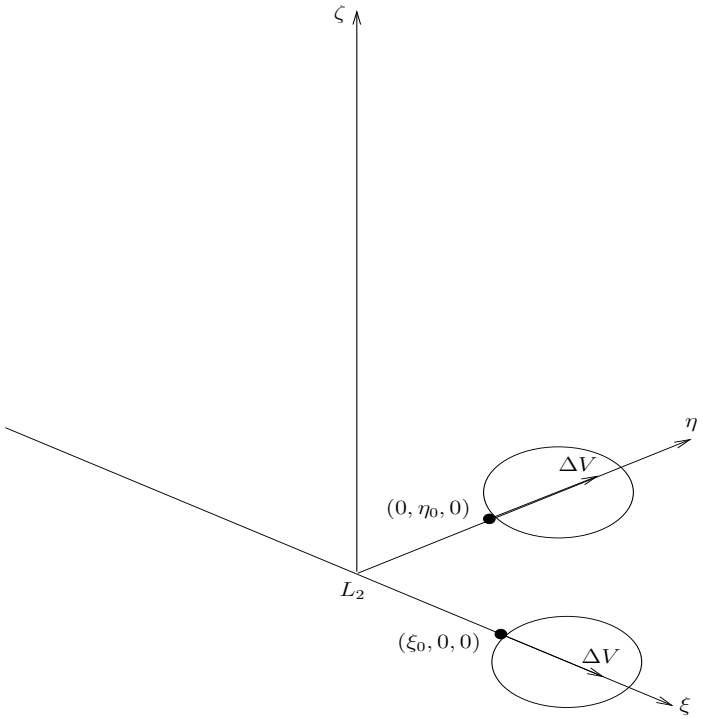

Figure 6.16: Orbit reference frame for impulse control (in-plane maneuvers).

$$\begin{aligned} \xi(0) &= A_3 + A_4 = \xi_0, && (6.75)\\ \xi(T) &= A_3 e^{\lambda_3 T} + A_4 e^{\lambda_4 T} = \xi_0, && (6.76) \end{aligned}$$

and

$$\begin{aligned} \eta(0) &= B_3 + B_4 = \eta_0, && (6.77)\\ \eta(T) &= B_3 e^{\lambda_3 T} + B_4 e^{\lambda_4 T} = \eta_0. && (6.78) \end{aligned}$$

In matrix form the system of equations above can be written as

$$\begin{bmatrix} 1 & 1 \\ e^{\lambda_3 T} & e^{\lambda_4 T} \end{bmatrix} \begin{bmatrix} A_3 \\ A_4 \end{bmatrix} = \begin{bmatrix} \xi_0 \\ \xi_0 \end{bmatrix}, \tag{6.79}$$

and

$$\begin{bmatrix} 1 & 1 \\ e^{\lambda_3 T} & e^{\lambda_4 T} \end{bmatrix} \begin{bmatrix} B_3 \\ B_4 \end{bmatrix} = \begin{bmatrix} \eta_0 \\ \eta_0 \end{bmatrix}. \tag{6.80}$$

Solving equation (6.79) (resp. equation (6.80)) for A_3 and A_4 (resp. for B_3 and B_4), yields the coefficients A_3, A_4, B_3 and B_4

$$\begin{bmatrix} A_3 \\ A_4 \end{bmatrix} = \frac{1}{-e^{\lambda_3 T} + e^{\lambda_4 T}} \begin{bmatrix} e^{\lambda_4 T} & -1 \\ -e^{\lambda_3 T} & 1 \end{bmatrix} \begin{bmatrix} \xi_0 \\ \xi_0 \end{bmatrix}, \tag{6.81}$$

$$\begin{bmatrix} B_3 \\ B_4 \end{bmatrix} = \frac{1}{-e^{\lambda_3 T} + e^{\lambda_4 T}} \begin{bmatrix} e^{\lambda_4 T} & -1 \\ -e^{\lambda_3 T} & 1 \end{bmatrix} \begin{bmatrix} \eta_0 \\ \eta_0 \end{bmatrix}, \tag{6.82}$$

and

$$A_3 = \frac{\xi_0}{-e^{\lambda_3 T} + e^{\lambda_4 T}} \Big(e^{\lambda_4 T} - 1 \Big), \tag{6.83}$$

$$A_4 = \frac{\xi_0}{-e^{\lambda_3 T} + e^{\lambda_4 T}} \Big(- e^{\lambda_3 T} + 1 \Big), \tag{6.84}$$

$$B_3 = \frac{\eta_0}{-e^{\lambda_3 T} + e^{\lambda_4 T}} \Big(e^{\lambda_4 T} - 1 \Big), \tag{6.85}$$

$$B_4 = \frac{\eta_0}{-e^{\lambda_3 T} + e^{\lambda_4 T}} \Big(- e^{\lambda_3 T} + 1 \Big). \tag{6.86}$$

Thus, the required initial velocity components are given respectively by

$$\begin{aligned} \dot{\xi}(0) &= \lambda_3 A_3 + \lambda_4 A_4, \\ &= \frac{\xi_0}{-e^{\lambda_3 T} + e^{\lambda_4 T}} \Big[\lambda_3 (e^{\lambda_4 T} - 1) + \lambda_4 (-e^{\lambda_3 T} + 1) \Big], \end{aligned} \tag{6.87}$$

$$\begin{aligned} \dot{\eta}(0) &= \lambda_3 B_3 + \lambda_4 B_4, \\ &= \frac{\eta_0}{-e^{\lambda_3 T} + e^{\lambda_4 T}} \Big[\lambda_3 (e^{\lambda_4 T} - 1) + \lambda_4 (-e^{\lambda_3 T} + 1) \Big]. \end{aligned} \tag{6.88}$$

If at time $t = 0$, the relative position ξ_0, η_0 and ζ_0 is known, then the relative velocity components $\dot{\xi}(0)$, $\dot{\eta}(0)$ and $\dot{\zeta}(0)$ can be determined. The components of the initial velocity are given by

$$\boldsymbol{V}(0) = \begin{bmatrix} \dot{\xi}(0) & \dot{\eta}(0) & \dot{\zeta}(0) \end{bmatrix}^T. \tag{6.89}$$

The terms $\dot{\xi}(T)$, $\dot{\eta}(T)$ and $\dot{\zeta}(T)$ are then the velocity components at time $t = T$ imparted along the ξ, η and ζ respectively, and denoted by

$$\boldsymbol{V}(T) = \begin{bmatrix} \dot{\xi}(T) & \dot{\eta}(T) & \dot{\zeta}(T) \end{bmatrix}^T. \tag{6.90}$$

Table 6.3: Requirements for displaced lunar orbits.

$Altitude(km)$	1750	2000	2500
a_0 (mms^{-2})	0.1	0.11	0.14
$\Delta V^a(ms^{-1})$	23	26	32
$\Delta V^b(ms^{-1})$	24.19	27.64	34.56

[a] Accumulated ΔV for low-thrust propulsion.
[b] Accumulated ΔV per orbit for impulse control (4 impulses per orbit).

Thus, the magnitude of the velocity impulse vector $\Delta \boldsymbol{V}$ in all directions is given by

$$\begin{aligned} |\Delta \boldsymbol{V}| &= |\boldsymbol{V}(T) - \boldsymbol{V}(0)|, \\ &= \sqrt{(\dot{\xi}(T) - \dot{\xi}(0))^2 + (\dot{\eta}(T) - \dot{\eta}(0))^2 + (\dot{\zeta}(T) - \dot{\zeta}(0))^2}. \end{aligned} \tag{6.91}$$

The requirements for impulse control and continuous thrust for different values of out-of-plane distance are shown in Table 6.3. For example a constant displacement distance of 1750 km requires an acceleration of 0.1 mm^{-2}, which correspond to a ΔV of 23 ms^{-1} per orbit for the continuous thrust control. Similarly, for impulse control using 4 impulses per orbit, the required ΔV is 24.19 ms^{-1} per orbit.

6.8 Summary

A hybrid concept for displaced periodic orbits in the Earth-Moon system has been developed. A feedback linearisation was used to perform stabilisation and trajectory tracking for nonlinear systems. The idea of this control is to transform a given nonlinear system into a linear system by use of a nonlinear coordinate transformation and nonlinear feedback. The augmented thrust acceleration is than applied to ensure a constant displacement periodic orbit, which provides key advantages for lunar polar telecommunications. A stabilising approach is then introduced to increase the damping in the system and to allow a higher gain in the controller. Theoretical and simulation results show good performance, with modest propellant mass requirements ($m_{prop} = 25\ kg$). Impulse control has also been investigated as an alternative to continuous thrust control.

Chapter 7

Asymptotic Analysis of Displaced Lunar Orbits

This chapter is concerned with the approximation of large displaced orbits in the Earth-Moon circular restricted three-body problem (CRTPB) by the Moon-Sail two-body problem. These orbits are achieved by orientating the solar sail so that it is directed perpendicular to the Sun-line and then pitched to provide an out-of-plane force. It is found that far from the L_1 and L_2 points, the approximate two-body analysis for large accelerations matches well with the dynamics of displaced Earth orbits in relation to the three-body problem. For small accelerations near the L_1 and L_2 points, a linear three-body analysis gives a good approximation. Throughout this chapter the dynamics of displaced orbits in relation to an approximate two-body Earth-Moon problem with a constant radiation pressure is considered. In order to carry out a linear stability analysis of approximate displaced two-body lunar orbits, a perturbation is then applied to the system and the resulting dynamics will be analysed.

7.1 Moon-Sail Three-Body Problem

The motion of a solar sail moving under the gravitational influences of the Earth and the Moon can be described in terms of the circular restricted three-body problem, as shown in Chapter 5, Section 5.1. In this model, it is again assumed that m_1 represents the larger primary (Earth), m_2 the smaller primary (Moon) and the motion of the sail which has a negligible mass ($m_1 > m_2$) will be considered. It is always assumed that the two more massive bodies (primaries) move in circular orbits about their common center of mass. If the motion of the third body is further restricted to be in the orbital plane formed by the other two bodies, the problem is the planar circular restricted three-body problem (PCRTBP). The time unit is defined such that, the orbital period of the primaries about their center of mass is 2π. The geometry for the Earth-Moon restricted three-body system is depicted in Figure 5.1.

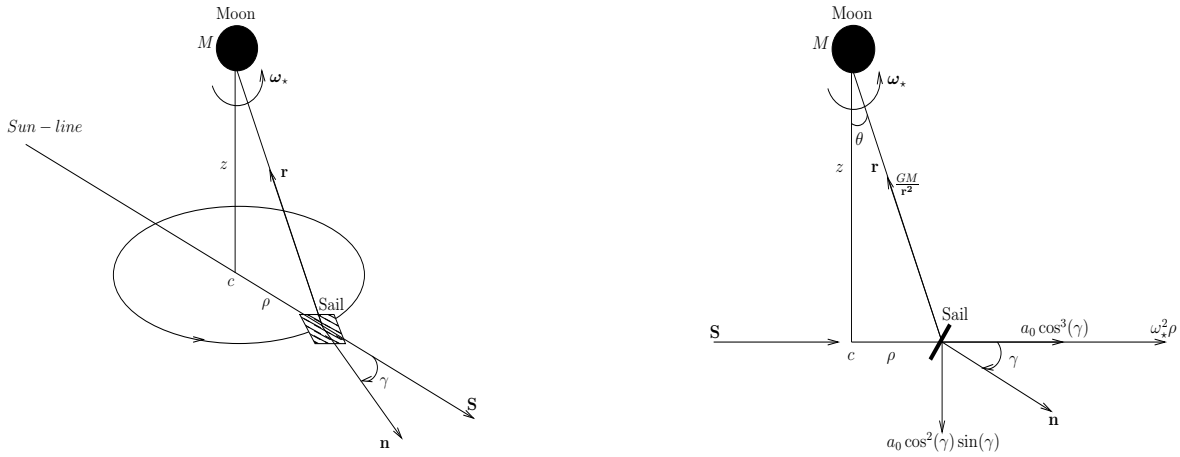

(a) (b)

Figure 7.1: (a) Schematic geometry of the Moon-Sail two-body problem generating a hover orbit displaced below Earth-Moon plane for lunar south pole communications; (b) Representative forces.

7.2 Moon-Sail Two-Body Problem

7.2.1 Introduction

The two-body problem is the only gravitational problem in celestial mechanics, apart from rather particular cases in the three-body problem, for which there exists a complete and general solution. A wide variety of practical orbital motion problems can be approximated by the two-body problem. In this section, the motion of a solar sail moving under the gravitational influence of the Moon only is considered, as shown in Figure 7.1 (a). Such a problem is defined as the Moon-Sail two-body problem. For a large displacement, such that the sail is far from the L_1 or L_2 points this provides a remarkably good approximation to the problem. The forces acting on the sail can be seen in Figure 7.1 (b). As is well known, the centripetal force directed along the ρ axis is proportional to the square of the angular velocity. From the perspective of an inertial reference frame, Figure 7.2 shows the Moon and the sail orbiting around the Earth.

7.2.2 Equations of motion

In this model, the Moon is assumed to be fixed, while the solar sail is in a rotating frame of reference. To describe the motion of the sail, a reference frame rotating with the Sun-line at angular velocity $\boldsymbol{\omega}_\star$ is considered, such that the origin is at the center c, as shown in Figure 7.1 (a). The two-body equations may be written in a similar form to equation (6.59). The equation of motion of the sail in a rotating frame of reference is described by

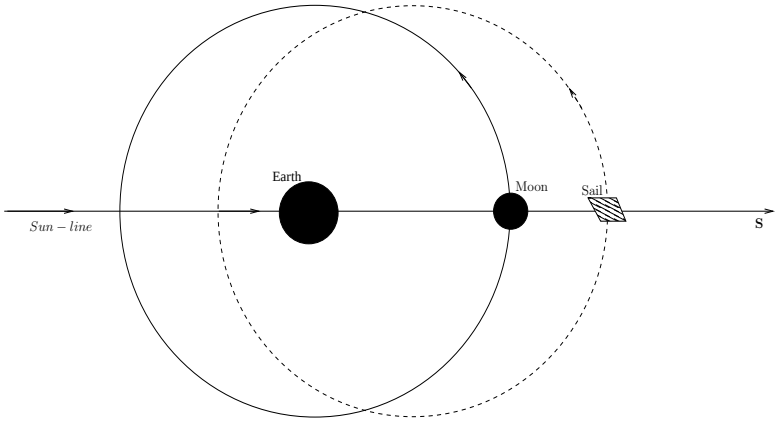

Figure 7.2: Schematic geometry of the Moon-Sail two-body orbiting around the Earth (inertial frame).

$$\frac{d^2\boldsymbol{r}}{dt^2} + 2\boldsymbol{\omega}_\star \times \frac{d\boldsymbol{r}}{dt} + \nabla\tilde{U}(\boldsymbol{r}) = \boldsymbol{a}, \tag{7.1}$$

where $\boldsymbol{\omega}_\star = \omega_\star \hat{\boldsymbol{z}}$ ($\hat{\boldsymbol{z}}$ is a unit vector pointing in the direction of $\boldsymbol{z}$) is the angular velocity vector of the rotating frame and $\boldsymbol{r}$ is the position vector of the solar sail to the central body. This frame of reference rotates with constant angular velocity relative to an inertial frame. In the rotating frame of reference, the condition for equilibrium solutions is obtained by setting $\ddot{\boldsymbol{r}} = \dot{\boldsymbol{r}} = 0$ so that

$$\nabla\tilde{U}(\boldsymbol{r}) = \boldsymbol{a}, \tag{7.2}$$

where

$$\tilde{U}(\boldsymbol{r}) = -\left[\frac{1}{2}|\boldsymbol{\omega}_\star \times \boldsymbol{r}|^2 + \frac{GM}{r}\right],$$

where M is the mass of the Moon and G is the gravitational constant.

By making use of a set of cylindrical polar coordinates (see Figure 7.1 (a)), the two-body potential function $\tilde{U}$ is given by

$$\tilde{U}(\rho, z; \omega_\star) = -\left[\frac{1}{2}(\omega_\star \rho)^2 + \frac{GM}{r}\right]. \tag{7.3}$$

Then, the partial derivative of the potential $\tilde{U}$ with respect to the position vector $\boldsymbol{r} = (\rho, \phi, z)$ that will be needed for the stability analysis in the next section are given by

$$\frac{\partial \tilde{U}}{\partial \rho} = -\rho(\omega_\star^2 - \tilde{\omega}^2), \tag{7.4}$$

$$\frac{\partial \tilde{U}}{\partial \phi} = 0, \tag{7.5}$$

$$\frac{\partial \tilde{U}}{\partial z} = z\tilde{\omega}^2. \tag{7.6}$$

From Figure 7.1 (b) the equations of motion of the solar sail in component form may be written in cylindrical coordinates (ρ, z) as

$$\frac{GM}{r^2}\cos(\theta) = a_0 \cos^2(\gamma)\sin(\gamma), \tag{7.7}$$

$$\frac{GM}{r^2}\sin(\theta) - \omega_\star^2\rho = a_0\cos^3(\gamma), \tag{7.8}$$

with $\cos(\theta) = \frac{z}{r}$, $\sin(\theta) = \frac{\rho}{r}$, and the distance of the solar sail from the Moon is $r = \sqrt{\rho^2 + z^2}$ so that

$$\frac{GMz}{r^3} = a_0 \cos^2(\gamma)\sin(\gamma), \tag{7.9}$$

$$\frac{GM\rho}{r^3} = a_0\cos^3(\gamma) + \omega_\star^2\rho. \tag{7.10}$$

Rearranging the equations (7.9) and (7.10), it is found that

$$\tan(\gamma) = \frac{z}{\rho}\left[1 - \left(\frac{\omega_\star}{\tilde{\omega}}\right)^2\right]^{-1}, \tag{7.11}$$

for a given (ρ,z), where

$$\tilde{\omega}^2 = \frac{GM}{r^3}. \tag{7.12}$$

Similary from equations (7.9) and (7.10), the required radiation pressure acceleration for the two-body analysis may also be obtained as

$$a_0(\rho, z) = \cos^2(\gamma)^{-1}\left[\left((\tilde{\omega}^2 z)^2 + \left(\tilde{\omega}^2\rho - \omega_\star^2\rho\right)^2\right]^{1/2}. \tag{7.13}$$

With these conditions the spacecraft appears to execute a circular orbit displaced above or below the moon.

7.3 Comparison of the linear three-body and the approximate two-body solution

In this section, the dynamics near the Earth-Moon L_1 and L_2 points for small accelerations with the linear analysis is compared, and the large hover orbits for large acceleration with the two-body analysis to the orbit found by Ozimek et al. [84] using a full three-body analysis. It is demonstrated that for a given orbit radius ρ and displacement distance z, the characteristic acceleration a_0 and the sail pitch angle γ can be found using the two-body analysis.

Let us consider the vector field on the plane given by

$$\boldsymbol{n}(\rho, z) = \left(\frac{f_2(\rho, z)}{\sqrt{f_1^2(\rho, z) + f_2^2(\rho, z)}}, \frac{f_1(\rho, z)}{\sqrt{f_1^2(\rho, z) + f_2^2(\rho, z)}} \right), \tag{7.14}$$

where

$$f_1(\rho, z) = \frac{Gm_2 z}{r^3}, \tag{7.15}$$

$$f_2(\rho, z) = \frac{Gm_2 \rho}{r^3} - \omega_\star^2 \rho. \tag{7.16}$$

For a given (ρ,z) the contours of Figure 7.3 define the require sail accelaration a_0 from equation (7.13) while the vector field describes the required sail orientation $\boldsymbol{n}$. From equations (7.9) and (7.10), this vector field defined on the whole plane minus the origin describes the direction of the acceleration vector $a_0 = a_0(\rho, z)$. This figure indicates for a large characteristic acceleration $a_0 = 1.7\ mm/s^2$ an orbit with radius $\rho \approx 6 \times 10^4\ km$ and displacement distance $z \approx 4 \times 10^4\ km$ is possible. The point marked A in Figure 7.3 represents the optimal displaced orbit (maximum displacement) for an acceleration $a_0 = 1.7\ mm/s^2$, equivalent to the hover orbit investigated by Ozimek et al. [84].

A small orbit at L_2 with characteristic acceleration $a_0 = 0.58\ mm/s^2$ is shown in Figure 7.4 using the linear analysis from Section 7.1. Near L_1 and L_2 the displacement distance for the linear analysis for a small acceleration $a_0 = 0.58\ mm/s^2$ and the two-body analysis for large acceleration $a_0 = 1.7 mm/s^2$ give a good approximation to the orbits found by Ozimek et al. [84] using a full three-body analysis (see Table 7.1). Now, the linear stability properties of the families of orbits will be investigated.

Table 7.1: Comparison of displacement distance.

a_0 (mm/s^2)	z $(km)^a$	z $(km)^b$	$\rho(km)^a$	$\rho(km)^b$
0.58	$\approx 10^4$	$\approx 10^{4*}$	–	–
1.70	$\approx 4.5 \times 10^4$	$\approx 4.0 \times 10^{4\dagger}$	$\approx 5.6 \times 10^4$	$\approx 6.5 \times 10^4$

[a] Displacement and Radius found by Ozimek et al. using Hermite-Simpson and seventh-degree Gauss Lobatto collocation schemes [84].

[b] Displacement and Radius found by the approximate analysis in this Chapter.

[*] Displacement distance obtain from the linear analytical solution.

[†] Displacement distance obtain from the two-body approximation.

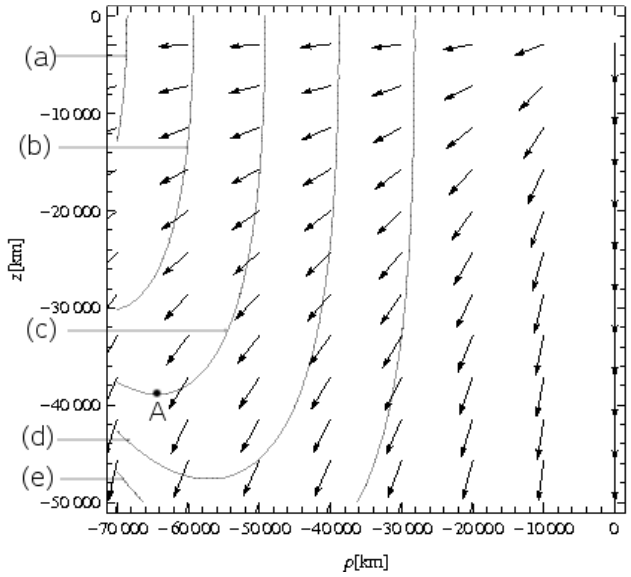

Figure 7.3: A contour plot and the vector field of the characteristic acceleration $a_0 = a_0(\rho, z)$ in the Earth-Moon system: (a) $a_0 = 0.58\ mm/s^2$, (b) $a_0 = 1\ mm/s^2$, (c) $a_0 = 1.7\ mm/s^2$, (d) $a_0 = 3\ mm/s^2$, (e) $a_0 = 6\ mm/s^2$.

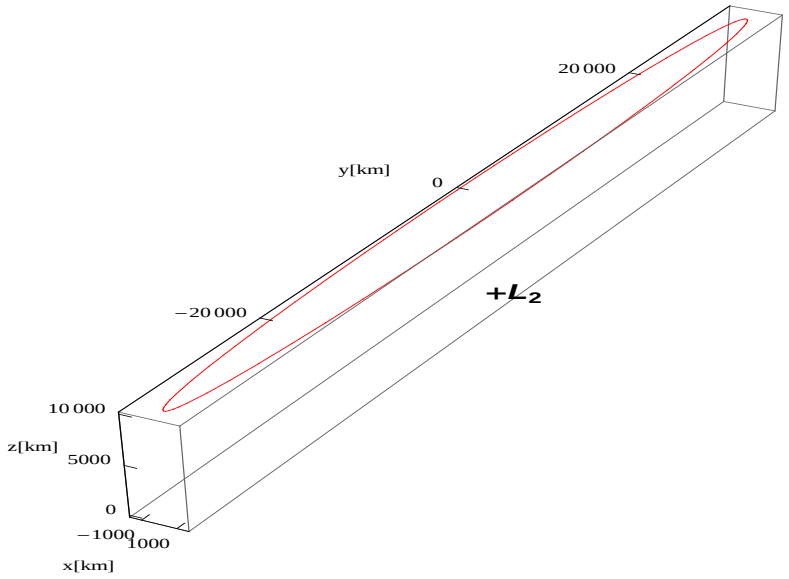

Figure 7.4: Linear analysis for small $a_0 = 0.58\ mm/s^2$ (orbit around L_2).

7.4 Stability of Approximate Displaced Lunar Orbits

7.4.1 Linearised system

The nonlinear equation of motion in the rotating frame of reference will now be linearised by adding a pertubation σ such that $\boldsymbol{r} \rightarrow \bar{\boldsymbol{r}} + \sigma$, where $\bar{\boldsymbol{r}} = (\bar{\rho}, \bar{\phi}, \bar{z})$ corresponds to the nominal displaced non-Keplerian orbit solution. Then, the variational equation is obtained from the nonlinear equation of motion, equation (6.1) as

$$\ddot{\sigma} + 2\boldsymbol{\omega}_\star \times \dot{\sigma} + \Lambda\sigma = 0, \tag{7.17}$$

where

$$\Lambda = \left[\frac{\partial \nabla \tilde{U}}{\partial \boldsymbol{r}}\right]_{\boldsymbol{r}=\bar{\boldsymbol{r}}}.$$

Defining the pertubations in $\bar{\boldsymbol{r}} = (\bar{\rho}, \bar{\phi}, \bar{z})$ as $\sigma = (\xi, \psi\bar{\rho}, \eta)$, so that equation (7.17) may be written as

$$\begin{bmatrix} \ddot{\xi} \\ \bar{\rho}\ddot{\psi} \\ \ddot{\eta} \end{bmatrix} + \begin{bmatrix} -2\omega_\star\dot{\psi}\bar{\rho} \\ 2\omega_\star\dot{\xi} \\ 0 \end{bmatrix} + \begin{bmatrix} \lambda_{11} & 0 & \lambda_{12} \\ 0 & 0 & 0 \\ \lambda_{21} & 0 & \lambda_{22} \end{bmatrix} = \begin{bmatrix} 0 \\ 0 \\ 0 \end{bmatrix}, \tag{7.18}$$

where $\lambda_{11} = \tilde{U}_{\rho\rho}$, $\lambda_{12} = \tilde{U}_{\rho z}$, $\lambda_{21} = \tilde{U}_{z\rho}$ and $\lambda_{22} = \tilde{U}_{zz}$. By extracting the azimuthal terms from equation (7.18), it is found that

$$\bar{\rho}\ddot{\psi} + 2\omega_\star\dot{\xi} = 0, \tag{7.19}$$

$$\ddot{\psi} + \frac{2\omega_\star}{\bar{\rho}}\dot{\xi} = 0, \tag{7.20}$$

and equation (7.20) immediately integrates to

$$\dot{\psi} = -\frac{2\omega_\star}{\bar{\rho}}\xi + C, \tag{7.21}$$

where C is a constant of integration.

By making use of equation (7.21), the first derivative terms from equation (7.18) will be removed to enable the variational equation to be written as

$$\begin{bmatrix} \ddot{\xi} \\ \ddot{\eta} \end{bmatrix} + \begin{bmatrix} \lambda_{11} & \lambda_{12} \\ \lambda_{21} & \lambda_{22} \end{bmatrix} \begin{bmatrix} \xi \\ \eta \end{bmatrix} = \begin{bmatrix} 2\omega_\star C\bar{\rho} \\ 0 \end{bmatrix}. \tag{7.22}$$

In the following the bar notation is removed for clarity, so the matrix elements can be written as

$$\lambda_{11} = 3\omega_\star^2 + \tilde{\omega}^2[1 - 3(\rho/r)^2], \tag{7.23}$$
$$\lambda_{12} = \lambda_{21} = -3\tilde{\omega}^2[\rho z/r^2], \tag{7.24}$$
$$\lambda_{22} = \tilde{\omega}^2[1 - 3(z/r)^2]. \tag{7.25}$$

Defining the transformation as

$$\xi = \xi^{'} + \frac{2\omega_\star C}{\lambda_{11}}\rho, \tag{7.26}$$
$$\eta = \eta^{'}, \tag{7.27}$$

a more familiar equation is then obtained if equations (7.26) and (7.27) are substituted in the above expression (equation 7.22) to obtain

$$\begin{bmatrix} \ddot{\xi}^{'} \\ \ddot{\eta}^{'} \end{bmatrix} + \begin{bmatrix} \lambda_{11} & \lambda_{12} \\ \lambda_{12} & \lambda_{22} \end{bmatrix} \begin{bmatrix} \xi^{'} \\ \eta^{'} \end{bmatrix} = \begin{bmatrix} 0 \\ 0 \end{bmatrix}. \tag{7.28}$$

The stability characteristics of the approximate displaced two-body lunar orbits can be easily investigated by calculating the eigenvalues of the variational equation. Therefore, the eigenvalues may now be obtained by substituting an exponential solution of the form

$$\begin{bmatrix} \xi^{'} \\ \eta^{'} \end{bmatrix} = \begin{bmatrix} \xi_0 \\ \eta_0 \end{bmatrix} \exp(\mu t). \tag{7.29}$$

Substituting this solution into equation (7.28) yields a matrix equation of the form

$$\begin{bmatrix} \mu^2 + \lambda_{11} & \lambda_{12} \\ \lambda_{12} & \mu^2 + \lambda_{22} \end{bmatrix} \begin{bmatrix} \xi_0 \\ \eta_0 \end{bmatrix} = \begin{bmatrix} 0 \\ 0 \end{bmatrix}. \tag{7.30}$$

The characteristic polynomial of the variational equation is then found to be

$$f(\mu^2) = \mu^4 + \mu^2(\lambda_{11} + \lambda_{22}) + (\lambda_{11}\lambda_{22} - \lambda_{12}^2), \tag{7.31}$$

and will be used to establish regions of linear stability and instability for approximate displaced two-body lunar orbits. The stability of the orbits depends on the properties of the characteristic equation given by equation (7.31). Thus, to guarantee nonpositive roots, and thus linear stability, it is required that the coefficients as well as the discriminant of the quadratic in μ^2 be positive. This can be shown to be true for displaced two-body lunar orbits in the case of the discriminant. By searching for regions with purely imaginary eigenvalues, the stability properties of displaced two-body lunar orbits will be determined.

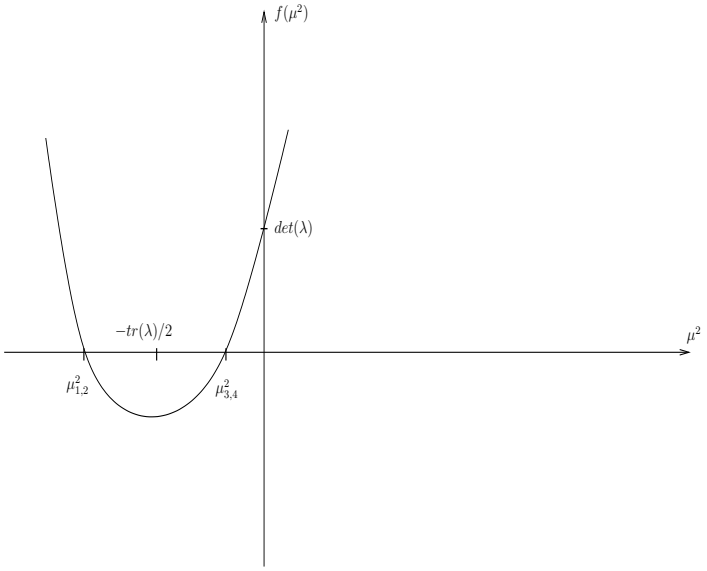

Figure 7.5: Roots of the characteristic polynomial.

It is required that both $det(\lambda) = \lambda_{11}\lambda_{22} - \lambda_{12}^2 > 0$ and $tr(\lambda) = \lambda_{11} + \lambda_{22} > 0$ for purely imaginary eigenvalues (see Figure 7.5). Then, it is found that

$$\lambda_{11} + \lambda_{12} = 3\omega_\star^2 - \tilde{\omega}^2, \tag{7.32}$$

$$\lambda_{11}\lambda_{22} - \lambda_{12}^2 = \tilde{\omega}^2\left[3\omega_\star^2\left(1 - 3\left(\frac{z}{r}\right)^2\right) - 2\tilde{\omega}^2\right]. \tag{7.33}$$

The first coefficient is strictly positive if

$$r > \sqrt[3]{\frac{GM}{3\omega_\star^2}}. \tag{7.34}$$

In addition the second coefficient is strictly positive if

$$3\tilde{\omega}^2\omega_\star^2\left(1 - 3\left(\frac{z}{r}\right)^2\right) - 2\tilde{\omega}^4 > 0. \tag{7.35}$$

7.4.2 Stability Comparison Analysis

For the stable two-body approximation with $z = 0$, $\rho > 81,360\ km$, which lies well beyond the L_1 point (see Figure 7.6). It can be seen then that the family of approximate displaced two-body lunar orbits is partitioned into stable and unstable groups by the conditions $det(\lambda) > 0$ and $tr(\lambda) > 0$ as shown in Figure (7.6). Thus, the stable partition satisfies the inequalities (7.34) and (7.35). In addition, it is advantageous in practice to use stable orbits to avoid the need for active control. However, as shown in Figure 7.6, orbits with a

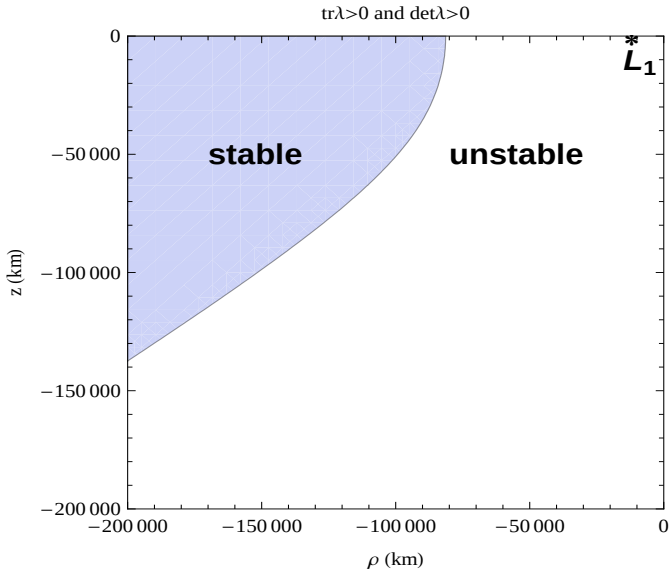

Figure 7.6: Stable and unstable regions of the ρ-z plane.

large displacement are unstable. There is a need to develop new simple control schemes to stabilise the unstable orbit families.

Now, due to the fact that the linearisation is performed, the analysis of the stability provides only necessary conditions for stability and sufficient conditions for instability. In addition, it may be noted that the model is an approximation to the full three-body problem, but can provide a guide to understanding numerically generated trajectories such as those in reference [84].

7.5 Summary

This chapter has demonstrated the approximation of large displaced orbits in the Earth-Moon circular restricted three-body problem by the Moon-Sail two-body problem. In addition, based on the linearised equation of motion near the collinear Lagrange points, displaced periodic orbits can be approximated by using linear analysis, while far from those points the classical two-body problem gives a good approximation. A sufficient condition for displaced periodic orbits based on the sail pitch angle and the magnitude of the solar radiation pressure for fixed initial out-of-plane distance has been derived. It was shown that for a given orbit radius and displacement distance, the characteristic acceleration and the sail pitch angle can be found using the two-body analysis. The orbits found approach the asymtotic solutions as the characteristic acceleration becomes large. A method was then developed to study the stability of the approximate displaced two-body lunar orbits. It was found that orbits with a large displacement are unstable as expected. Again a particular use of such orbits include continous communications between the equatorial regions of the Earth and the lunar poles.

Chapter 8

Conclusions and Future Work

8.1 Conclusions

The use of numerically integrated solutions, most often based on analytic approximations, has enabled the examination of a wide range of displaced orbit solutions in the Earth-Moon system. The goal has been to identify novel families of highly non-Keplerian orbits for spacecraft utilising either solar sail or solar electric propulsion at linear order in the Earth-Moon circular restricted three-body problem.

Firstly, new families of orbits for solar sails at linear order in the Earth-Moon system have been studied. A suffcient condition for displaced periodic orbits based on the sail pitch angle and the magnitude of the solar radiation pressure for fixed initial out-of-plane distance has been derived. By making use of a first-order approximation, periodic orbits are derived analytically at linear order. It was found that for a given displacement distance above/below the Earth-Moon plane it is easier by a factor of order 3.19 to do so at L_4/L_5 compared to L_1/L_2 - ie. for a fixed sail acceleration the displacement distance at L_4/L_5 is greater than that at L_1/L_2. Furthermore, displaced L_4/L_5 orbits are passively stable, making them more forgiving to sail pointing errors than highly unstable orbits at L_1/L_2. The drawback of the new family of orbits is the increased telecommunications path-length, particularly the Moon-L_4 distance compared to the Moon-L_2 distance. Thereafter, solar sail propulsion is used to provide station-keeping at periodic orbits around the libration points using small variations in the sail's orientation. Thus, the z-position is maintained at the triangular libration points by adjusting the control angle γ in such a way that it will cancel disturbances that drive the sail away from those points. The linear feedback controller is developed by linearising the z-dynamics around the triangular libration points and some sail attitude γ_0.

However, trajectories near the Earth-Moon L_1 and L_2 points are not easily identified, such that the solar sail can enable continuous communications with the equatorial regions of the Earth from any point on the lunar far-side. Hence, displaced periodic orbits at linear order in the circular restricted Earth-Moon system have been investigated, where the third massless body utilises a hybrid of solar sail and a solar electric propulsion system.

A feedback linearisation control scheme is proposed and implemented, where the main idea is to cancel the nonlinearities and to impose desired linear dynamics satisfied by the solar sail. The SEP control is then selected, which takes into consideration the nonlinearity cancellation and the stabilising linear control. When the control is applied to the nonlinear system, asymptotic stability is achieved. This provides the key advantage that the displacement distance of the hybrid sail is then constant. For practical applications, a constant displacement distance may lead to easier tracking from the lunar surface for communications applications. Furthermore, impulse control is investigated as a means of enabling displaced lunar orbits and is compared to continuous thrust control.

Then, the dynamics of displaced orbits in relation to the two and three-body Earth-Moon problem is studied and the results are compared. An asymptotic analysis for large ($a_0 = 1.7mm/s^2$) and small ($a_0 = 0.58mm/s^2$) accelerations has been developed. The analysis is obtained within an approximation of large displaced orbits ($a_0 = 1.7mm/s^2$) by the Moon-Sail two-body problem. The displaced periodic orbits found approach the asymptotic solutions as the characteristic acceleration becomes large. This simple, two-body approximate analysis matches with the large displaced orbit found by Ozimek et al. [84] using numerical collocation methods in a related work. For small accelerations a linear approximation of the Earth-Moon three-body problem is used, which again matches well with the orbit found in reference [84]. Moreover, the linear stability characteristics of the families of approximate periodic orbits are investigated.

The new families of orbits have the property of ensuring visibility of both the lunar far-side and the equatorial regions of the Earth, and can enable new ways of performing lunar telecommunications.

8.2 Future Work

Despite the models and results reported in the literature and this thesis, there are many open issues. A few of these issues are discussed in this section.

As already mentioned in Chapter 2 Section 2.1.5, the assumption of an ideal flat solar sail can render the model inaccurate. While it is now certainly possible to generate displaced lunar orbits using a simplified solar sail model (perfect reflector), it would be interesting to extend the work by considering a non-ideal sail in more detail. In this new configuration (non-perfect solar sail), the resultant force vector will not be in the direction normal to the sail surface since the absorbed photons force is greater than the force due to reflected photons. Future solar sail design studies will require detailed force models which can also take into account the sail film optical properties, sail shape and changing sail temperature.

Now that the concept of displaced lunar orbits has been defined and implemented, the next stage of the design process is to compute a transfer trajectory from an initial Earth orbit to a displaced orbit around the Moon. For such a problem, obtaining a satisfactory initial guess is much more difficult. These circumstances have motivated the development of evolutionary algorithms such as genetic algorithms (GA), which can provide a solution

to the problem. More precisely, this technique can be used as pre-processors to provide an initial guess of the solution from which a method such as direct collocation with nonlinear programming (NLP) can converge to a much more accurate solution.

While the Sun-Jupiter system already possesses a collection of asteroids at the triangular libration points, a dust cloud derived from elsewhere in the solar system (comet fragments or lunar origin) can be eventually maintained for a relatively short period around the stable Earth-Moon triangular libration points L_4 and L_5. The dust could provide significant insolation reduction to offset radiative forcing by carbon dioxide. However, bodies at the triangular libration points of the Earth-Moon system would face pertubations from the Sun. Therefore, long-lived pertubed orbits and the effects of driving the annual and long-term climate with periodic changes in solar radiation are all important steps to be considered in the future.

In Chapter 7, it has been shown that families of displaced lunar orbits exist. These families have both linearly stable and unstable subfamilies with the two-body analysis. It was found that orbits with a large displacement are unstable. In practice they are all unstable since we are approximating the three-body problem. Further investigation will examine the controllability and stabilisability of the unstable subfamilies. We conclude with a discussion of how these results may be applied to additional techniques, which may further improve performance through the use of linear or nonlinear controllers.

In addition to the families of orbits discussed above, it will be possible to demonstrate that displaced lunar orbits may be patched together, providing additional new families of orbits in the Earth-Moon CRTBP.

Bibliography

[1] Farquhar, R., "Limit Cycle Analysis of a Controlled Libration-Point Satellite," *Journal of the Astronautical Sciences*, Vol. 17, No. 5, 1970, pp. 267–291.

[2] Colombo, G., "Sui Satelliti Sistema Terra-Luna," *Rediconti Accademica Nazionale Dei Lincei, Series 8*, Vol. 28, 1960, pp. 169–172.

[3] Colombo, G., "The Stabilization of an Artificial Satellite at the Inferior Conjunction Point of the Earth-Moon System," *Technical Report 80, Smithsonian Astrophysical Observatory Special Report*, 1961.

[4] McInnes, C. R., *Solar Sailing: Technology, Dynamics and Mission Applications*, Springer Praxis, London, 1999.

[5] McInnes, C., "Solar Sailing: Mission Applications and Engineering Challenges," *Royal Society of London Philosophical Transactions A: Mathematical, Physical and Engineering Sciences*, Vol. 361, No. 1813, November 2003, pp. 2989–3008.

[6] McInnes, C. R., "Minimum Mass Solar Shield for Terrestrial Climate Control," *JBIS, Journal of the British Interplanetary Society*, Vol. 55, No. 9-10, 2002, pp. 307–311.

[7] Prado, J.-Y., Perret, A., and Pignolet, G., "Using a Solar Sail for a Plasma Storm Early Warning System," *In* 47^{th} *International Astronautical Congress*, October 1996.

[8] Angel, R., "Feasibility of Cooling the Earth with a Cloud of Small Spacecraft near the Inner Lagrange Point (L_2)," *PNAS*, Vol. 103, No. 46, 2006, pp. 17184–17189.

[9] Vulpetti, G., "Sailcraft Trajectory Options for the Interstellar Probe: Mathematical Theory and Numerical Results," *Chapter IV of NASA/CR-2002-211730, "The Interstellar Probe (ISP): Pre- Perihelion Trajectories and Application of Holography"*, June 2002.

[10] Vulpetti, G., "Sailcraft at High Speed by Orbital Angular Momentum Reversal," *Acta Astronautica*, Vol. 40, No. 10, 1997, pp. 733–758.

[11] Vulpetti, G., Johnson, L., and Matloff, G. L., "Solar Sail: A Novel Approach to Interplanetary Travel," *Praxis, New York*, 2008.

[12] Rayman, M. D., Chadbourne, P. A., Culwell, J. S., and Williams, S. N., "Mission Design for Deep Space 1: A Low-Thrust Technology Validation Mission," *Acta Astronautica*, Vol. 45, 1999, pp. 381–388.

[13] Rayman, M. and Williams, S., "Design of the First Interplanetary Solar Electric Propulsion Mission," *Journal of Spacecraft and Rockets*, Vol. 39, No. 4, July-August 2002, pp. 589–595.

[14] Poincaré, H., "Les Méthodes Nouvelles de la Mécanique Céleste," *Gauthier-Villars et fils, Paris*, 1892.

[15] Waters, T. and McInnes, C., "Periodic Orbits above the Ecliptic in the Solar-Sail Restricted Three-Body Problem," *Journal of Guidance, Control, and Dynamics*, Vol. 30, No. 3, 2007, pp. 687–693.

[16] Waters, T. and McInnes, C., "Invariant Manifolds and Orbit Control in the Solar Sail Three-Body Problem," *Journal of Guidance, Control, and Dynamics*, Vol. 31, No. 3, 2008, pp. 554–562.

[17] Baoyin, H. and McInnes, C., "Solar Sail Halo Orbits at the Sun-Earth Artificial L_1 Point," *Celestial Mechanics and Dynamical Astronomy*, Vol. 94, No. 2, 2006, pp. 155–171.

[18] Baoyin, H. and McInnes, C., "Solar Sail Equilibria in the Elliptical Restricted Three-Body Problem," *Journal of Guidance, Control and Dynamics*, Vol. 29, No. 3, 2006, pp. 538–543.

[19] Baoyin, H. and McInnes, C., "Solar Sail Orbits at Artificial Sun-Earth Lagrange Points," *Journal of Guidance, Control and Dynamics*, Vol. 28, No. 6, 2005, pp. 1328–1331.

[20] McInnes, C., McDonald, A., Simmons, J., and McDonald, E., "Solar Sail Parking in Restricted Three-Body Systems," *Journal of Guidance, Control and Dynamics*, Vol. 17, No. 2, 1994, pp. 399–406.

[21] McInnes, C. R., "Artificial Lagrange Points for a Non-Perfect Solar Sail," *Journal of Guidance, Control and Dynamics*, Vol. 22, No. 1, 1999, pp. 185–187.

[22] Mclnnes, C. R. and Simmons, J. F. L., "Solar Sail Halo Orbits I: Heliocentric Case," *Journal of Spacecraft and Rockets*, Vol. 29, No. 4, July-August 1992, pp. 466–471.

[23] Molostov, A. A. and Shvartsburg, A. A., "Heliocentric Halos for a Solar Sail with Absorption," *Soviet Physics Doklady*, Vol. 37, No. 3, 1992, pp. 149–152.

[24] Molostov, A. A. and Shvartsburg, A. A., "Heliocentric Synchronous Halos for a Solar Sail with Absorption," *Soviet Physics Doklady*, Vol. 37, No. 4, 1992, pp. 195–197.

[25] Molostov, A. A. and Shvartsburg, A. A., ""Best" Solar Sail for Heliocentric Halos," *Soviet Physics Doklady*, Vol. 37, No. 6, 1992, pp. 290–293.

[26] Van der Ha, J. and Modi, V. J., "Long-term Evaluation of Three-Dimensional Heliocentric Solar Sail Trajectories with Arbitrary Fixed Sail Setting," *Celestial Mechanics and Dynamical Astronomy*, Vol. 19, No. 2, February 1979, pp. 113–138.

[27] Wokes, S., Palmer, P., and Roberts, M., "Classification of Two-Dimensional Fixed-Sun-Angle Solar Sail Trajectories," *Journal of Guidance, Control, and Dynamics*, Vol. 31, No. 5, September-October 2008, pp. 1249–1258.

[28] Mclnnes, C. R. and Simmons, J. F. L., "Solar Sail Halo Orbits II: Geocentric Case," *Journal of Spacecraft and Rockets*, Vol. 29, No. 4, July-August 1992, pp. 472–479.

[29] Shvartsburg, A. A., "Geocentric Halos for a Solar Sail with Absorption," *Soviet Physics Doklady*, Vol. 38, No. 2, 1993, pp. 85–88.

[30] Glotova, M. Y. and Shvartsburg, A. A., "Geocentric Synchronous Halos for a Solar Sail," *Soviet Physics Doklady*, Vol. 38, No. 12, 1993, pp. 449–501.

[31] Fekete, T. A., Sackett, L. L., and von Flotow, A. H., "Trajectory Design for Solar Sailing from Low-Earth Orbit to the Moon," *Advances in Astronautical Sciences*, Vol. 79, No. 3, 1992. AAS 92-184, pp. 1083–1094.

[32] McInnes, C., "The Existence and Stability of Families of Displaced Two-Body Orbits," *Celestial Mechanics and Dynamical Astronomy*, Vol. 67, No. 2, 1997, pp. 167–180.

[33] McInnes, C., "Dynamics, Stability, and Control of Displaced Non-Keplerian Orbits," *Journal of Guidance, Control and Dynamics*, Vol. 21, No. 5, September-October 1998, pp. 799–805.

[34] Hughes, G. W. and McInnes, C. R., "Solar Sail Hybrid Trajectory Optimization for Non-Keplerian Orbit Transfers," *Journal of Guidance, Control, and Dynamics*, Vol. 25, No. 3, May-June 2002, pp. 602–604.

[35] Forward, R. L., "Statite: A Spacecraft That Does Not Orbit," *Journal of Spacecraft and Rockets*, Vol. 28, No. 5, 1991, pp. 606–611.

[36] Bookless, J. and McInnes, C. R., "Dynamics and Control of Displaced Periodic Orbits using Solar Sail Propulsion," *Journal of Guidance, Control, and Dynamics*, Vol. 29, No. 3, May-June 2006, pp. 527–537.

[37] Dankowicz, H., "Some Special Orbits in the Two-Body Problem with Radiation Pressure," *Celestial Mechanics and Dynamical Astronomy*, Vol. 58, No. 4, 1994, pp. 353–370.

[38] McInnes, C. R., "Orbits in a Generalized Two-Body Problem," *Journal of Guidance, Control, and Dynamics*, Vol. 26, No. 5, September-October 2003.

[39] Topputo, F., Owis, A. H., and Bernelli-Zazzera, F., "Analytical Solution of Optimal Feedback Control for Radially Accelerated Orbits," *Journal of Guidance, Control, and Dynamics*, Vol. 31, No. 5, September-October 2008.

[40] McKay, R. J., Macdonald, M., Frescheville, F. B. D., Vasile, M., McInnes, C. R., and Biggs, J. D., "Non-Keplerian Orbits using Low Thrust, High ISP Propulsion Systems," *In* 60^{th} *International Astronautical Congress*, Daejeon, Republic of Korea, 12 - 16 October 2009. IAC-09.C1.2.8.

[41] Chapront, J. and Francou, G., "The Lunar Libration: Comparisons Between Various Models - A Model Fitted to LLR Observations," *Journes 2004. Fundamental Astronomy: New Concepts and Models for High Accuracy Observations*, Paris, France, September 20 - 24, 2004.

[42] Starchville, T. and Melton, R., "Optimal Low-Thrust Trajectories to Earth-Moon L_2 Halo Orbits (Circular Problem)," *In AAS/AIAA Astrodynamics Specialist Conference*, Sun Valley, Idaho, August 4 - 7, 1997. AAS 97-714.

[43] J. Condon, D. P., "The Role of Humans in Libration Point Missions with Specific Applications to an Earth-Moon Libration Point Gateway Station," *In AAS/AIAA Astrodynamics Specialist Conference*, Quebec City, Canada, 30 July - 2 August, 2001. AAS 01-307.

[44] Szebehely, V., *Theory of Orbits: the Restricted Problem of Three-Bodies*, Academic Press, New York and London, 1967.

[45] Roy, A. E., *Orbital Motion*, Institute of Physics Publishing, Bristol and Philadelphia, 2005.

[46] Vonbun, F., ""A Humminbird for the L_2 Lunar Libration Point"," *NASA TN-D-4468*, April 1968.

[47] Gómez, G., Llibre, J., Martínez, R., and Simó, C., *Dynamics and Mission Design near Libration Points*, Vol. I, II, World Scientific Monograph Series in Mathematics, 2001.

[48] Gómez, G., Jorba., A., J.Masdemont, and Simó, C., *Dynamics and Mission Design near Libration Points*, Vol. III, IV, World Scientific Monograph Series in Mathematics, 2001.

[49] Gómez, G., Howell, K. C., Masdemont, J., and Simó, C., "Station-Keeping Strategies for Translunar Libration Point Orbits," *In AAS/AIAA Space Flight Mechanics Meeting*, Monterey, California, February 9 - 11, 1998. AAS 98-168.

[50] Farquhar, R. and Kamel, A., "Quasi-Periodic Orbits about the Translunar Libration Point," *Celestial Mechanics*, Vol. 7, 1973, pp. 458–473.

[51] Farquhar, R., "The Utilization of Halo Orbits in Advanced Lunar Operations," *Nasa technical report*, 1971.

[52] Farquhar, R., "Comments on Optimal Controls for out-of-plane Motion about the Translunar Libration Point," *Journal Spacecraft and Rockets*, Vol. 8, 1971, pp. 815–816.

[53] Broucke, R., "Traveling Between the Lagrange Points and the Moon," *Journal of Guidance, Control, and Dynamics*, Vol. 4, No. 2, 1979, pp. 257–263.

[54] Broucke, R. A., "Periodic Orbits in the Restricted Three-Body Problem with Earth-Moon Masses," *Technical Report 32-1168, Jet Propulsion Laboratory*, February 1968.

[55] Farquhar, R. W. and Dunham, D. W., "Use of Libration-Point Orbits for Space Observatories," *In Observatories in Earth Orbit and Beyond, Kluwer Academic Publishers*, 1990, pp. 391–395.

[56] Farquhar, R. W. and Dunham, D. W., "Stationkeeping Techniques for Libration-Point Satellites," *Journal of Astronautical Sciences*, Vol. 49, No. 1, January 2001, pp. 127–144.

[57] Breakwell, J. and Brown, J., "The 'Halo' Family of 3-Dimensional Periodic Orbits in the Earth-Moon Restricted Three-Body Problem," *Celestial Mechanics*, Vol. 20, 1979, pp. 389–404.

[58] Breakwell, J. V., Kamel, A. A., and Ratner, M. J., "Station-Keeping for a Translunar Communication Station," *Celestial Mechanics*, Vol. 10, No. 3, 1974, pp. 357–373.

[59] Richardson, D. L., "Halo Orbit Formulation for the ISEE-3 mission," *Journal Guidance and Control*, Vol. 3, No. 6, 1980, pp. 543–548.

[60] Richardson, D. L., "A note on a Lagrangian Formulation for Motion about the Collinear Points," *Celestial Mechanics*, Vol. 22, 1980, pp. 231–236.

[61] Howell, K., "Three-Dimensional, Periodic, 'Halo' Orbits," *Celestial Mechanics*, Vol. 32, 1984, pp. 53–71.

[62] Howell, K. C. and Pernicka, H. J., "A Station-Keeping Method for Libration Point Trajectories," *Journal of Guidance, Control, and Dynamics*, Vol. 16, No. 1, 1993, pp. 151–159.

[63] Howell, K. and Keeter, T., "Station-Keeping Stategies for Libration Point Orbits: Target Point and Floquet Mode Approaches," *Proceedings of AAS/AIAA Space Flight Mechanics Meeting, 1995, Advances in the Astronautical Sciences*, Vol. 16, 1995, pp. 1377–1396.

[64] Howell, K. and Marchand, B., ""Natural and Non-Natural Spacecraft Formations Near L_1 and L_2 Libration Points in the Sun-Earth/Moon Ephemerics System"," *Dynamical Systems: An International Journal*, Vol. 20, No. 1, March 2005, pp. 149–173.

[65] Folta, D. and Vaughn, F., "A Survey of Earth-Moon Libration Orbits: Stationkeeping Strategies and Intra-Orbit Transfers," *In AAS/AIAA Astrodynamics Specialists Conference*, Providence, Rhode Island, August 16 - 19, 2004.

[66] Folta, D. and Quinn, D., "Lunar Frozen Orbits," *In AIAA/AAS Astrodynamics Specialist Conference*, Keystone, Colorado, August 21 - 24, 2006.

[67] Wie, B., "Space Vehicle Dynamics and Control," *AIAA Education Series*, 1998.

[68] McInnes, C., "Solar sail Trajectories at the Lunar L_2 Lagrange Point," *Journal of Spacecraft and Rocket*, Vol. 30, No. 6, 1993, pp. 782–784.

[69] Simo, J. and McInnes, C. R., "Solar Sail Trajectories at the Earth-Moon Lagrange Points," *In 59th International Astronautical Congress*, Glasgow, Scotland, 29 September - 03 October 2008. IAC-08.C1.3.13.

[70] Simo, J. and McInnes, C. R., "Stabilization of Displaced Periodic Orbits in the Solar Sail Restricted Three-Body Problem," *presented at the SIAM Conference on Applications of Dynamical Systems (DS09)*, Snowbird, Utah, May 17 - 21, 2009.

[71] Simo, J. and McInnes, C. R., "Asymptotic Analysis of Displaced Lunar Orbits," *Journal of Guidance, Control and Dynamics*, Vol. 32, No. 5, September-October 2009, pp. 1666–1671.

[72] Simo, J. and McInnes, C. R., "Analysis and Control of Displaced Periodic Orbits in the Earth-Moon System," *In* 60^{th} *International Astronautical Congress*, Daejeon, Republic of Korea, 12 - 16 October 2009. IAC-09.C1.2.4.

[73] Simo, J. and McInnes, C. R., "Displaced Periodic Orbits with Low-Thrust Propulsion in the Earth-Moon System," *In* 19^{th} *AAS/AIAA Space Flight Mechanics Meeting*, Savannah, Georgia, February 8 - 12, 2009. AAS 09-153.

[74] Simo, J. and McInnes, C. R., "Solar Sail Orbits at the Earth-Moon Libration points," *Communications in Nonlinear Science and Numerical Simulation*, Vol. 14, No. 12, December 2009, pp. 4191–4196.

[75] Simo, J. and McInnes, C. R., "Designing Displaced Lunar Orbits Using Low-Thrust Propulsion," *Journal of Guidance, Control and Dynamics*, Vol. 33, No. 1, January-February 2010.

[76] Simo, J. and McInnes, C. R., "On the Stability of Approximate Displaced Lunar Orbits," *In* 20^{th} *AAS/AIAA Space Flight Mechanics Meeting*, San Diego, California, February 14-17, 2010. AAS 10-181.

[77] Simo, J. and McInnes, C. R., "Displaced solar sail orbits: Dynamics and applications," *In* 20^{th} *AAS/AIAA Space Flight Mechanics Meeting*, San Diego, California, February 14-17, 2010. AAS 10-222.

[78] Simo, J. and McInnes, C. R., "Solar Sail Orbits at the Earth-Moon Libration points," *In Nonlinear Science & Complexity, Springer*, Vol. 2, 2009, pp. 147–155.

[79] Simo, J. and McInnes, C. R., "Solar Sail Orbits at the Earth-Moon Libration points," *In* 2^{nd} *Conference on Nonlinear Science and Complexity, NSC 08*, Porto, Portugal, July 28-31, 2008.

[80] Simo, J. and McInnes, C. R., "Displaced Lunar Orbits Using Low-Thrust Propulsion: Application to Binary Asteroid," *Workshop on Applications on Control theory to Astrodynamics problems*, Surrey, England, April 26-27, 2010.

[81] Simo, J. and McInnes, C. R., "Displaced Periodic Orbits with Low-Thrust Propulsion in the Earth-Moon System," *Advances in the Astronautical Sciences*, Vol. 134, 2009, pp. 815–828.

[82] Simo, J. and McInnes, C. R., "On the Stability of Approximate Displaced Lunar Orbits," *Advances in the Astronautical Sciences*, Vol. 136, 2010, pp. 1229–1238.

[83] Simo, J. and McInnes, C. R., "Displaced solar sail orbits: Dynamics and applications," *Advances in the Astronautical Sciences*, Vol. 136, 2010, pp. 1803–1816.

[84] Ozimek, M., Grebow, D., and Howell, K., "Design of Solar Sail Trajectories with Applications to Lunar South Pole Coverage," *Journal of Guidance, Control, and Dynamics*, Vol. 32, No. 6, November-December 2009, pp. 1884–1897.

[85] Ozimek, M., Grebow, D., and Howell, K., "A Collocation Approach for Computing Solar Sail Lunar Pole-Sitter Orbits," *In AIAA/AAS Astrodynamics Specialist Conference*, Pittsburgh, Pennsylvania, August 2009. Paper AAS 09-378.

[86] Grebow, D., Ozimek, M., and Howell, K., "Advanced Modeling of Optimal Low-Thrust Lunar Pole-Sitter Trajectories," *In* 60^{th} *International Astronautical Congress*, Daejeon, Republic of Korea, 12 - 16 October 2009. IAC-09-C1.5.4.

[87] Wawrzyniak, G. G. and Howell, K., "Accessing the Design Space for Solar Sails in the Earth-Moon System," *In AIAA/AAS Astrodynamics Specialist Conference*, Pittsburgh, Pennsylvania, August 2009. Paper AAS 09-348.

[88] Wawrzyniak, G. G. and Howell, K., "Numerical Methods to generate Solar Sail Trajectories," 2^{nd} *International Symposium on Solar Sailing (ISSS 2010)*, New York, USA, July 20 - 22, 2010.

[89] Wawrzyniak, G. G. and Howell, K. C., "The Solar Sail Lunar Relay Station: An Application of Solar Sails in the Earth-Moon System," *In* 59^{th} *International Astronautical Congress*, Glasgow, Scotland, September 29 - October 3, 2008. IAC 08.C1.3.14.

[90] Slotine, J.-J. E. and Li, W., *Applied Nonlinear Control*, Prentice Hall, Englewood Cliffs, New Jersey 07632, 1991.

[91] Macdonald, M. and McInnes, C. R., "Solar Sail Science Mission Applications and Advancement," *Advances in Space Research*, 2011, in press.

[92] Tsiolkovsky, K. E., "Extension of Man into Outer Space," *Proceedings of the Symposium on Jet Propulsion*, Vol. 2, United Scientific and Technical Presses, 1936.

[93] Tsander, K., "From a Scientific Heritage," *NASA TTF-541*, 1924.

[94] Wright, J. L., "Space Sailing," *Gordon and Breach Science Publications*, Amsterdam, 1992.

[95] Wright, J. L. and Warmke, J. M., "Solar Sail Mission Applications," *In AAS/AIAA Astrodynamics Specialist Conference*, San Diego, California, August 1976. AIAA 76-808.

[96] Diedrich, B. and Mulligan, P., "Solar Sails and Artificial Lagrange Orbits for Remote Sensing, Telecommunications, and Space Weather Applications," 87^{th} *American Meteorological Society Annual Meeting, Third Symposium on Future National Operational Environmental Satellites*, San Antonio, California, January 13 - 18, 2007.

[97] McInnes, C., Hughes, G., and Macdonald, M., "Payload Mass Fraction Optimization for Solar Sail Cargo Missions," *Journal Of Spacecraft and Rockets*, Vol. 39, No. 6, 2002, pp. 933–935.

[98] McInnes, C., "Artificial Lagrange Points for a Non-Perfect Solar Sail," *Journal of Guidance, Control and Dynamics*, Vol. 22, No. 1, 1999, pp. 185–187.

[99] West, J. L. and Derbes, B., "Solar Sail Vehicle System Design for the Geostorm Warning Mission," *In Proc.* 41^{st} *AIAA Structures, Structural Dynamics and Materials Conf. and Adaptive Structures Forum*, Atlanta, GA, September 2000. AIAA-2000-5326.

[100] Yen, C.-W. L., "Solar Sail Geostorm Warning Mission Design," *In* 14^{th} *AAS/AIAA Space Flight Mechanics Conference*, Maui, Hawaii, February 8 - 12, 2004. AAS 04-107.

[101] West, J. L., "The GeoStorm Warning Mission: Enhanced Opportunities based on New Technology," *In* 14^{th} *AAS/AIAA Space Flight Mechanics Meeting*, Maui, Hawaii, February 8 - 12, 2004. AAS 04-102.

[102] West, J. L., "The Lunar Polesitter," *In AIAA/AAS Astrodynamics Specialist Conference*, Honolulu, Hawaii, August 18 - 21, 2008.

[103] K. Hamera, T. Mosher, M. G. R. P. L. S. and Trojan, J., "An Evolvable Lunar Communication and Navigation Constellation Architecture," 26^{th} *International Communications Satellite Systems Conference*, San Diego, California, June 10 - 12, 2008. AIAA-2008-5480.

[104] Ely, T. A. and Lieb, E., "Constellations of Elliptical Inclined Lunar Orbits Providing Polar and Global Coverage," *Journal of the Astronautical Sciences*, Vol. 54, No. 1, 2006, pp. 53–67.

[105] Ely, T. A. and Lieb, E., "Stable Constellations of Frozen Elliptical Inclined Orbits," *Journal of Astronautical Sciences*, Vol. 53, No. 3, July-September 2005, pp. 301–316.

[106] Antonio, E. and Lara, M., "Frozen Orbits about the Moon," *Journal of Guidance, Control, and Dynamics*, Vol. 26, No. 2, March-April 2003, pp. 238–243.

[107] Russell, R. P. and Lara, M., "Repeat Ground Track Lunar Orbits in the Full-Potential Plus Third-Body Problem," *In AIAA/AAS Astrodynamics Specialist Conference and Exhibit*, Keystone, Colorado, 21 - 24 August 2006. AIAA 2006-6750.

[108] Forward, R. L., "Light-Levitated Geostationary Cylindrical Orbits using Perforated Light Sails," *Journal of the Astronautical Sciences*, Vol. 32, No. 2, April-June 1984, pp. 221–226.

[109] Forward, R. L., "Light-Levitated Geostationary Cylindrical Orbits," *Journal of the Astronautical Sciences*, Vol. 29, No. 1, January-March 1981, pp. 73–80.

[110] Fischer, H. J. and Haerting, A., "Why Light-Levitated Geostationary Cylindrical Orbits are not Feasible," *Journal of the Astronautical Sciences*, Vol. 40, No. 3, September 1992, pp. 329–333.

[111] van de Kolk, C., "Stability of Levitated Cylindrical Orbits by using Solar Sails," *In AAS/AIAA Astrodynamics Specialist Conference*, Gridwood, Alaska, August 16 - 19, 1999. AAS 99-335.

[112] Baig, S. and McInnes, C., "Light-Levitated Geostationary Cylindrical Orbits are Feasible," *Journal of Guidance, Control, and Dynamics*, Vol. 33, No. 3, May-June 2010, pp. 782–793.

[113] Morrow, E., Lubin, D., and Sheers, D., "Solar Sail Orbits Operations at Asteroids," *Journal of Spacecraft and Rockets*, Vol. 38, No. 2, March-April 2001, pp. 279–286.

[114] Scheeres, D. and Schweickart, R., "The Mechanics of Moving Asteroids," 1^{st} *Planetary Defense Conference*, Orange County, California, February 23 - 26, 2004. AIAA 2004-1446.

[115] Scheeres, D. J., "Close Proximity Operations for Implementing Mitigation Strategies," *Planetary Defense Conference*, Orange County, California, 23^{rd} Feb. 2004. AIAA 2004-1445.

[116] Conway, B. A., "Near-Optimal Defection of Earth-Approaching Asteroids," *Journal of Guidance, Control and Dynamics*, Vol. 24, No. 5, 2001, pp. 1035–1037.

[117] Dachwald, B. and Wie, B., "Solar Sail Trajectory Optimization for Intercepting, Impacting, and Deflecting Near-Earth Asteroids," *AIAA Guidance, Navigation, and Control Conference and Exhibit*, San Francisco, California, August 15 - 18, 2005. AIAA 2005-6176.

[118] Izzo, D., Bourdoux, A., Walker, R., and Ongaro, F., "Optimal Trajectories for the Impulsive Deflection of near Earth Objects," *Acta Astronautica*, Vol. 59, 2006, pp. 294–300.

[119] Vasile, M., "A Multi-mirror Solution for the Deflection of Dangerous NEOs," *Communications in Nonlinear Science and Numerical Simulation*, Vol. 14, No. 12, December 2009, pp. 4139–4152.

[120] Lu, E. T. and Love, S. G., "Gravitational Tractor for Towing Asteroids," *Nature*, Vol. 438, No. 7065, 2005, pp. 177–178.

[121] Broschart, S. B. and Scheeres, D. J., "Control of Hovering Spacecraft Near Small Bodies: Application to Asteroid 25143 Itokawa," *Journal of Guidance, Control, and Dynamics*, Vol. 28, No. 2, March-April 2005, pp. 343–354.

[122] McInnes, C. R., "Near Earth Object Orbit Modification using Gravitational Coupling," *Journal of Guidance, Control and Dynamics*, Vol. 30, No. 3, May-June 2007, pp. 870–872.

[123] Rios-Reyes, L. and Scheeres, D. J., "Generalized Model for Solar Sails," *Journal of Spacecraft and Rockets*, Vol. 42, No. 1, January-February 2005, pp. 182–185.

[124] Brophy, J. R. and Noca, M., "Electric Propulsion for Solar System Exploration," *Journal of Propulsion and Power*, Vol. 14, No. 5, September-October 1998, pp. 700–707.

[125] Flandro, G., "Asymptotic Solution for Solar Electric Low Thrust Orbit Raising with Eclipse Penalty," *In AIAA Mechanics and Control of Flight Conference*, Anaheim, California, August 5 - 9, 1974. AIAA-74-802.

[126] Kluever, C. and Pierson, B., "Optimal Low-Thrust Three-Dimensional Earth-Moon Trajectories," *Journal of Guidance, Control and Dynamics*, Vol. 18, No. 4, July-August 1995, pp. 830–837.

[127] Chase, R., "Potential Military Space Systems Applications for advanced Electric Propulsion Systems," 17^{th} *SAE and ASME, Joint Propulsion Conference*, Colorado Springs, Colorado, July 27 - 29, 1981. AIAA-1981-1536.

[128] Deininger, W., "A Review of Nuclear Electric Propulsion Spacecraft System Concepts," 21^{st} *DGLR and JSASS, International Electric Propulsion Conference*, Orlando, Florida, July 18 - 20, 1990. AIAA-1990-2553.

[129] J. Senent, C. O. and Capella, A., "Low-Thrust Variable Specific Impulse Transfers and Guidance to Unstable Periodic Orbits," *Journal of Guidance, Control, and Dynamics*, Vol. 28, March-April Monterey, California, February 9 - 11, 1998. AAS 98-168, pp. 280–290.

[130] Morimoto, M., Yamakawa, H., and Uesugi, K., "Periodic Orbits with Low-Thrust Propulsion in the Restricted Three-Body Problem," *Journal of Guidance, Control, and Dynamics*, Vol. 29, No. 5, September-October 2006, pp. 1131–1139.

[131] Morimoto, M. Y., Yamakawa, H., and Uesugi, K., "Artificial Equilibrium Points in the Low-Thrust Restricted Three-Body Problem," *Journal of Guidance, Control, and Dynamics*, Vol. 30, No. 5, September-October 2007, pp. 1563–1568.

[132] Cichan, T. and Melton, R. G., "Optimal Trajectories for Non-Ideal Solar Sails," *Advances in the Astronautical Sciences*, Vol. 109, No. 3, 2001, pp. 2381–2391.

[133] Colasurdo, G. and Casalino, L., "Optimal Control Law for Interplanetary Trajectories with Solar Sail," *Advances in the Astronautical Sciences*, Vol. 109, No. 3, 2001, pp. 2357–2368.

[134] Coverstone, V. L. and Prussing, J. E., "Technique for Escape from Geosynchronous Transfer Orbit Using a Solar Sail," *Journal of Guidance, Control and Dynamics*, Vol. 26, No. 4, July-August 2003, pp. 628–634.

[135] Kuninaka, H., Nishiyama, K., Funaki, I., Yamada, T., Shimizu, Y., and Kawaguchi, J., "Powered Flight of Electron Cyclotron Resonance Ion Engines on Hayabusa Explorer," *Journal of Propulsion and Power*, Vol. 23, No. 3, May-June 2007, pp. 544–551.

[136] "NASA Glenn Research Center Website," *http://www.nasa.gov/centers/glenn/about/fs08grc.html*.

[137] Cano, J. L., Hechler, M., Khan, M., and Pulido, J., "SMART-1 Consolidated Report on Mission Analysis," *Issue 1.2, S1-ESC-RP-5506*, July 16 2001.

[138] Leipold, M. and Götz, M., "Hybrid Photonic/Electric Propulsion," *Kayser-Threde, TR SOL4- TR-KTH-0001*, Munich, Jan. 2002, ESA Contract No. 15334/01/NL/PA.

[139] Mengali, G. and Quarta, A. A., "Trajectory Design with Hybrid Low-Thrust Propulsion system," *Journal of Guidance, Control, and Dynamics*, Vol. 30, No. 2, March-April 2007, pp. 419–426.

[140] Mengali, G. and Quarta, A. A., "Tradeoff Performance of Hybrid Low-Thrust Propulsion System," *Journal of Spacecraft and Rockets*, Vol. 44, No. 6, 2007, pp. 1263–1270.

[141] Dachwald, B., Seboldt, W., and Häusler, B., "Performance Requirements for Near-Term Interplanetary Solar Sailcraft Missions," 6^{th} *International Symposium on Propulsion for Space Transportation of the XXIst Century*, Versailles, France, May 2002.

[142] Baig, S. and McInnes, C., "Artificial Three-Body Equilibria for Hybrid Low-Thrust Propulsion," *Journal of Guidance, Control, and Dynamics*, Vol. 31, No. 6, November-December 2008, pp. 1644–1655.

[143] Poincaré, H., "Sur le problème des trois corps et les équations de la dynamique," *Acta Mathematica*, Vol. 13, 1890, pp. 1–27.

[144] Tisserand, F., "Traité de la Mécanique Céleste," *Gauthier-Villars et fils, Paris*, 1889.

[145] Mignard, F., "Stability of L_4 and L_5 against Radiation Pressure," *Celestial Mechanics*, Vol. 34, 1984, pp. 275–287.

[146] Battin, R. H., "An Introduction to the Mathematics and Methods of Astrodynamics," *AIAA Education Series. American Institute of Aeronautics and Astronautics, Reston, Revised Edition*, 1999.

[147] Koon, W., Lo, M., Marsden, J., and Ross, S., "Low Energy Transfer to the Moon," *Celestial Mechanics and Dynamical Astronomy*, Vol. 81, No. 1, 2001, pp. 63–73.

[148] Perko, L., "Differential Equations and Dynamical Systems," *Springer-Verlag*, New York, 1991.

[149] Guckenheimer, J. and Holmes, P., "Nonlinear Oscillations, Dynamical Systems, and Bifurcations of Vector Fields," *Springer-Verlag*, New York, 1983.

[150] Hénon, M., "Families of Periodic Orbits in the Three-Body Problem," *Celestial Mechanics*, Vol. 10, 1974, pp. 375–388.

[151] D. Dichmann, E. D. and Paffenroth, R., "The Computation of Periodic Solutions of the Three-Body Problem Using the Numerical Continuation Software AUTO," *Libration Point Orbits and Applications*, Hong Kong, China, World Scientific, 2003.

[152] Farquhar, R., "The Control and use of Libration-Point Satellites," *Ph.D. Dissertation, Stanford University*, 1968.

[153] Richardson, D. L., "Analytic Construction of Periodic Orbits about the Collinear Points," *Celestial Mechanics*, Vol. 22, No. 3, 1980, pp. 241–253.

[154] Sontag, E., "Mathematical Control Theory," *Springer*, New York, 1998.

[155] Jurdjevic, V. and Quinn, J., "Controllability and stability," *Journal of Differential Equations*, Vol. 28, 1978, pp. 381–389.

[156] Wie, B., "Thrust Vector Control Analysis and Design for Solar-Sail Spacecraft," *Journal of Spacecraft and Rockets*, Vol. 44, No. 3, May-June 2007, pp. 545–557.

[157] Cielaszyk, D. and Wie, B., "New Approach to Halo Orbit Determination and Control," *Journal of Guidance, Control and Dynamics*, Vol. 19, No. 2, March-April 2009, pp. 266–273.

[158] Schaub, H., Akella, M. R., and Junkins, J. L., "Adaptive Realization of Linear Closed Loop Tracking Dynamics in the Presence of Large System Model Errors," *Journal of the Astronautical Sciences*, Vol. 48, No. 4, October-December, 2000, pp. 537–551.

[159] Gurfil, P., "Nonlinear Feedback Control of Low-Thrust Orbital Transfer in a Central Gravitational Field," *Acta Astronautica*, Vol. 60, 2007, pp. 631–648.

[160] Yan, Q., Yang, G., Kapila, V., and de Queiroz, M., "Nonlinear Dynamics and Output Feedback Control of Multiple Spacecraft in Elliptic Orbits," *In Proceedings of the American Control Conference*, Vol. 2, Chicago, Illinois, June 2000.

[161] Kokotovic, P. and Khalil, H. K., *Singular Perturbations in Systems and Control*, IEEE Press, New York, 1986.

Appendix A

Constants

The following constants and characteristic values are used for computation throughout the analysis:

Table A.1: Physical Constant Parameter Values.

Quantity	*Value*	*Units*
$R^{\star}$	384400	km
GM_E	398600.4480734463	km^3/s^2
GM_M	4902.799140594719	km^3/s^2
R_E	6378.137	km
R_M	1738	km

Appendix B

Other Cases and Further Simulations

B.1 A hybrid concept for a constant displacement distance of $2500\ km$

The figure sequence for Chapter 6, Section 6.4 for a constant displacement distance of 2500 km, considering a characteristic acceleration of $a_0 = 0.14\ mm/s^2$ is shown in this Section.

The magnitude of the total control effort appears in Figure B.1 for the orbit around the L_1 and L_2 libration points, while the acceleration derived from the solar sail and the SEP thruster is given in Figure B.2 for L_1, and Figure B.3 for L_2.

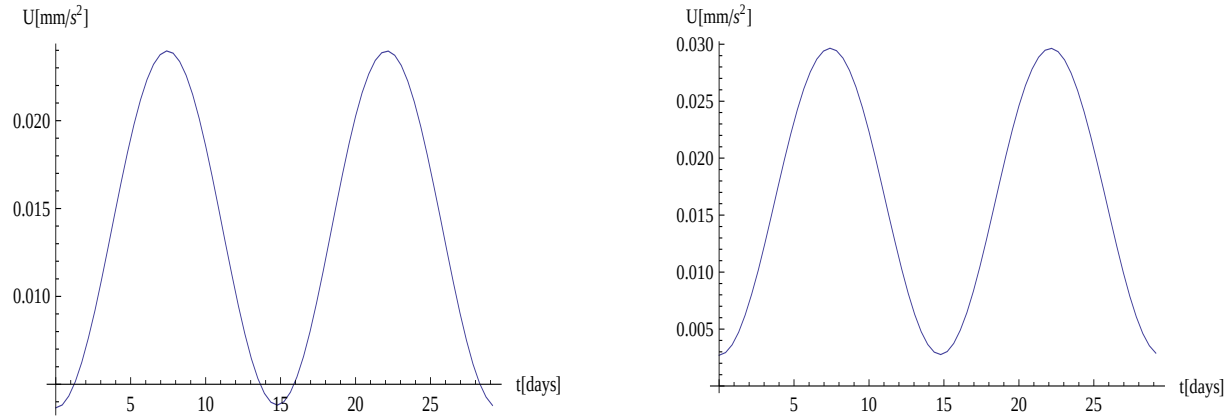

Figure B.1: (a) Magnitude of the total control effort about the L_1 point; (b) Magnitude of the total control effort about the L_2 point.

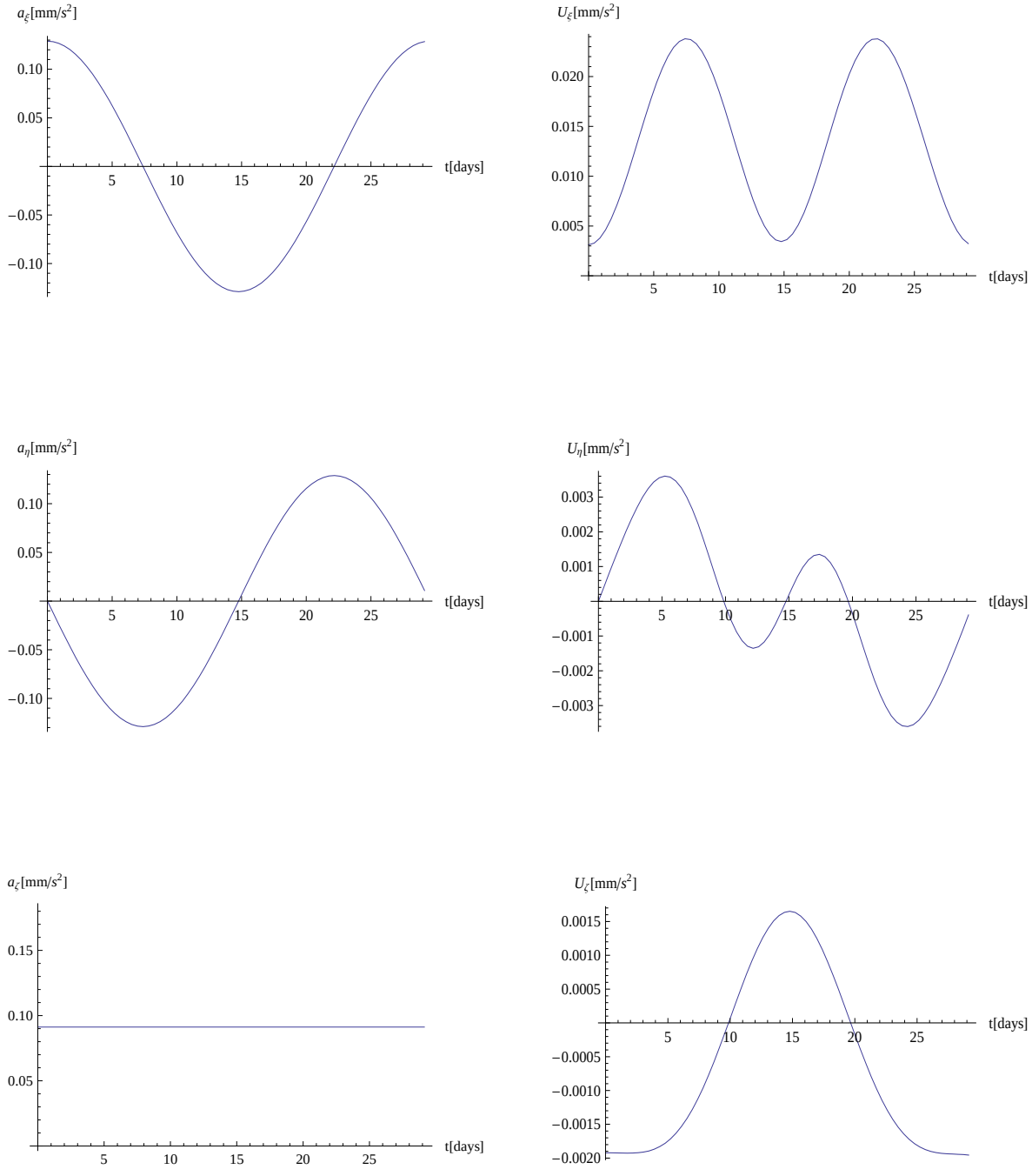

(a) (b)

Figure B.2: (a) Acceleration derived from the solar sail about the L_1 point; (b) Acceleration derived from the SEP thruster about the L_1 point.

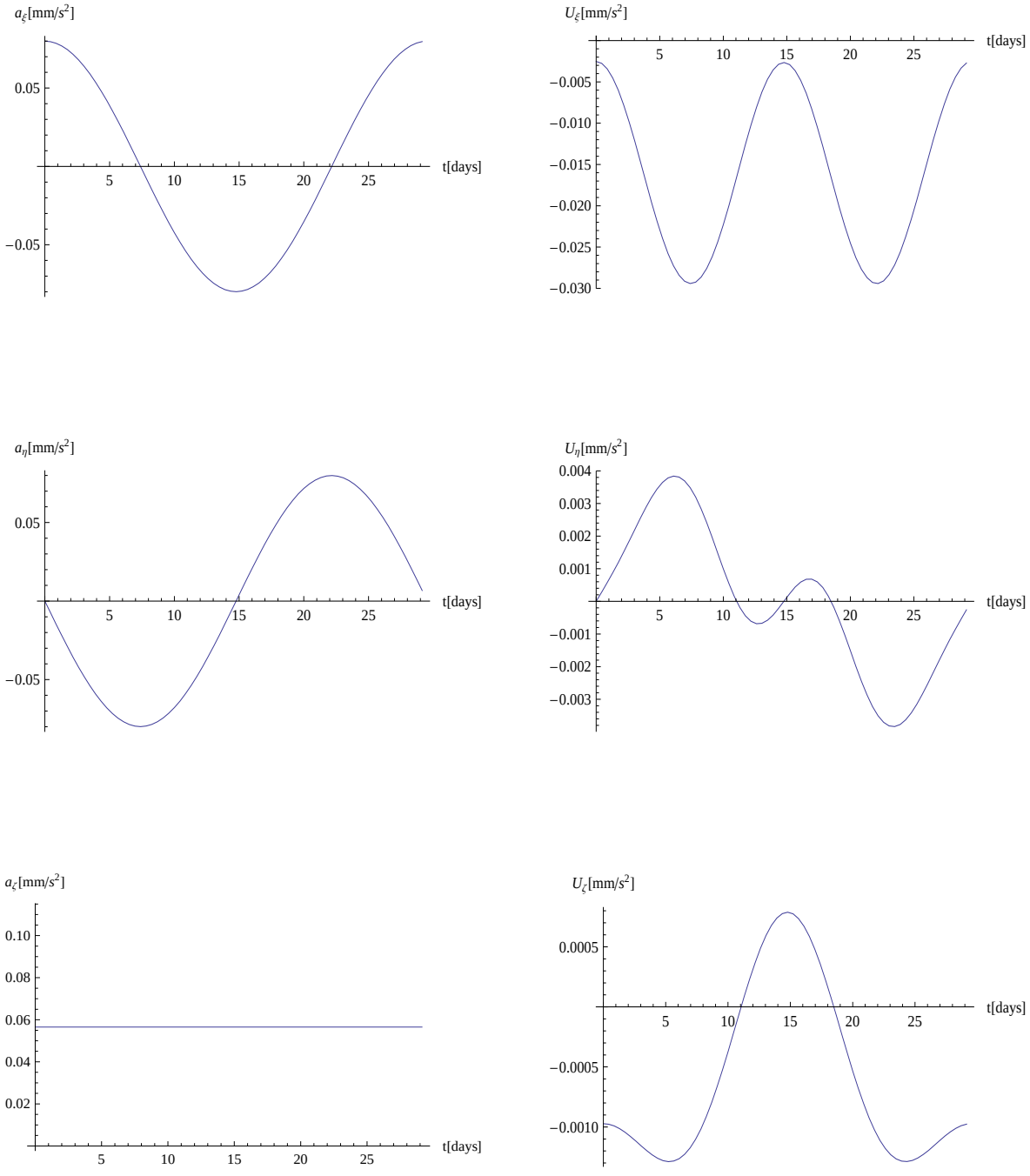

(a) (b)

Figure B.3: (a) Acceleration derived from the solar sail about the L_2 point; (b) Acceleration derived from the SEP thruster about the L_2 point.

B.2 Applications to Binary Asteroid Systems: The Cases $\mu = 0.15$ and $\mu = 0.35$

The figure sequence for Chapter 6, Section 6.5 with $\mu = 0.15$ and $\mu = 0.35$ is given in this Section.

Again, the magnitude of the total control effort appears in Figure B.4 for system mass ratio $\mu = 0.15$, and Figure B.6 for $\mu = 0.35$. The acceleration derived from the solar sail (denoted by a_ξ, a_η, a_ζ) is plotted in terms of components for one revolution of the asteroid orbit in Figure B.5 (a), and the SEP acceleration components appears in Figure B.5 (b) for system mass ratio $\mu = 0.15$. Similarly, the acceleration derived from the solar sail is plotted in terms of components for one revolution of the asteroid orbit in Figure B.7 (a), and the SEP acceleration components appears in Figure B.7 (b) for system mass ratio $\mu = 0.35$.

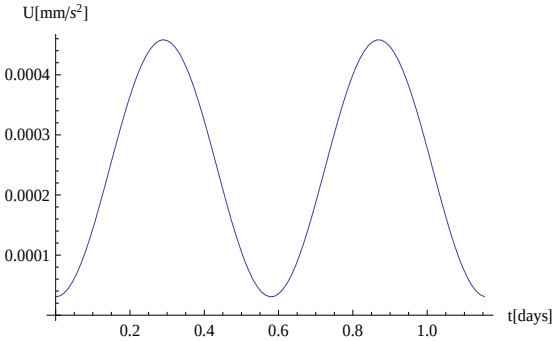

Figure B.4: Magnitude of the total control effort, $\mu = 0.15$.

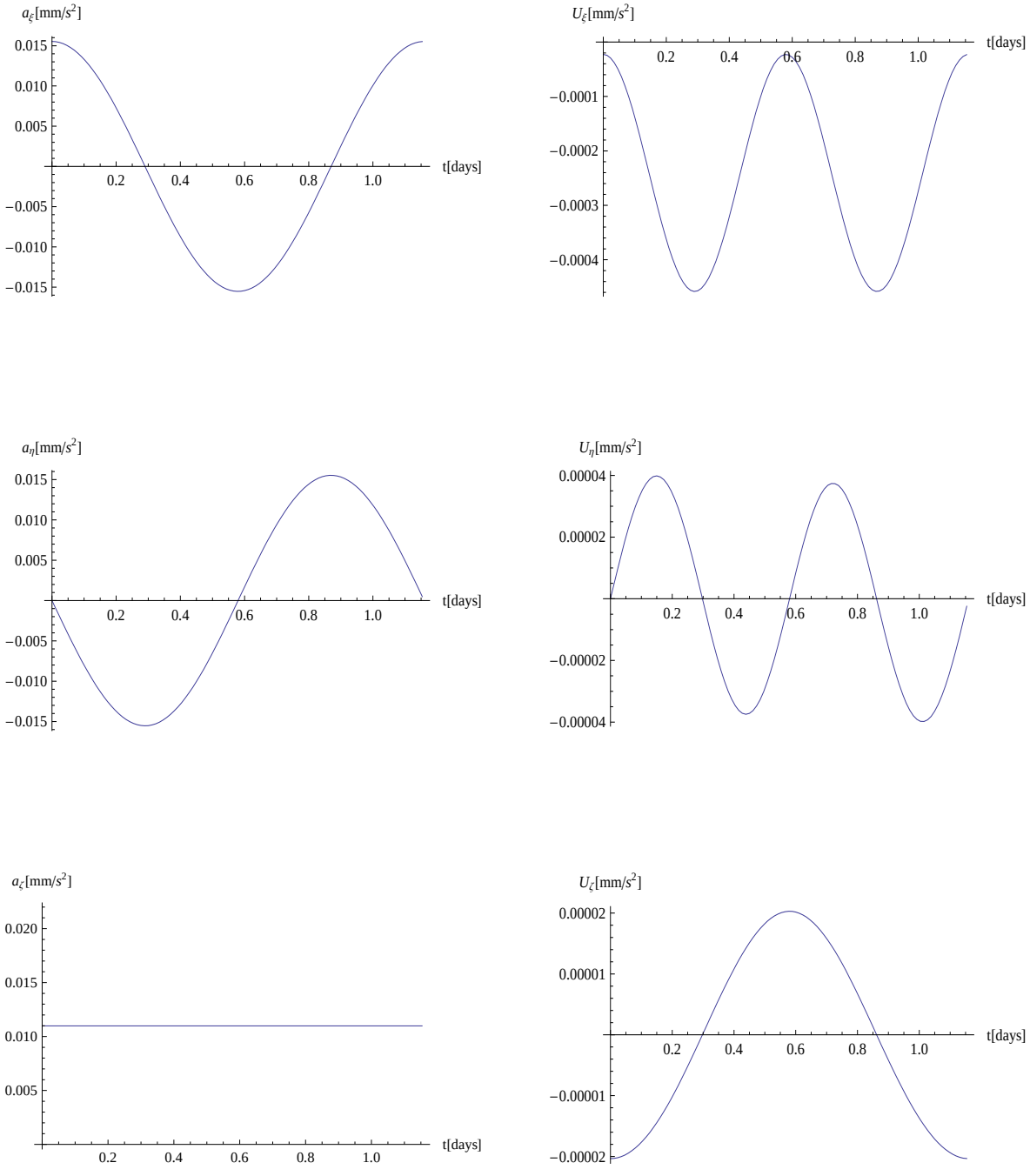

(a) (b)

Figure B.5: (a) Acceleration derived from the solar sail with the system mass ratio $\mu = 0.15$; (b) Acceleration derived from the SEP thruster with the system mass ratio $\mu = 0.15$.

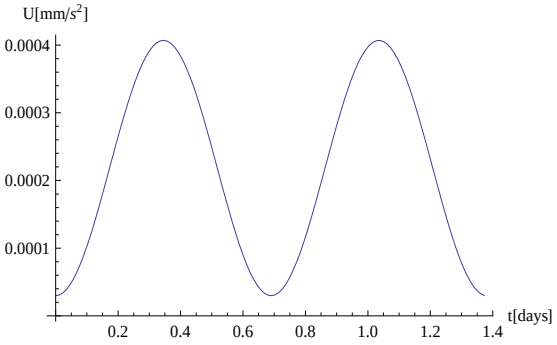

Figure B.6: Magnitude of the total control effort, $\mu = 0.35$.

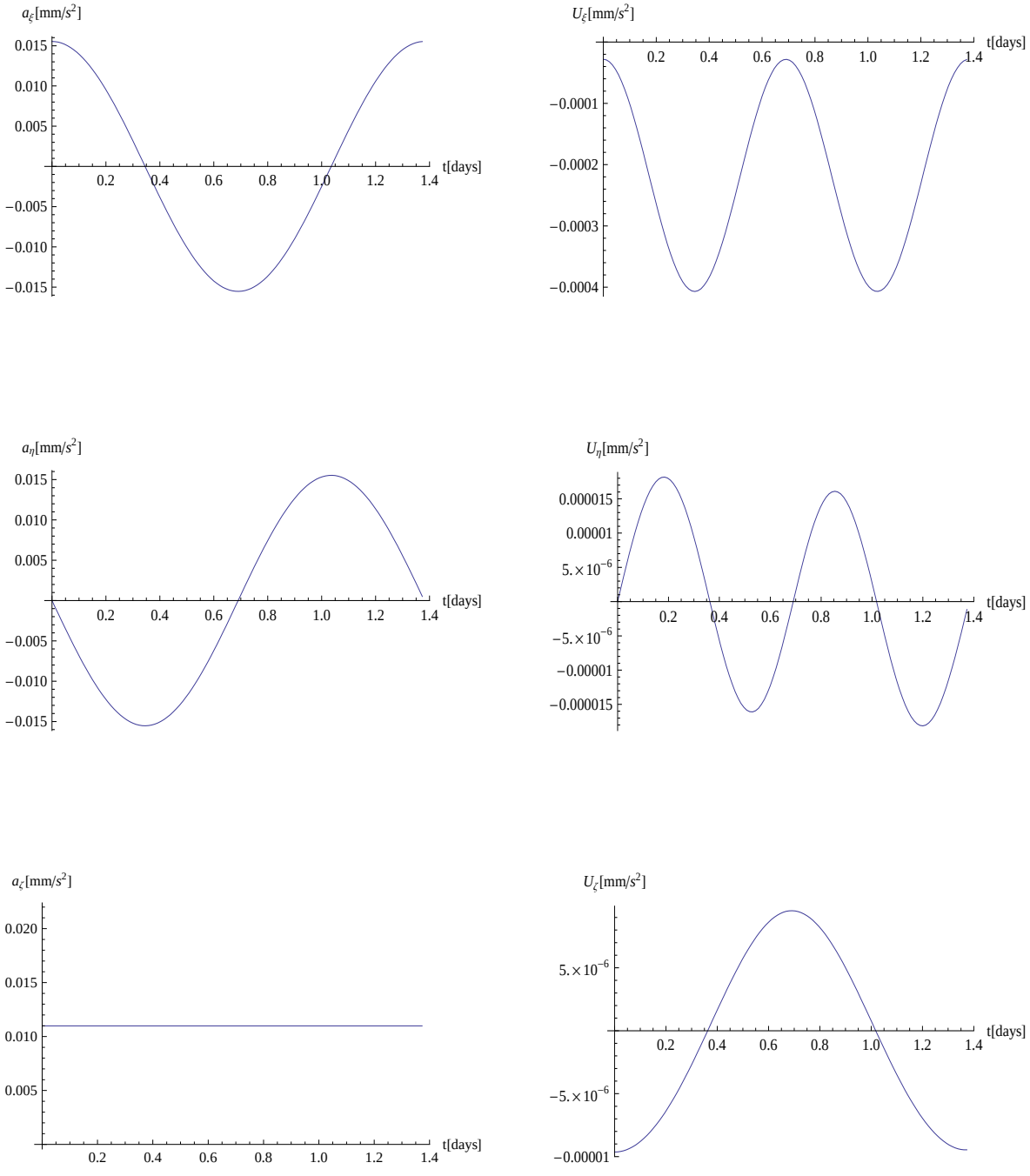

(a) (b)

Figure B.7: (a) Acceleration derived from the solar sail with the system mass ratio $\mu = 0.35$; (b) Acceleration derived from the SEP thruster with the system mass ratio $\mu = 0.35$.